An Optimized Surface Topography for Calcium Phosphate Bone Tissue Engineering Scaffolds

Jacob Sebastian Mealy, B.A., B.A.I., P.G. Dip.

A thesis submitted to the University of Dublin in partial fulfilment of the requirements for the degree of

Doctor in Philosophy

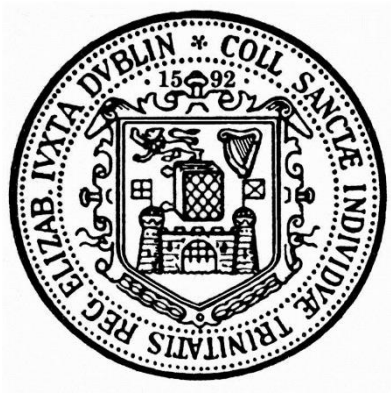

School of Engineering

Trinity College Dublin

Ireland

September, 2015

Supervisor

Prof. Kevin O'Kelly

Declaration

I declare that this thesis has not been submitted as an exercise for a degree at this or any other university and it is entirely my own work. Except for the experiments on inflammation in Chapter 5 which were performed by Clare Cunningham; specifically, Figures 5.8 and 5.9.

I agree to deposit this thesis in the University's open access institutional repository or allow the Library to do so on my behalf, subject to Irish Copyright Legislation and Trinity College Library conditions of use and acknowledgement.

Jacob Mealy

February, 2016

Table of Contents

List of Figures

List of Tables

Symbols & Abbreviations

Symbols

Signifier	Definition	Units
k	Permeability	m^2
r	Radius	m
R_a	Average surface roughness	m
R_q	Root-mean-square surface roughness	m
$S_{100\% \text{ reduced}}$	Fluorescence signal generated by 100% reduced resazurin solution	None
S_a	3D average surface roughness	m
$S_{control}$	Fluorescence signal generated by 10%vol. resazurin media solution	None
S_{dr}	Developed interfacial area ratio	None
S_q	3D root-mean-square surface roughness	m
S_x	Fluorescence signal of sample at day x	None
Δ	Average absolute slope	None
λ	Average surface wavelength	m
τ	Tortuosity	None
ϕ	Porosity	None

Abbreviations

Signifier	Definition
ALP	Alkaline phosphatase, a marker of osteogenic differentiation
FDA	Food and Drug Administration
HA	Hydroxyapatite
He-ion	Helium-ion microscopy
IL1-α, β	Interleukin-1 alpha, beta, inflammatory cytokines
IUPAC	International Union of Pure and Applied Chemistry
LPS	Lipopolysaccharide, an endotoxin that can cause strong immune reactions in animals
MSC	Mesenchymal stem cell
MTT	3-(4, 5-Dimethylthiazol-2-yl)-2, 5-diphenyltetrazolium bromide, a tetrazolium salt reduced to purple formazan in the mitochondria of living cells
SE	Standard error of the mean
SEM	Scanning electron microscopy
TCP	Tri-calcium phosphate
TNFα	Tumour Necrosis Factor, an inflammatory cytokine
µCT	Micro-computer tomography

Acknowledgements

I would first like to thank my supervisor Prof. Kevin O'Kelly. This project was made possible by the opportunities he gave me, along with his support, advice and our invaluable academic discussions. Likewise, to all those in the Trinity Centre for Bioengineering and in the wider Dept. of Mechanical and Manufacturing Engineering, thank you for the kindness you have shown and the help you have offered me over the last four years.

Specific academic acknowledgment must go to the following people. Dr Gráinne Cunniffe for her patient instruction on aseptic cell culture techniques, Dr Clive Downing and Dr Alan Bell for their training and technical help with SEM and He-ion microscopy respectively, Dr Robbie Goodhue for his expertise in XRD and for the enlightening conversations about the ensuing data, Dr Daithi De Faoite for further XRD and material analysis.

Clare Cunningham performed the experiments on inflammatory response to the various scaffolds presented in Chapter 5. My sincere thanks to both her and Prof. Aisling Dunne for these results and the fascinating education in immunology that they afforded me. I hope that this project precedes further collaboration between our two departments.

To my family; Ken, Cliona, Sam and Anna, you have all supported me in so many different ways, not just during my Ph.D., but my life as a whole. I truly appreciate everything you have done for me.

Finally, to Alice. Your support of me over the last four years and more has been overwhelming. For all of the meticulous advice, necessary cajolement, undeserved sympathy, excessive patience and boundless good humour, thank you.

This work was funded by the Higher Education Authority of Ireland under the Programme for Research in Third Level Institutions (PRTLI5) and the Graduate Research Education Programme in Engineering (GREPEng).

Publications and Presentations Arising from This Study

J. Mealy and K. O'Kelly, "Cell response to hydroxyapatite surface topography modulated by sintering temperature," *J. Biomed. Mater. Res. Part A*, 2015. (Journal Article)

J. Mealy and K. O'Kelly, "A novel calcium phosphate/alumina scaffold with optimized surface topography for oro-maxillo-facial bone tissue engineering," *Bioengineering in Ireland – Proceedings of the Twenty-First Annual Conference of the Section of Bioengineering of the Royal Academy of Medecine in Ireland,* 2015. (Oral Presentation)

J. Mealy and K. O'Kelly, "Ceramic scaffolds for bone healing", *Discover Research Dublin – EU Researchers' Open Night,* 2014. (Poster Presentation)

J. Mealy and K. O'Kelly, "Cell response to nanoscale surface topography of hydroxyapatite tissue engineering scaffolds," *Bioengineering in Ireland – Proceedings of the Twentieth Annual Conference of the Section of Bioengineering of the Royal Academy of Medecine in Ireland,* 2014. (Oral Presentation)

J. Mealy and K. O'Kelly, "Cell response to nanoscale surface topography of hydroxyapatite tissue engineering scaffolds," *European Society of Biomaterials – Proceedings of the Twenty-Fifth European Conference on Biomaterials,* Madrid, Spain, 2013. (Poster Presentation)

J. Mealy and K. O'Kelly, "From biomaterial to bone – the response of cells to scaffold surfaces," *Discover Research Dublin – EU Researchers' Open Night,* 2013. (Poster Presentation)

J. Mealy and K. O'Kelly, "Cell response to surface topology in hydroxyapatite tissue engineering scaffolds," *Bioengineering in Ireland – Proceedings of the Nineteenth Annual Conference of the Section of Bioengineering of the Royal Academy of Medecine in Ireland,* 2013. (Oral Presentation)

Abstract

Improved scaffold/host integration and avoiding core necrosis are important and active goals in tissue engineering. Alternatives to bone tissue grafting that are highly bioactive and inexpensive to manufacture are clinical necessities, particularly in relation to today's ageing population profiles. There is also a need to develop such grafting alternatives for applications where tissue-engineered solutions (i.e. based on tissue growth in perfusion bioreactors) are not feasible from a clinical and cost perspective. Nanoscale surface topography has the potential to influence many aspects of cellular behaviour on tissue engineering scaffolds including proliferation. The aim of this project was to optimize the surface topography of a hydroxyapatite (HA) bone tissue engineering scaffold in order to increase mesenchymal stem cell (MSC) proliferation on the construct. The working hypothesis was that nanoscale features incorporated into the scaffold pore surfaces would provide a stimulus to increase cellular activity and overall proliferation.

Two methods of surface manipulation were investigated; sintering temperature and nanophase addition. Cellular proliferation was indicated by MSC metabolic activity and was measured using a resazurin sodium salt media assay. Scaffold pore surfaces were modelled using lightly pressed, two-dimensional disks in order to remove confounding factors such as pore size and shape.

Altering sintering temperature from 1100°C to 1350°C produced several surface morphologies: from small, granular features ~500nm in size at low temperatures, to smooth, glassy features ~10µm in size at high temperatures. Cells proved incapable of adhering to the low temperature surfaces (<1250°C) while the best proliferation rates were observed on the 1300°C and 1350°C samples. The average surface wavelength, λ, correlated strongly with cellular

response to the surfaces. From this, a threshold wavelength of ≥2.4μm was suggested as being necessary for cellular adhesion. The best performing surfaces had wavelengths of ~2.65μm.

The necessity for a relatively long surface wavelength to facilitate adhesion led to the design of an idealised surface with an underlying basal layer of appropriate wavelength, into which would be embedded nanoscale features to stimulate proliferation. This design was realised through the addition of an alumina nanopowder to the HA precursor in concentrations of 1-10wt%. The resulting topography closely matched the target design and proved capable of increasing cellular proliferation by 261.5% over pure HA.

These results translated well to full, three-dimensional scaffolds, proving the applicability of the technique in a relevant, tissue engineering context. The novel construct, consisting of HA+5wt% alumina, was compared to a market leading commercial scaffold as a benchmark test. Cellular proliferation was an order of magnitude higher on the novel formulation when compared with the commercial scaffold. Furthermore, ELISA tests revealed that IL-1β expression in both macrophages and dendritic cells in response to the scaffolds was six times less on the novel formulation as on the commercial comparator. This shows that the novel scaffold induced a significantly lower inflammatory response compared to an existing therapy. These results prove the superior *in vitro* performance of the novel topography and allow for the optimized scaffold to be taken forward to *in vivo* trials.

The overall project aim was achieved by adding an alumina nanophase to HA bone tissue engineering scaffolds to produce an optimized surface topography that significantly increased cellular proliferation on the scaffold pores. This will improve the overall scaffold performance *in vivo* and help alleviate the effects of core necrosis. The novel construct has the advantage of using inexpensive materials and a manufacturing methodology that is easily scalable to industry.

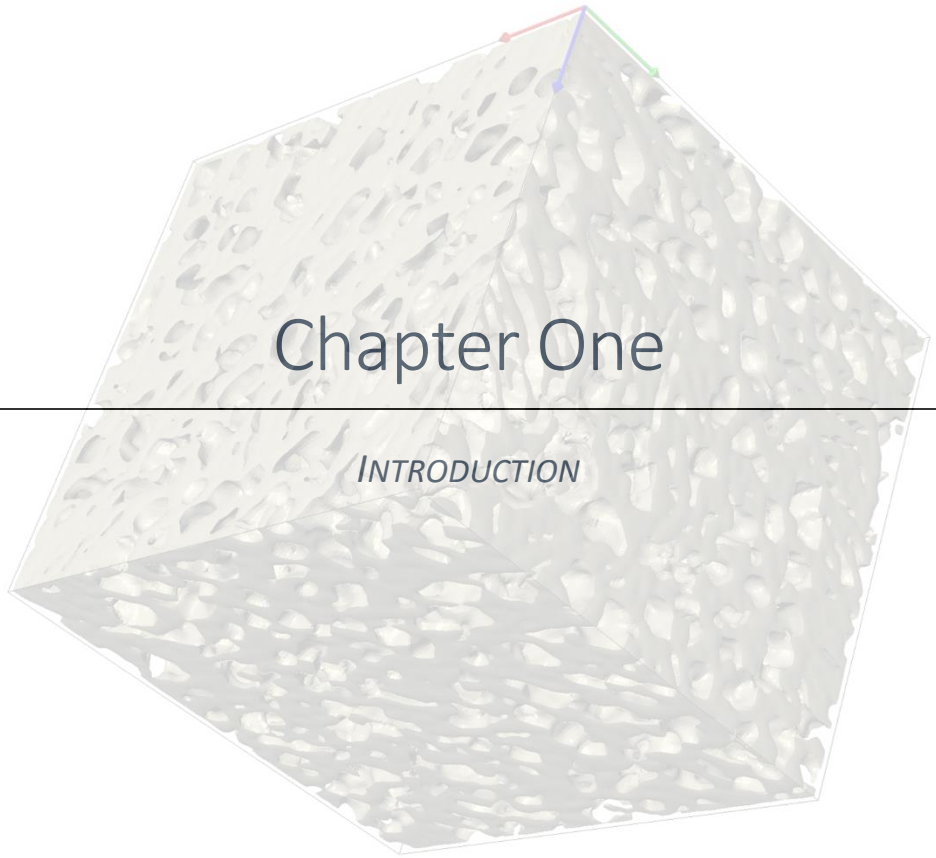

Chapter One

INTRODUCTION

1.1 Problem Outline

It is estimated that about half of the three million musculoskeletal procedures performed annually in the United States involve auto or allografts [1]. This figure stretches to about 2.2 million worldwide which potentially results in an approximate market size of about $3.5 billion. A recent and comprehensive review by Velasco *et al* [2] makes the point that estimating the potential market size for a bone tissue engineering therapy depends on how such a therapy is defined. Most definitions of bone graft substitutes include not only scaffolds and implants but also cell-based therapies and growth factors. The Velasco review estimates that a global market of $3.3 billion is forecast by 2017. It is clear that there is a large and growing commercial interest in developing alternatives to bone tissue grafting.

Establishing commercial viability is necessary to fund a tissue grafting alternative. However, it is also important to remember that there is a real clinical need for alternatives to bone grafting, from both a patient and practitioner point of view. Although tissue grafts of all three origins; autogenous, allogeneic and xenogeneic, are widely accepted as the current gold standard for skeletal repair, they are subject to significant limitations. These include the expense and associated patient pain of additional harvesting procedures for autografts, the risk of transgenic disease associated with allo- and xenografts and the increased potential for infection across the board. Thus, there is a clear clinical need for a synthetic bone graft substitute that is safe, easy to use and cost effective.

The clinical need logically translates into the substantial market potential mentioned above. The market is important to bear in mind when evaluating potential solutions to the problem. The manufacturing process needs to be scalable to industry and as cheap as possible. A bone grafting alternative that sufficiently meets these requirements could be applicable not just to developed economies but also to Third World populations. Such a product would represent a significant step forward in terms of a global response to musculoskeletal trauma and disease.

Nowhere is the clinical relevance of a bone grafting alternative better represented than in the twin disciplines of dental and oro-maxillo-facial surgery. Here, bone grafting is both ubiquitous and technically challenging. The nature of the affected area requires grafts for small repairs such as tooth socket preservation as well as larger, more complex procedures such as facial reconstruction. As such, a solution that is favourable in this challenging clinical setting will likely be transferable to other skeletal sites.

A representative problem in oro-maxillo-facial surgery, and the impetus behind this investigation, is the reconstruction of the alveolar ridge. This is the bony process in the mandible into which the teeth are housed. Reconstruction of the alveolar ridge is often necessary after trauma or bone resorption to facilitate the implantation of teeth (Figure 1.1).

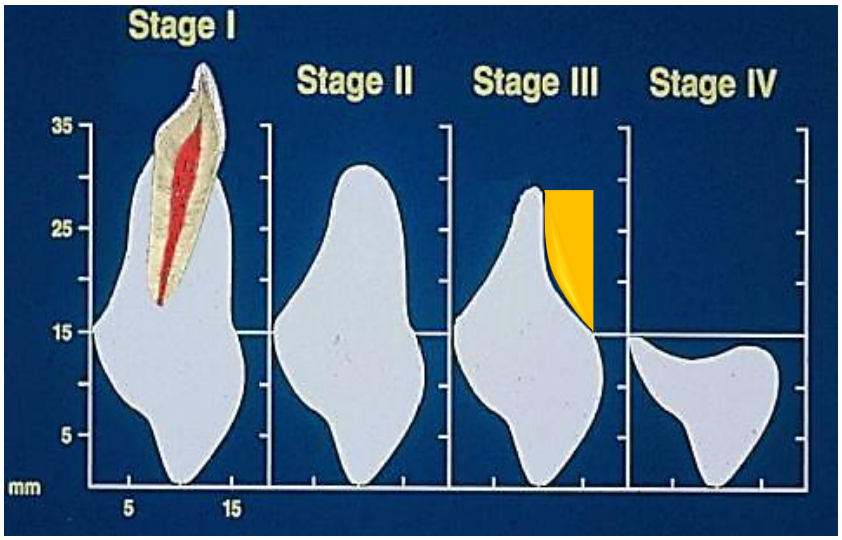

Figure 1.1. *Resorption of the alveolar ridge with a potential graft location shown in yellow. Original image courtesy of Spiller* [126].

This procedure is challenging due to the fact that the graft may only come into contact with the native bone on two sides. This results in a lack of structural support and is physiologically limiting as there are only two contact surfaces to enable cell migration and overall tissue-graft integration. Currently, the most expedient repair procedure in this situation is to rebuild the structure with a paste made of demineralized bovine bone in granular form. The paste is supported by a polymer membrane to hold it in place. The technique itself is difficult and rarely

results in full bone recovery. The membrane can slip resulting in failure of the graft and is another potential source of infection. An obvious and desirable alternative would be a self-supporting structure. This could then be optimised to allow cell migration and diffusion of nutrients through the limited contact areas in addition to promoting vascularisation.

The foundation for this work was the research performed by the Trinity Centre for Bioengineering (TCBE) into scaffolds for bone tissue engineering [3], [4]. The outcome of that research was a highly porous, multi-domain hydroxyapatite (HA) matrix that addresses many of the problems that such structures face. Chief amongst these is core necrosis; the widespread death of cells seeded into the centre of the scaffold due to poor nutrient transport to the site and waste removal from it. The TCBE structure combated this by incorporating three distinct porosity scales; these were defined by Buckley *et al.* as micropores (Ø1-2µm), mesopores (Ø100-200µm) and macrochannels (Ø300µm)[1]. The micropores and macrochannels facilitated diffusion through the matrix while the mesopores provided the environment for cell attachment and growth.

Despite these advances, the structure was still some way from being a commercially viable product. Cell necrosis, although much reduced, was still present at the structure core. Little *in vitro* cell analysis was carried out and no *in vivo* animal trials were performed. The next step was to actively encourage cell adhesion and proliferation throughout the scaffold. A matrix that rapidly integrates with the host tissue and vascularises is the key to improving the current crop of grafting procedures.

Traditionally, cells have been aided and encouraged to proliferate by seeding them onto scaffolds and culturing them in a bioreactor system prior to implantation. Bioreactors are varied but they frequently involve exposing the cells to a dynamic, perfusion environment. Whilst this

[1] It will be noted that these pore size definitions differ quite significantly from the International Union of Pure and Applied Chemistry (IUPAC) definitions of micropores (Ø<2nm) and mesopores (Ø2-50nm). This work continued with the Buckley definitions.

increases cellular proliferation, it is at odds with the predominantly diffusion based environment the cells subsequently experience *in vivo*. Furthermore, the added expense of preculture both from a financial and temporal point of view may make such cell-structure systems commercially unviable. Certainly this is the case in a clinical environment such as the Dublin Dental Hospital, where the most common grafting procedures are outpatient oriented and relatively quick (total procedure time is usually less than three hours). As such, a versatile product that could conceivably be used "wet" for preculture if desired; or "dry" for direct implantation into the host without preculture, would be ideal. Such a scaffold would fulfil the various commercial niches, including both small-scale procedures such as socket preservation and also larger, more complex ones such as alveolar ridge augmentation.

1.2 Scaffold Optimization

In this work, the approach is to ensure that any alterations to the scaffold will remain compatible with the original manufacturing parameters described by Buckley and O'Kelly [4]. This freeze-drying and sintering technique is a cheap and expedient method of manufacture and it is eminently scalable for industry. As a result, these parameters place some loose bounds around the research and provide a point of focus.

Additionally, it must be remembered that any alterations to the scaffold recipe may have knock-on effects not originally envisaged or intended. Many of the scaffold's properties are intrinsically linked, for example; porosity and mechanical strength: an increase in overall porosity will likely result in a reduction in mechanical strength. Situations like this require cost-benefit decisions that are best taken in consultation with clinicians, who, as the users of the end-product, will have an informed idea of how they would like it to perform. This work was carried out in consultation with practitioners from the Dublin Dental Hospital.

A key focus of this research is altering the surface topography of the scaffold to produce an improved cellular response. The surface topography can be altered at both the micro- and the nanoscale to provide a direct stimulation to the cells. Encouraging cell movement and, in particular, cellular proliferation through topographical manipulation will go a long way towards a more viable scaffold for oro-maxillo-facial applications.

1.3 Scaffold Characterization

There are numerous ways to improve the viability of a tissue engineering scaffold. Ultimately however, most come down to encouraging and prolonging cell life inside the scaffold matrix until vascularisation can take over. *In vivo* cellular proliferation is crucial to the integration of the scaffold into the host tissue. Aside from actual *in vivo* implantation, *in vitro* assessments of cellular performance provide the best metric for determining the potential capability of a scaffold. As *in vivo* work is generally prohibitively expensive (and often ethically challenging) for the initial, iterative stages of scaffold development, *in vitro* cell analysis is the current standard for tissue engineering evaluation.

1.4 Project Aim

This project aim was to produce a commercially viable ceramic alternative to bone grafting, predominantly for use in oro-maxillo-facial environments. Starting with an existing hydroxyapatite (HA) scaffold design template, the manufacturing procedure was modified to incorporate optimizations to the surface topography of the scaffold pores. Once formulated, the new topographies were evaluated to assess their effect on cell adhesion and proliferation and, thus, their role in influencing overall scaffold bioactivity.

1.5 Project Outline

In the early stages of the research, work continued on two aspects of scaffold development in parallel; experimental work on manufacturing surface topographies and computational modelling of 3D scaffolds. In the latter case, the aim was to develop a computational model of diffusion through the scaffold matrix. Ideally, this would provide a cheap tool to analyse the effects of parametric changes to the scaffold structure and thus inform design. Ultimately, this avenue of enquiry was outweighed by the laboratory analysis and was halted. Although unfinished, the model may prove useful in the future as a starting point for continued research. As such, it is included in Appendix III for reference.

The primary objective of the project was then to optimize the surface topography of the TCBE HA scaffold to increase cell proliferation on the pore surfaces. The topography was examined and evaluated through laboratory and *in vitro* analysis. A review of the literature, detailed in Chapter 2, identified sintering temperature and phase addition as likely manufacturing parameters for altering surface topography. Chapter 3 presents the topographies generated by varying sintering temperature. It also identifies an appropriate surface descriptor for the topographies and, using that, suggests the optimal sintering temperature to carry forward in the research. Chapter 4 discusses the effects of phase addition on the surface topography. Surface chemistry and bulk stability are also examined and an optimized scaffold formula produced. This formula is applied in full in Chapter 5, where it is also benchmarked against a market leading commercial scaffold. These benchmark tests cover both cellular proliferation and inflammatory response. The project as a whole is discussed and final conclusions drawn in Chapter 6.

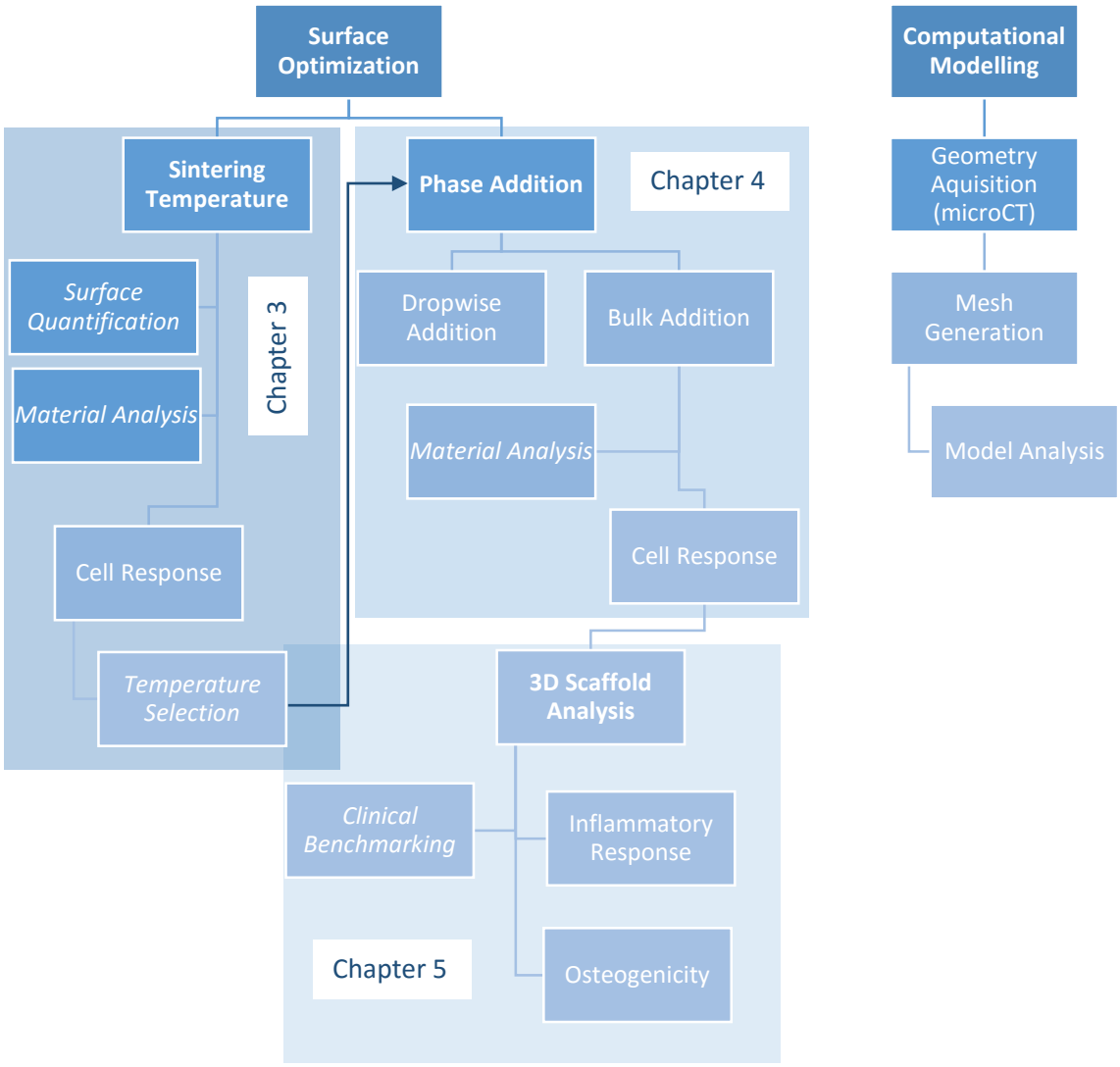

Figure 1.2. *Flowchart showing the overall project methodology.*

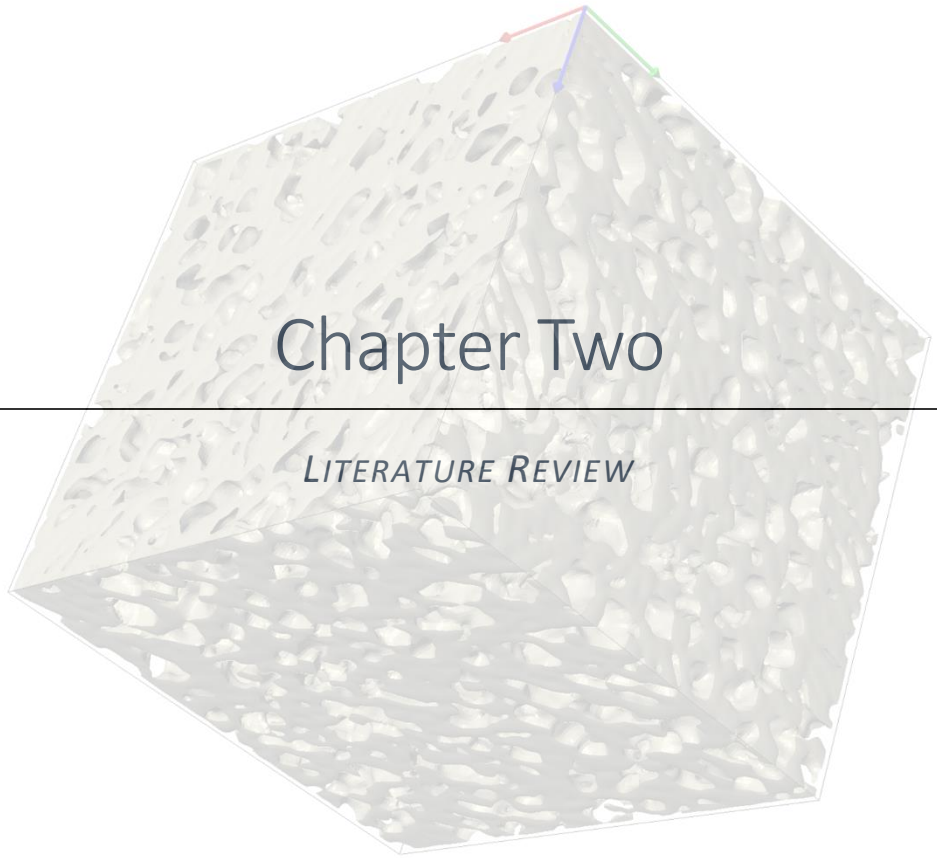

Chapter Two

Literature Review

2.1 Overview of the Implant Location

2.1.1 Introduction

The ideal outcome of any research into alternatives to bone grafting is a solution that is applicable across the skeleton. However, specific anatomical sites have different mechanical properties, for example bone is much less dense in the lumbar spine than it is in the femoral neck [5]. Such differences will present various challenges to an implanted construct. This work focusses on the alveolar ridge as an implant site. The unique trials of tooth implantation and mastication provided by the alveolar ridge along with its limited potential for blood supply to an implanted scaffold ensure the most rigorous examination possible. A brief overview of bone as a material and a description of the implant site are given to put this in context and explain the challenges further. Previous research into bone grafting alternatives is then examined.

2.1.2 Bone Anatomy and Physiology

The alveolar ridge is a specialised part of the maxilla and mandible bones that anchors and supports the teeth. Broadly speaking there are two types of bone commonly found in the human skeleton. The first and most commonly modelled is trabecular or cancellous bone. This is the spongy porous bone found in the middle of long bones and accounts for most of their volume. The cancellous bone is normally surrounded by cortical bone which is stronger and denser, and acts to protect the weaker bone within [6]. The alveolar ridge roughly follows this template consisting of mainly cancellous bone surrounded by a thin layer of cortical bone.

The major components of bone are carbonated hydroxyapatite crystals (plate-shaped, approximately 50 × 25nm), type I collagen fibrils (approximately 80-100nm diameter) and water [7]. The apatite serves to reinforce the fibrils which then combine to form bundles. Therefore,

bone can be described as a composite material deriving structural benefits from both its mineral and polymer components (Figure 2.1).

The exact arrangement of bone microstructure depends on the type of bone and can change over time. For example, trabecular bone density tends to decrease with age while cortical bone thickness is also reduced [5]. Bone also displays an adaptable microstructure in response to injury. Woven bone, or bone that forms in response to a break or other trauma, is generally disorganised with fibrils randomly orientated. This structure is then remodelled into cancellous or cortical bone with a more organised, isotropic arrangement of fibrils.

2.1.3 Bone Remodelling

The ability of bone to remodel to repair and prevent damage is fundamental to its viability as a tissue. Over time, fatigue cracks develop in the mineral structure due to the regular loading and unloading of the skeleton. These would eventually reach a size capable of causing failure if they were not removed in some way. Tight units of osteoclasts (bone resorbing cells) and osteoblasts (bone forming cells) move through the bone; resorbing and replacing bone matrix respectively [7]. In doing so, they remove any cracks in the tissue. This process gives rise to the longitudinal features known as osteons and the interstitial spaces between the osteoclasts and osteoblasts called Howship's lacunae (Figure 2.1) [7].

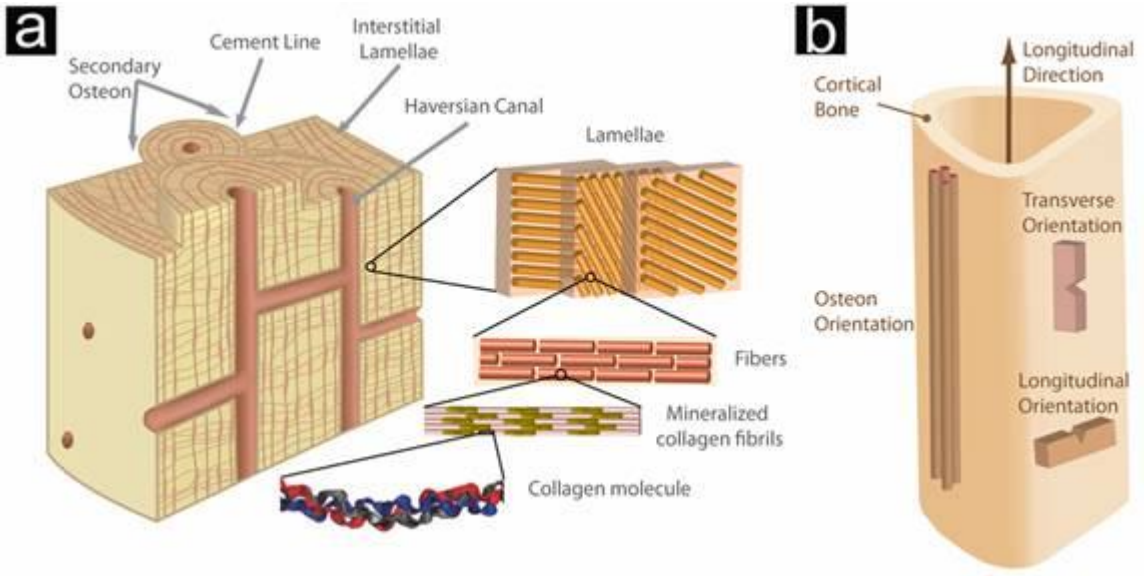

Figure 2.1. *Diagram showing (a) the microstructural and (b) the macrostructural organisation of bone [8].*

The remodelling process will thus impact on anything that is implanted into the bone tissue. In ideal cases it is advantageous, as a bioresorbable scaffold will eventually be replaced by naturally occurring tissue. This is far preferable to the scaffold remaining *in situ* indefinitely. In any event, the remodelling process must be taken into account as bone that is shielded from stress by an implant will eventually be resorbed and not replaced [9]. Nowhere is this more evident than in the resorption of the alveolar ridge after tooth loss.

2.1.4 The Alveolar Ridge: Unique Challenges and Clinical Needs

The alveolar ridge poses many unique challenges as a bone tissue engineering implant site. The ridge itself is the bony process into which the teeth are housed and consists of a dense outer layer of cortical bone surrounding more porous cancellous bone [10]. It plays an important role not only in support of the teeth but also in mastication and speech.

The remodelling process is particularly pertinent to the alveolar ridge as this structure undergoes continuous and extensive remodelling in response to tooth growth and the mechanical

loads associated with mastication [11]. This manifests itself primarily as severe resorption following tooth loss or removal (Figure 2.2, Figure 1.1 repeated here for clarity).

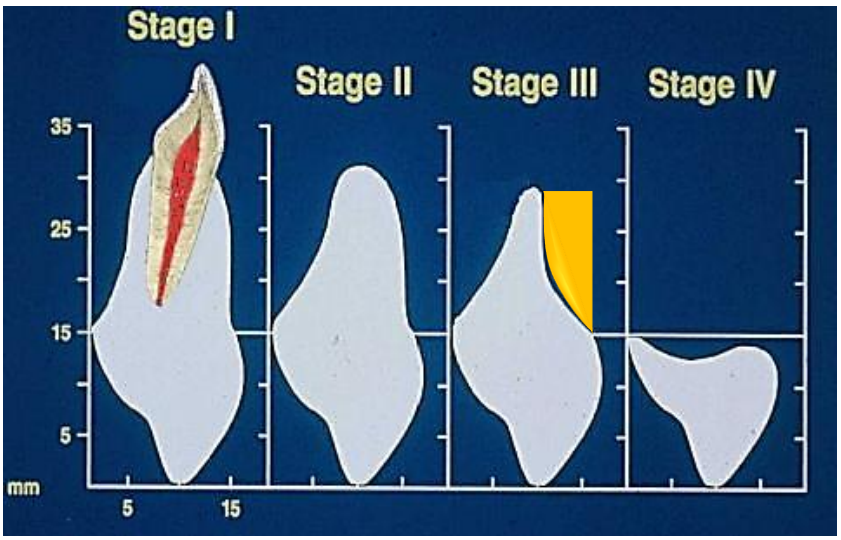

Figure 2.2. *Resorption of the alveolar ridge with a potential graft location shown in yellow. Original image courtesy of Spiller* [126].

The most basic procedure associated with the alveolar ridge is socket preservation. This can only be performed when three or more walls of the socket remain and involves filling the interstitial space with a granular bone graft [12]. The graft is sometimes held in place with a collagen plug and a flap of periosteum.

If the bone is so resorbed or damaged as to preclude socket preservation, a more complex reconstruction is required. This is made particularly challenging by the fact that any graft will have only one or maybe two contact surfaces with the host bone (Figure 2.2). This presents structural as well as nutritional constraints. A common approach is to build back up the required volume with a granulated graft as before. This is then held in place with a membrane, usually made of xenogeneic collagen [13]. This procedure is difficult however, and is subject to significant post-operative resorption [13]. A bioactive self-supporting block graft would be preferable, as long as cell viability is maintained through to the core.

2.2 Tissue Engineering Strategies and Their Limitations

2.2.1 Tissue Grafting

The current gold-standard in large bone tissue defect repair is autologous grafting [1]. It is difficult to characterise the success rate of autologous grafts in general as different authors tend to provide different standards of "success". However for dental implants, it is reasonable to accept that the success rate lies between approximately 73-97% [14]. For these figures success was defined as dental implants into autologous grafts which are still in place and suffering minimal resorption after a year. In terms of bone addition in severely resorbed alveolar ridges; about 12mm is a typical figure [15]. This gain is usually subject to some subsequent bone resorption over time.

However, these successes come at a price. There is an associated cost to the patient in terms of harvesting the required bone; the usual source of which is the iliac crest of the pelvis. This requires an additional procedure and is associated with elevated risk and pain for the patient. There is also an increased chance of infection and donor site morbidity associated with autografts. Allogeneic and xenogeneic grafts do not incur the same cost to the patient but they come with the added danger of immunogenic response [1]. For these reasons, a cost-effective, synthetic alternative is desirable.

2.2.2 Scaffolds

A tissue engineering scaffold is an artificial structure that will support and, ideally, encourage cell adhesion and proliferation[2]. The numerous cell types (macrophages, stem cells, osteoblasts, etc.) required for full bone healing can be seeded onto the scaffold prior to

[2] For the purposes of brevity, the use of decellularized extra-cellular matrix as a scaffold is here classified as a graft.

implantation or recruited from the surrounding host tissue. The design and analysis of tissue engineering scaffolds has formed the bulk of the research into grafting alternatives and that is the focus of this work.

A bone tissue engineering scaffold should have the following attributes [16];

1) Provide temporary mechanical support to the affected area.
2) Act as a substrate for osteoid deposition.
3) Contain a porous architecture to allow for vascularization and bone in-growth.
4) Encourage bone cell migration into the scaffold.
5) Support and promote osteogenic differentiation in the non-osseous, synthetic scaffold (osteoinduction).
6) Enhance cellular activity towards scaffold-host tissue integration (osseointegration).
7) Degrade in a controlled manner to facilitate load transfer to developing bone.
8) Produce non-toxic degradation products.
9) Not incite an active chronic inflammatory response.
10) Be capable of sterilization without loss of bioactivity.
11) Deliver bioactive molecules or drugs in a controlled manner to accelerate healing and prevent pathology[3].

As a result of its unique physiology, the alveolar ridge presents some additional specific clinical needs for a tissue engineering graft. Such a graft would ideally be easy to use, available off the shelf, self-supporting, roughly adaptable to specific defects and capable of nutrient transport through limited bone surface contact.

[3] This last is not a prerequisite but would be advantageous.

Properties such as porosity, permeability, mechanical strength and surface topography are all integral parts of scaffold design and contribute towards fulfilling the above requirements. Although they are often intrinsically linked and it can be difficult to alter one without affecting others, it is the manipulation of these properties that ultimately determines the viability of the end-product.

2.2.3 Core Necrosis and Limited Bone Ingrowth

Core necrosis occurs when the cells in the centre of a scaffold construct start to die. They rely on mass transport through the matrix for their oxygen and nutrients and, if this mass transport is insufficient, a toxic and hypoxic environment is created [17]. This phenomenon is exacerbated by the growth of cells on the exterior of the construct, occluding the pores and further decreasing the mass transport and cell penetration to the construct centre. The lack of penetration of seeded cells is well-illustrated by the Trinity Centre for Bioengineering (TCBE) scaffold (Figure 2.3).

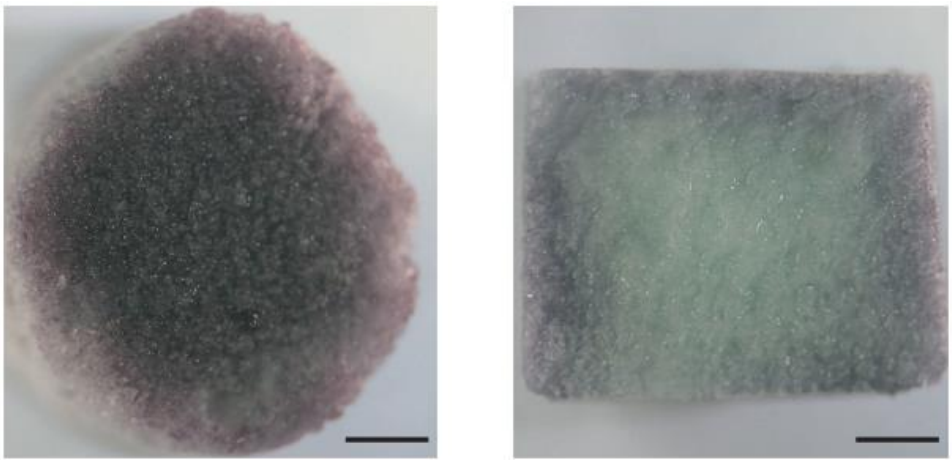

Figure 2.3. *MTT (tetrazolium dye) staining of surface and longitudinal cross-sections of hydroxyapatite scaffold four hours post-seeding with MC3T3-E1 mouse clonal osteogenic cells. The blue stain indicates cell viability, note its lack of penetration through to the scaffold core [4]. Scale bar is 1mm.*

Core necrosis is a specific term given to the more general problem of limited bone ingrowth into bone tissue engineering scaffolds. This issue provides the impetus for numerous studies and it will need to be solved before further progress is made towards a viable bone tissue engineering scaffold. There are numerous ways to do this including altering the pore size, morphology and interconnectivity of a scaffold [18], [19]. A more porous and interconnected scaffold will provide better mass transport to its core [19] but altering this attribute may have structural consequences. The interplay between a scaffold's characteristics is why it is so important that care is taken when using a manufacturing technique to effect a change on the scaffold structure.

Another important factor that negatively affects a scaffold's mass transport capabilities is pore occlusion. Specifically this occurs when cells proliferate to such a degree that they block the outer pores of a structure thus inhibiting the conductance of fluid and nutrients [17], [19]. Although this is a natural result of a scaffold's "success", it actually contributes to the construct's ultimate failure. As such, a functionally graded surface that controls general proliferation rates or cell motility through to the core may be more optimal.

Cell motility itself is an interesting topic here. Motility refers to an individual cell's movement. It is distinct from proliferation in that the cell itself moves as opposed to replicating; although it is possible for both events to occur simultaneously. Cell motility is traditionally associated with chemotactic gradients but there is little doubt that it also occurs in response to surface topography [20]. What needs to be determined is its relevance to a commercially viable bone tissue engineering scaffold. For example it may not be advantageous to encourage cells to migrate straight to the centre of a scaffold as they risk isolation. However, as discussed, if cells remain at the distal edges of the scaffold they occlude the pores and hinder fluid transport through the matrix.

It is possible to direct the migration of cells using nanoscale fibres [21] or grooves [22] so it should be possible to encourage cell movement from one location to another in a construct if so desired. This could mitigate any potential cell isolation while clearing cells from the edges of a scaffold before they can occlude the pores.

2.2.4 Perfusion-Based Tissue Culture

One proposed method for overcoming the mass-transport difficulties associated with three dimensional tissue cultures is to force or perfuse fluid through the matrix to ensure nutrient delivery and waste product removal from the entirety of the structure. A common approach is to culture cell-scaffold constructs in bioreactors that generate a perfusion environment prior to implantation [23]–[25].

There can be little doubt that perfusion culture of scaffold-cell constructs improves viability and bone ingrowth [23]–[25]. Increased fluid flow through the scaffold matrix results in elevated nutrient and waste product transport and less hypoxic conditions. Although these are clearly beneficial outcomes, they do not reflect the *in vivo* reality of the situation. In the body, once oxygen and nutrients have passed through the capillaries, they rely on diffusion to ultimately reach cells [26]. In fact, no cell in the body is further than between 100-200µm from a capillary [27]. Thus, it is illogical to develop a scaffold that will rely on an artificial culture environment to remain viable. Any further work must focus on producing a product that can perform sufficiently in a diffusive fluid regime.

The addition of a perfusion-based culture routine also has some obvious clinical drawbacks. The increased time and associated costs with the culture may outweigh the benefits of the scaffold pre-culture. Far better to design a scaffold to be used directly “off-the-shelf”; that can also be pre-cultured if the clinician desires.

2.3 Improving Scaffold Viability – Surface Topography

Cells respond in a multitude of ways to their topographical surroundings at both the micro- and the nanoscale. These responses include changes in proliferation, differentiation, motility, morphology and adhesion [28]–[31]. Although much work has been done to characterise the effects of surface topography on cells, no serious attempt has yet been made to incorporate this feature into tissue engineering scaffold design. Despite this, control of the surface morphology of a scaffold shows great promise as a stimulus for guiding cells in a tissue engineering context.

In discussing the effect of surface topography on cell behaviour in isolation, care must be taken to identify and, where possible, distinguish confounding factors. Alteration of the surface morphology can often have a profound effect on other aspects of the scaffold which may be equally influential to cell viability. A good example of this is variation in the surface chemistry of the scaffold either as a method for changing the topography [32] or as a side-effect [33]. Results from studies such as these are difficult to interpret from a purely topographical point of view.

It is possible to generate topographical changes through a variety of manufacturing techniques. Here, these have been split into three areas; machining, sintering temperature and phase addition.

2.3.1 Machined Surfaces

Machined surfaces refer to any topography that has been produced by a mechanical action performed post manufacture. Examples include etching, polishing, particulate coating and blasting.

In 2007, Dalby *et al.* [29] showed that the use of “nanoscale symmetry and disorder” could be used to induce mesenchymal stem cells to produce bone mineral. In addition, they

showed that the cells cultured on the topographically modified surface displayed a more osteoblastic differentiation profile than those cultured on flat surfaces. They investigated arrays of nanopits 120nm in diameter and 100nm deep arranged in various configurations (Figure 2.4). Sputter-coating and electroplating processes were used to produce dies which then generated the topographies. Their results give a good indication of the possibilities that exist for this technique, particularly in situations where stem cells are required to differentiate down a particular lineage quickly. However, the manufacturing process appears complex and expensive and also difficult to implement in a tissue engineering scaffold.

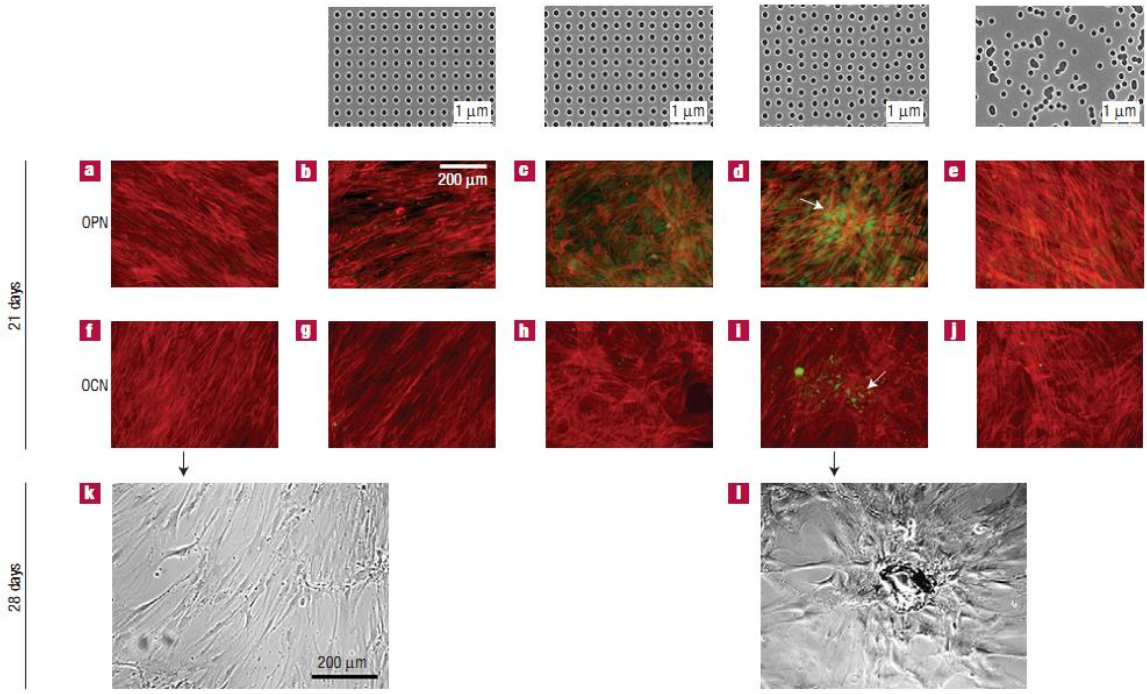

Figure 2.4. *OPN and OCN staining of MSC cells after 21 days and phase-contrast/bright-field images of alizarin-red-stained cells after 28 days. The top row shows the various surface topographies investigated [29].*

More recently, this work has been supported by gene expression studies by the same group which further elucidated the cell-surface interaction [34]. Nanotopographically textured surfaces induced highly osteogenic responses in human MSCs indicating that this method has potential for bone tissue engineering with this particular cell-type. The authors also hypothesize

that the basis for the osteogenic response is direct mechano-transduction through the cytoskeleton i.e. that the cells “feel” their surroundings via displacements in their cytoskeleton. Again, as a proof-of-concept this is promising but not readily applicable to a full 3D scaffold.

Lamers *et al.* [22] detail a study involving osteoblasts cultured on various nanoscale surfaces incorporating isotropic and anisotropic features (Figure 2.5). The surfaces consisted of ridges and grooves in size ratios of 1:3 and 3:1 in addition to a square topography. These surfaces were produced using a silicon template patterned using electron beam lithography. Significant cell responses were observed on pitches (i.e. the sum of ridge and groove width) ranging in size from 100-600nm. On the anisotropic surfaces, they found that cell morphology was affected much more than on isotropic surfaces with the cells significantly elongated and aligned with the main axis of the topography. Unlike morphology, cell motility was found to increase on both isotropic and anisotropic surfaces with maximum motility achieved on surfaces with a pitch of 400nm. As before, the manufacturing process used here is expensive. Moreover, it is difficult to see how it could be applied to the pore surfaces of 3D scaffolds.

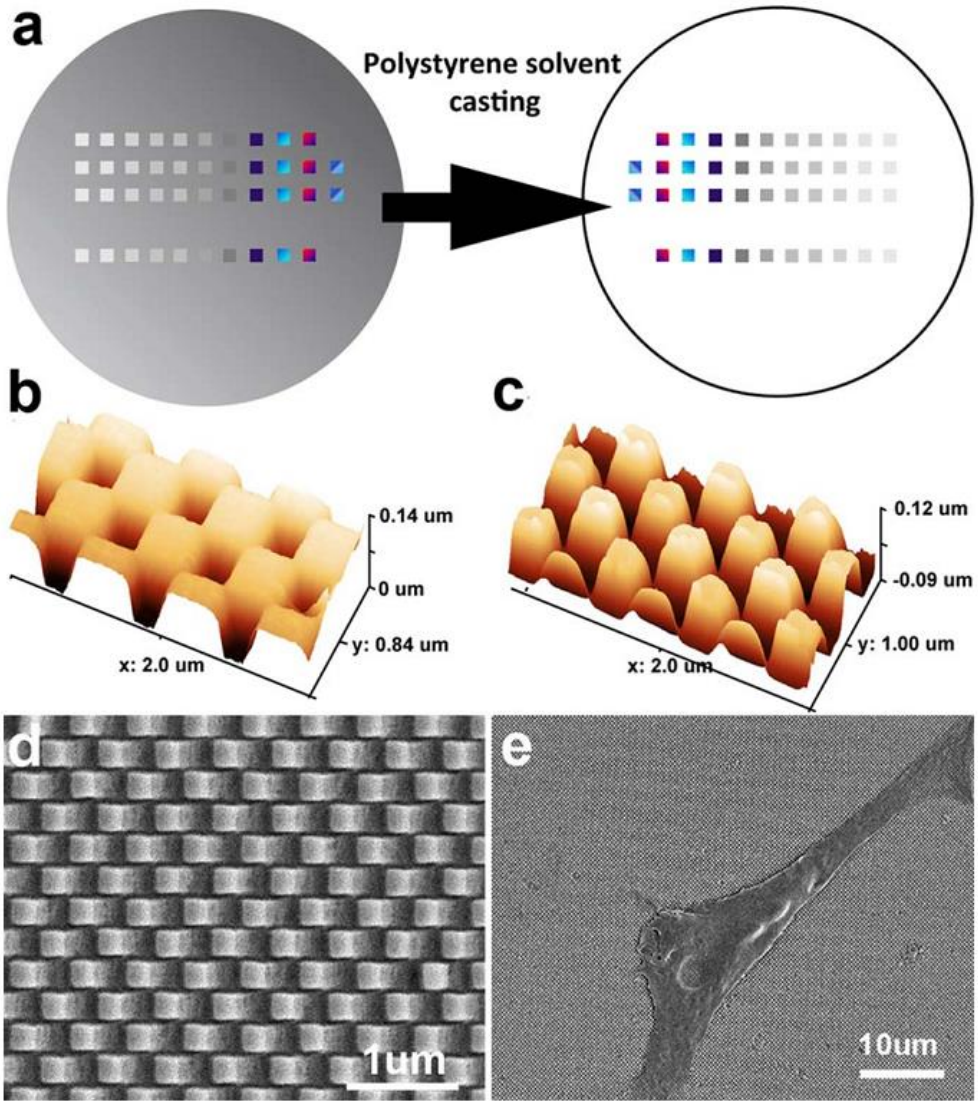

Figure 2.5. *(a) Silicon mould creation using polystyrene solvent casting. Polystyrene replicas visualised with (b)(c) AFM and (d) SEM. (e) Polystyrene replicas were finally used for biological analyses [20].*

Interestingly, a threshold depth of approximately 34nm was found for grooves to elicit a cellular response. The authors hypothesize that this is due to a build-up of proteins that masks the topography. This has implications for a lower boundary when considering novel nanoscale topography to induce a cell response.

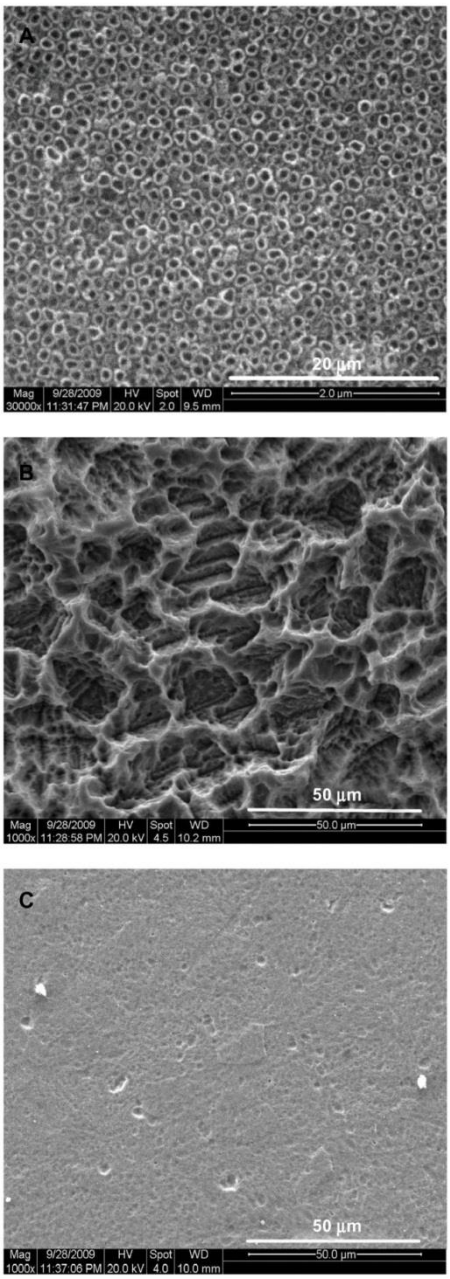

Figure 2.6. *SEM images of nanotube, microporous and smooth titanium surfaces from Xia et al. [33].*

Xia *et al.* [35] describe an investigation comparing three titanium surfaces; one smooth, one with nanoscale topographical features and one with microscale topographical features (Figure 2.6). The nanoscale surface consisted of nanotube arrays of diameter approximately 100nm achieved by anodisation in an aqueous solution of hydrofluoric acid. The microscale surface was a porous structure with various pores ranging in diameter from 1-60µm with the majority in the 10-20µm bracket. This was produced by immersion in an aqueous solution of HCL and $CaCl_2$. The smooth control was generated by polishing, which left some shallow pits and grooves. Of the three surfaces, the nanotube arrays induced the best responses in human osteosarcoma-derived MG63 cells with increased cell proliferation, alkaline phosphatase activity and expression of osteogenic proteins. These results were further verified in an *in vivo* study in rabbit tibiae. In addition, increased bone-implant interfacial strength was observed on the nanostructured samples. The study clearly demonstrates the importance of length-scale when considering cell-surface interactions and has positive implications not just for cell activity but also for construct-tissue integration.

In a recent study, topography effects were even found to have more of an effect than specific, chemical bioactivation of the surface [36]. Altmann *et al.* investigated the response of primary human alveolar bone osteoblasts (PHABOs) to three UV-treated titanium and zirconia

implant surfaces from commercial sources. While the UV treatment performed as intended, i.e. reduced surface carbon and increased hydrophilicity, the authors found that it was the differences in surface topography that had a greater effect on cell response. They concluded that the two rougher surfaces improved initial cell adhesion, while the smooth surface appeared to aid cell proliferation. In addition, gene expression was highest on the smoothest material. Surface roughness was quantified by roughness height (S_a) with the three values being; 1.09±0.1µm for TiUnite (titanium), 0.77±0.2µm for ZircaPore (zirconia) and 0.58±0.0µm for Zit-Z (zirconia).

Altmann *et al.* also refer to another study which they claim agrees with them; Vandrovcova *et al.* [37]. This was an investigation into the response of human osteoblast-like MG63 cells to titanium oxide coated glass with surface roughness values R_a = 0, 40, 100 and 170nm. As in the Altmann study, cell proliferation was greatest on the smoothest surface. Conversely however, improved initial cell adhesion was also observed on the smoother surfaces. Despite the similarity, the studies cannot be said to be in total agreement as implied by Altmann *et al.* This kind of discrepancy is discussed in more detail in Section 2.3.4.

The main conclusion from these studies in the context of the work presented here is that while they provide a good indication of the potential of nanoscale surface topography to effect changes in cell response, the machining manufacturing methods do not lend themselves to application in a tissue engineering scaffold. The porous 3D nature of the scaffold precludes any direct impingement on the pore surfaces making it difficult to generate a novel topography via a mechanical method.

2.3.2 Sintering Temperature

If it is accepted that machining is not a viable way to alter the surface topography of porous tissue engineering scaffolds then an alternative method of topographical manipulation

must be proposed. An integral part of ceramic processing is the sintering stage where the prepared construct or "green body" is subjected to a high temperature to fuse its constituent particles together. Depending on the temperature applied, various degrees of particle fusion are possible. Thus, it seems like a logical way of generating various surface topographies. At lower temperatures for example, more of the original particle shapes would be preserved, perhaps providing suitable topographical features to elicit a cell response. Conversely, at high temperatures where lots of particle fusion occurs, smoother surfaces would be generated. This method would clearly be very cheap and easy to implement as it is already a fundamental part of the manufacturing process.

Despite these arguments, a Pubmed search using the terms "sintering temperature surface topography" returned only five results[4]. Of these, none details a parametric study of different sintering temperatures, temperature effects on surface morphology and/or the subsequent cell response.

A search using the terms "sintering temperature cell response" was slightly more productive[3]. The fact that the crystal structure of HA is controllable via sintering temperature is established [38]. Although no biological work is shown, it is concluded that the HA is more stable at higher temperatures (1000-1200°C as opposed to 600-800°C). Rouahi *et al.* describe an interesting study utilising various HA powders from different sources, two of which were sintered to 1200°C to form bioceramics to study cell attachment [39]. The authors concluded that protein adsorption (analysed using powdered samples) is inversely related to the specific surface area (SSA) of the HA. The cell attachment (human Saos-2 osteoblastic cells) is then inversely related to the protein adsorption. The study is convoluted and fails to make any attempt to analyse different sintering temperatures. However, it gives a hint of the potential for altering the manufacturing

[4] Search performed on 13/2/2015.

process of HA to effect changes in cell response. It is also worth noting that the high temperature (1200°C) heat treatment of the powders acted to reduce the SSA of the samples.

Dulgar-Tulloch *et al.* [40] offer a more comprehensive study of effects of sintering temperature on cell response. They describe three different materials; alumina, titania and HA; sintered under a variety of regimes and temperatures to yield grain sizes of 24-50nm, 200nm and 1500nm (Figure 2.7). They found that human MSC adhesion and proliferation is reduced on surfaces consisting of grain sizes less than 200nm. It is also interesting to note that they found no correlation with surface roughness. Grain-size (a lateral as opposed to vertical dimension) was the surface descriptor they chose to differentiate their topographies. Again this point will be dealt with in more detail in Section 2.3.4. They also refer to similar work by Webster *et al.* [41], which they claim supports their conclusions. However this study was performed using rat osteoblasts and a critical grain size of 49-67nm for alumina was found for cell adhesion. The discrepancy in the conclusions could be explained by differences in cell type and culture conditions but in any event comparisons between the studies are difficult to draw.

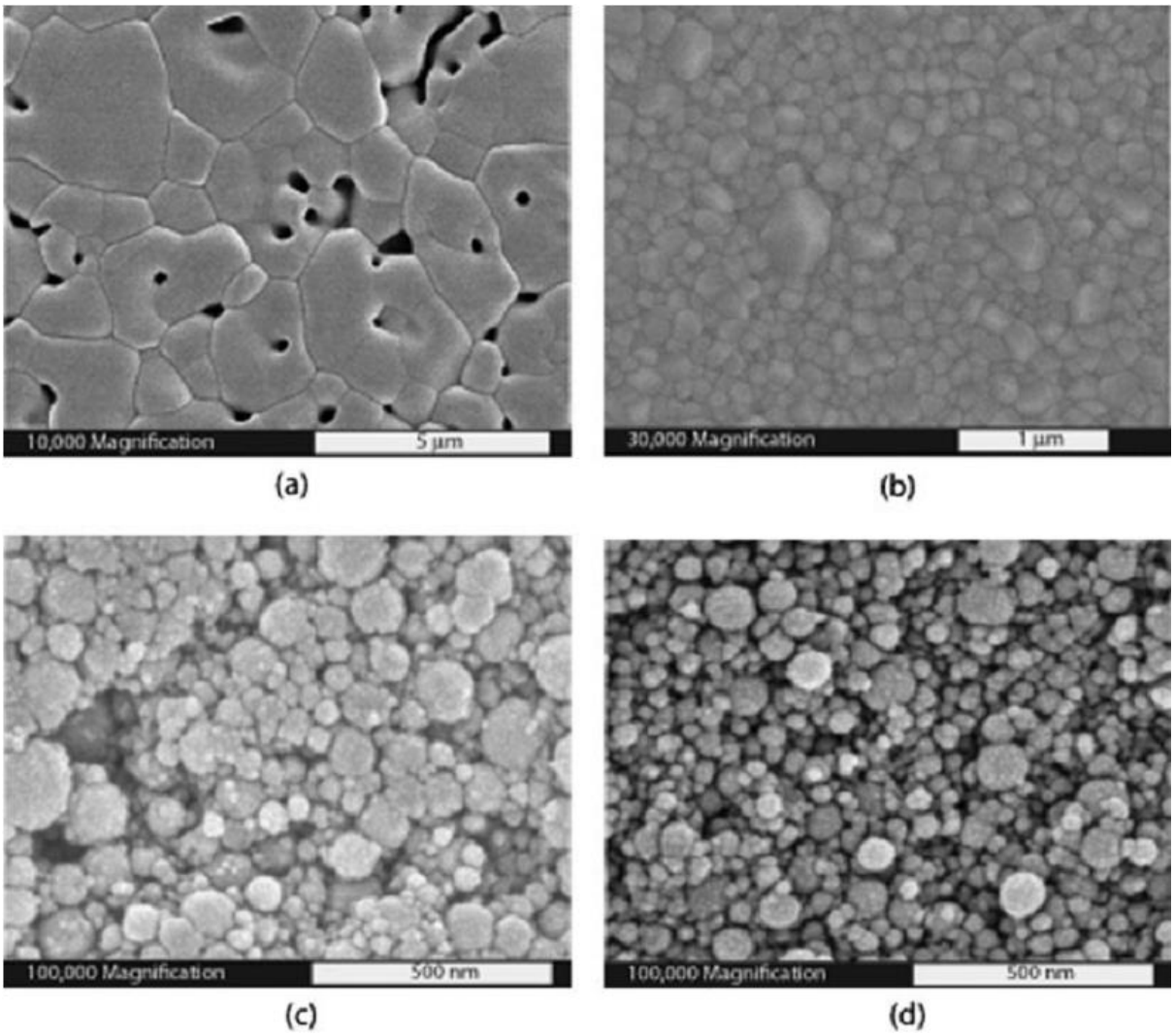

Figure 2.7. *SEM images of various surfaces described by Dulgar-Tulloch et al. (a) 1500nm alumina, (b) 200nm HA, (c) 50nm titania, and (d) 24nm alumina [38].*

Overall, there appears to be a scarcity of work done on this topic. This fact, combined with the ease of implementation of a sintering temperature study, strongly suggest that varying the sintering temperature of the HA as a potential surface manipulator is a worthwhile endeavour. In addition it should be noted that, although grain-size is a somewhat subjective measurement[5], its use in the Dulgar-Tulloch study gives a hint that perhaps basic surface

[5] It often depends on the analysis of manually thresholded images which can lead to inconsistencies.

roughness parameters (R_a, R_q, S_a, S_q, etc.) are not the ideal descriptors for tissue engineering surface topographies.

2.3.3 Phase Addition

The addition of further metallic or ceramic phases to calcium phosphates in order to modify their material properties is an established technique. However, it is generally performed with the express intention of increasing the mechanical strength of the main calcium phosphate phase [42]–[48]. Although there is a general concern with maintaining biocompatibility, little attention has been paid to how the addition of these phases affects surface topography. Some interfacial reactions are likely inevitable, however in theory it should be possible to use a doping phase that will remain proud from the surrounding HA matrix during sintering thus forming relevant topographical features to stimulate a cell response. Alumina and zirconia seem ideal candidates due to their stability and high melting temperatures (2072°C and 2715°C respectively) compared to HA (~1100-1250°C).

An example of a detailed study on this topic, albeit with little analysis of actual surface topography, is another from Webster's group mentioned above; by Evis *et al.* [49]. The paper details the addition of zirconia to HA in various doses (10, 25 and 40wt %) and sintered at various temperatures (900-1300°C). A homogeneous mixture was achieved by ball-milling the powders prior to sintering. Human osteoblasts were found to adhere most onto substrates with low zirconia contents (10wt %) and low sintering temperatures (900°C); these parameters correspond with the smallest grain-sizes achieved of approximately 160nm. Although pure HA appears to be used as a material analysis control at all sintering temperatures, a major weakness apparent here was that no indication was given of its performance in the cell adhesion assays. Thus it becomes impossible to tell whether or not the addition of the zirconia was an improvement on the biocompatibility of the HA. Furthermore, no mechanical testing has been performed so we cannot

even confirm that the zirconia acted as intended to strengthen the HA matrix. Secondly, if we are to accept that grain-size is an important topographical descriptor, then we must conclude that this study showing the smallest grain-sizes of 160nm giving the greatest cell adhesion, disagrees with Dulgar-Tulloch *et al.* [40] who conclude that grain-sizes above 200nm are best for cell adhesion. However this difference is small and may be attributable to variations in methodology. Finally, it is interesting to note that here Evis *et al.* have succeeded in correlating a surface roughness (R_{RMS}) with cell adhesion. Higher roughness values which are produced at the lower sintering temperatures correspond to the best cell adhesion. If anything, this simply serves as another confounding factor as it is impossible to tell what the dominant parameter is affecting the differences in cell response; grain-size, surface roughness, or indeed material chemistry which is not dealt with at all.

Despite the relative lack of concern with the topographical effects of phase addition to hydroxyapatite, it is clear that the process, particularly when coupled with high sintering temperatures, can result in phase changes [50], [51]. This effect would need to be monitored in any study involving composite sintering of biomedical ceramics.

2.3.4 Surface Characterisation

Surface quantification in general is a non-trivial problem. Even amongst the tribology research community, the standard height-based descriptors such as R_a and R_{RMS} are being labelled as too simplistic to describe most real-world surfaces on their own. There is an argument that provided the surfaces under examination all have a reasonably similar underlying waveform, all that is required to differentiate them is a height-based parameter [52]. Even then, when peak counts are important, e.g. as contact points in bearing surfaces, the standard parameters are losing favour [53]. The simplicity of these descriptors means that, alone, they are limited in their ability to ably describe a non-uniform surface. This is a particularly pertinent issue in tissue

engineering where many surfaces will be pseudo-random or at least non-uniform in morphology. Thus, some though should go into choosing a descriptor or descriptors for a particular surface and this choice should be backed-up by some common sense analysis of high magnification microscopy, e.g. SEM.

It is apparent from the literature that most tissue engineering research groups have not considered the above issues. This manifests as a huge variation in results. This can, of course, be attributed to a number of factors such as study scope, material choice, cell-type, surface treatment etc. However a major point is the lack of a standardized referencing system, not just for results comparison but also for characterization of the surface topography. Many authors avoid the issue of surface quantification altogether and simply qualitatively describe the sizes and shapes of their surface features; with the consensus being that features on an order of 30-400nm are most effective [29]–[31], [54]. Others prefer the more traditional surface roughness parameters of R_a and R_q and their three-dimensional counterparts S_a and S_q [55], [56]. Even more variation is evident here. At the nanoscale, cell responses have been observed on surfaces with R_a from ~195-519nm [55], while at the microscale the range can be ~4-74µm [56]. Clearly this situation is not ideal and a standardized measurement for surface topography in a tissue engineering context is required.

As an example of the lack of clarity on surface topography quantification, a study by Ito *et al.* [57] is interesting. The work consisted of culturing mouse osteoblast-like MC3T3-E1 cells on yttria stabilized tetragonal zirconia polycrystals with four different surface treatments; mirror polishing, 50µm and 150µm alumina blasting and acid etching. Their results showed no clear difference in initial cell attachment between any of the surfaces. However, cell proliferation was significantly higher on surfaces blasted with 150µm alumina. Despite this, they report no significant difference in the surface roughness height deviation (S_a) of any of the surfaces (Figure 2.8). Moreover, very little distinction is made between nano- and microscale topography.

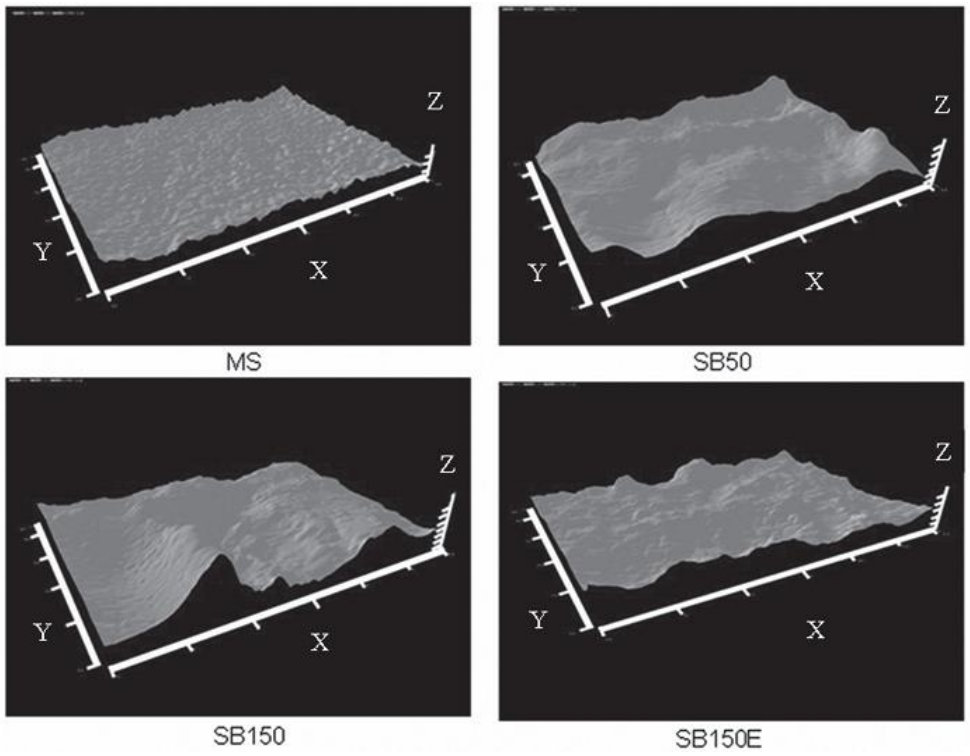

Figure 2.8. *Various surfaces described by Ito et al., X and Y axes are 1µm, Z axis is 0.05µm [53].*

As a result of these issues, it is difficult to draw specific conclusions from the studies available. What is clear is that surface topography has the ability to profoundly affect cell fate and viability and the results can manifest themselves in numerous ways. Thus, while there is still some way to go before an ideal implant surface is found, the technique itself merits further study. In fact, it may be the case that no surface treatment exists that can satisfy the three demands of biological compatibility, clinical relevance and commercial viability. If so, surface characteristics will need to be developed on a case-by-case basis taking into account manufacturability, cost, material limitations and implant requirements.

2.4 Scaffold Properties and Their Manipulation

Although the main focus of this work is the use of surface topography to improve the bioactivity of bone tissue engineering scaffolds, it is important to remember that often the manipulation of one parameter can have unexpected knock-on effects. Thus, care must be taken to ensure that while achieving the desired results in one area, other characteristics are not compromised.

2.4.1 Porosity and Mechanical Strength

It is logical that an increase in overall scaffold porosity will result in a decrease of the mechanical strength of the scaffold. For example, Jones *et al.* [58] describe a HA scaffold whose Young's Modulus decreases from 40GPa to 20GPa with an increase of porosity from 30% to 50%. Alumina scaffolds in the same study display a similar behaviour. Thus, despite the need for highly porous structures to facilitate the proliferation of cells and diffusion of nutrients, it is important that a suitable balance is found between porosity and strength so that the scaffold can be used in a load-bearing situation.

A confounding factor here is that the bulk material used to create the scaffold structure may, itself, contain a certain level of porosity. This usually manifests itself as a microporous phase as defined by Buckley *et al.* [4] in the range of 2 - 5µm, although nomenclature varies across the literature. Cordell *et al.* [59] analysed the effect of two sizes of microporosity, which they defined as 5.96µm and 16.2µm, on the mechanical properties of bulk HA and on scaffolds manufactured from the same material. They found that for bulk HA, strength in both bending and compression decreased with increasing micropore size. The larger pore samples were less reliable (smaller Weibull modulus) in bending but more reliable in compression. The group postulated that this apparent contradiction stemmed from the greater distribution in pore sizes in bending and the

decreased number of pores per unit volume in compression. The compressive strength of the HA scaffolds was similar for both pore sizes, this makes sense as the scaffolds are more likely to fail due to larger defects i.e. the mesopore phase. The average strength of the scaffolds of 8 MPa compares favourably with that reported for trabecular bone (1-7 MPa).

A more isotropic architecture will exhibit varying mechanical properties depending on its orientation. For example, lamellar-type scaffolds described by Fu *et al.* [60] displayed a compressive strength of ~10 MPa (at a strain of ~7%) when loaded parallel to the lamellae but only ~4 MPa (in a strain range of 2-10%) when loaded perpendicular to them.

Care must also be taken that the scaffold is not too strong as this can lead to stress shielding and associated bone loss due to under-stimulation of the surrounding cells [9]. Such a discrepancy is apparent in the Jones study [58] where they report values in the tens of gigapascals for the Young's Modulus of their scaffolds whereas their measured values for trabecular bone are between 1 – 5GPa.

2.4.2 Permeability and Interconnectivity

A scaffold with high permeability is desirable as it facilitates the initial seeding of cells through the structure as well as the transport of nutrients and waste products. In geology and environmental science, permeability and porosity can sometimes be related, although no fundamental law exists across all conditions. For example the Capillary Tube Model can be used to relate the two via the equation;

$$k = \frac{\varphi r^2}{8\tau}$$

Where k = permeability, φ = porosity, r = capillary radius and τ = tortuosity. However, in a bone tissue engineering scaffold, the situation is slightly more complex in that pores have varying

degrees of connectivity which must be accounted for i.e. a highly porous structure in which none of the pores are connected would be unable to allow cells to migrate through the matrix.

The general hypothesis is that pores need to have an accessible pore radius, i.e. the radius of the smallest sphere that can access the pore from outside, of >50µm to facilitate bone ingrowth [61], [62]. The Jones *et al.* study mentioned earlier [58] corroborates this by showing a strong correlation between accessible pore radius and bone ingrowth. Although scaffolds with an accessible radius >50µm showed greater bone ingrowth after implantation, the authors also found an upper cut-off of ~100µm for bone ingrowth. Clearly the degree of interconnectivity of the pore network is a sensitive parameter that should be examined on a case-by-case basis.

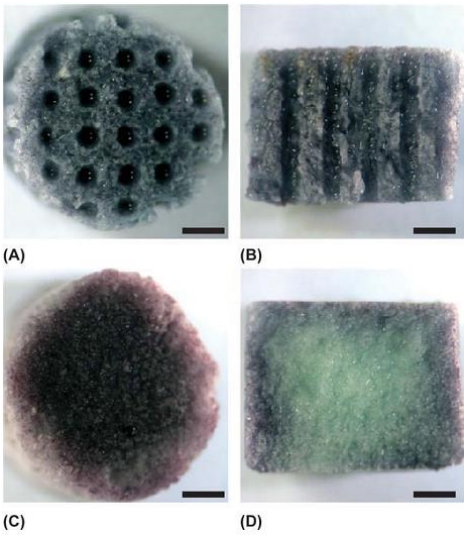

Figure 2.9. *MTT staining of cell viability on (A)(B) scaffold with macrochannels and (C)(D) scaffold without [15].*

As a way of increasing the permeability of the matrix post-manufacture, the addition of the macrochannels to the TCBE scaffold proved effective [4]. The permeability for the matrix without the channels was measured as $0.097 \times 10^{-10}\ m^2$; the macrochannels increased this to $1.71 \times 10^{-10}\ m^2$. The effect this had on the penetration of viable cells through to centre of the scaffold is clear (Figure 2.9).

2.4.3 Construct Vascularisation

It is estimated that *in vivo* no cell is ever further from a capillary than about 100-200µm [63]. This gives a fairly stark limit of what can be expected from diffusion of nutrients through a matrix. Several studies have elucidated the behaviour of vessel forming endothelial cells and have

described conditions that encourage their proliferation, motility and growth [64], [65]. However, more efforts are necessary to integrate a vascularisation technique into other areas of tissue engineering, as the necrotic core referred to by Buckley *et al.* demonstrates [4].

One such effort has been made by Trkov *et al.* [66]. They developed a micropatterned 3D hydrogel construct to investigate the interaction of endothelial and mesenchymal stem cells. Clearly, any such interaction will be highly pertinent to an attempt at a long-term bone tissue engineering implant. They found that bone marrow derived MSCs migrated in response to the proximity of endothelial cells. This was attributed to a chemotactic gradient created by secretion of chemokines by the endothelial cells. In addition, the MSCs acted to support the endothelial cells in the creation of a stable vascular network that consisted of long, highly-branched tubular structures resembling capillaries.

Although this work shows great promise for the ability of MSCs to support vasculogenesis, it is clear that an additional cell type, namely endothelial, is necessary. Thus, at some stage in any development of a novel tissue engineering strategy, the addition of an auxiliary cell type may well have to be considered and the potential repercussions associated with it.

In terms of seeding a scaffold with an angiogenic cell-line alone, avoiding co-culture, Handel *et al.* [67] report favourable results. An osteogenic 45S5 Bioglass®-based scaffold was seeded with human adipose tissue-derived stem cells (hASCs). The constructs were analysed using two metrics; an *in vitro* human umbilical vein endothelial cell (HUVEC) formation assay and an *in vivo* chorioallantoic membrane (CAM) angiogenesis assay. Improved angiogenesis was observed by both techniques and this was attributed to increased vascular endothelial growth factor (VEGF) provided by the hASCs. In fact, the improvement was noted on both Bioglass® scaffolds and fibrous controls (Figure 2.10) provided they were seeded with hASCs. This implies independence from any ionic dissolution from the Bioglass®.

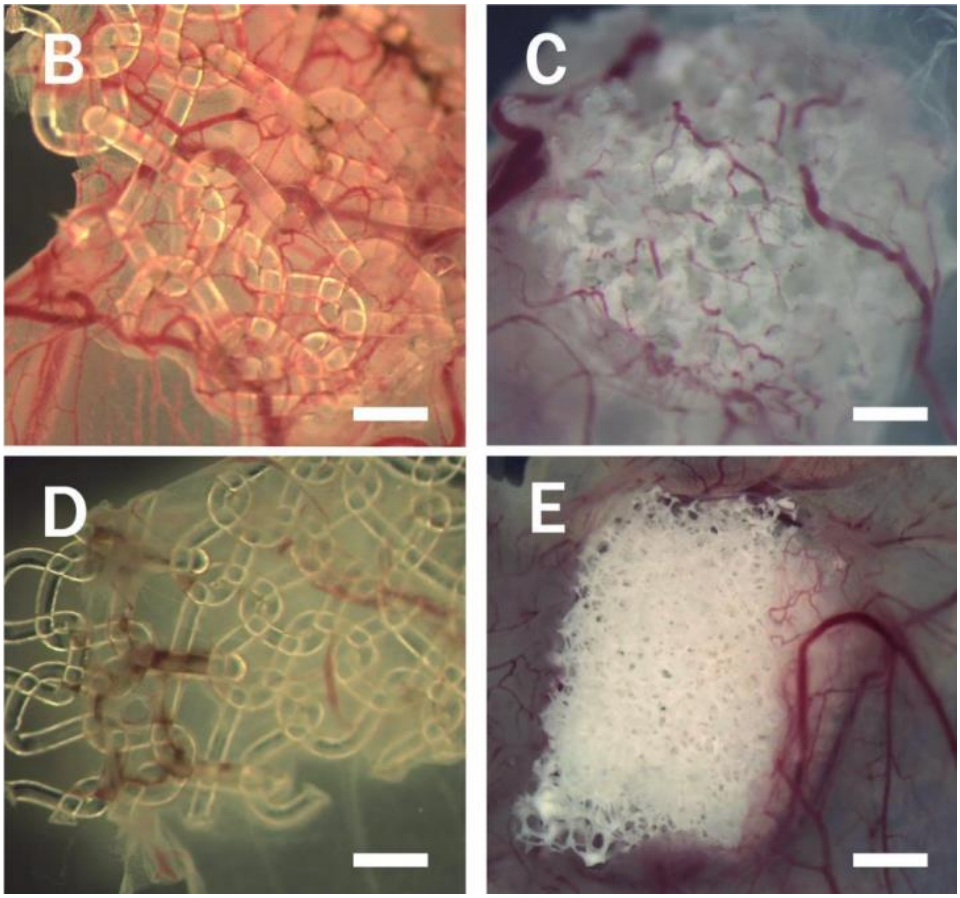

Figure 2.10. *(B) Fibrous and (C) Bioglass® scaffolds seeded with hASCs after investigation in the CAM angiogenesis assay compared with their counterparts seeded with (D and E) human fibroblasts. Scale bars = 1mm [63].*

Another approach would be to supply progenitor cells with supplementary angiogenic growth factor. This method was investigated by Helmrich *et al.* [68]. Here, VEGF was overexpressed in genetically modified human bone marrow-derived MSCs. The over-expression was found to significantly improve the vasculature of constructs both *in vitro* and in an *in vivo* nude rat implant. However, the increased VEGF was also found to increase osteoclast recruitment to the implant site which resulted in resorption and an overall decrease in bone mass. This is another example of a novel method having an unexpected effect and highlights the need for further investigation in this area.

In the Helmrich study, the authors also highlight the importance of the quality of vasculature, not just the quantity. It is not enough to simply increase the density of carrier vessels through a construct if diffusion of nutrients cannot occur through the vessel walls. The VEGF over-expression resulted in physiologically-relevant vascular networks with a high density of capillaries whose thin walls facilitate the exchange of nutrients. Conversely, the control samples produced networks consisting of predominantly conductance vessels. These are thick muscle cell coated arteries and veins which allow very little diffusion through their exterior. This result adds another caveat to the issue of angiogenesis in tissue engineering grafts and it is clear that more work is required before a particular method to increase blood vessel formation is adopted.

2.5 Inflammation

Inflammation is a term used to describe a whole suite of biological responses to a range of potential stimuli which result in protein synthesis and cell activation. As with any physiological system, bone exhibits an inflammatory response to trauma. While quite complex, the response is essentially a cascade of events and signals that regulate the healing process. Progenitor cells are recruited to the injury/infection site and their subsequent actions are regulated by an array of proteins and cytokines which can have both local and systemic effects [69]. Logically, an understanding of the effect of scaffold material and structure on this process is pertinent to the design of any implantable product. However inflammatory potential often seems to be ignored with most literature focussing on biocompatibility, manufacturability and the restoration of form and function [70]–[74]. Unfortunately, the value of these features could be overcome by implant-induced inflammation. While some inflammation is necessary for healing, it can also induce a range of responses that can compromise the health of both the host and the implant.

While there is evidence to suggest that calcium phosphates of various forms induce an inflammatory response [75]–[78], the specific mechanisms of the response are often poorly elucidated. More importantly, the potential consequences for the implant are frequently ignored. This is particularly relevant for implanted ceramic scaffolds as mesenchymal stem cells (MSCs) can contribute to the degradation of ceramics [75], exacerbating any inflammatory effect. Thus the inflammatory process is relevant from two points of view: the health of the recipient and the "survivability" of the implant.

Recent studies have described calcium phosphate induced inflammation, both *in vitro* and in animal models. Murine macrophages have shown increased production of pro-inflammatory cytokines IL-6 and TNF-α [77] while also displaying significant decreases in proliferation and phagocytosis when cultured in the presence of nanocrystalline hydroxyapatite. 1-50µm β-tricalcium phosphate (β-TCP) particles also induced an inflammatory response *in vivo* in mice. This

manifested as a significant migration of immune cells to the injection site. The inflammatory infiltrate included neutrophils, lymphocytes, macrophages and fibroblasts. In the same study *in vitro*, macrophages phagocytosed the β-TCP particles [76]. Sintering temperature of HA has also been suggested to correlate with inflammation [79]. Here, HA particles sintered at 1180°C induced higher levels of inflammatory cytokines TNF-α and IL-6 in human monocytes compared to particles sintered at 600°C. However, this study is limited in that only two temperatures were examined, both relatively low.

These studies all have in common a lack of clarity regarding the specific immune stimulus. Particle-size, chemistry, crystallinity etc. could all effect an immune response. In fact it has been suggested that grain shape may be a defining characteristic [78] with long, needle-like nanostructures the most likely to induce inflammation. And of course, it may also be a combination of any of the above. In addition, very little is known about the exact pathways that this inflammation is acting through. Although there is evidence to suggest that the TLR (toll-like receptor) pathway is involved [80].

In any case, it is clear that further study is required on what effect implanted calcium phosphates have on the immune system. More generally, inflammation is a complex area and its effects should be examined as part of any new implant design.

2.6 Observational Methods

2.6.1 Introduction

The “observer effect” is usually explained as being the act of measuring, in itself, altering the state of that which is measured. In all aspects of science it is important to remain aware of the potential consequences of using a particular metric to draw conclusions. An example from tissue culture would be using a media assay to analyse cell proliferation rather than counting the cells by eye. Aside from the practical benefits of the assay, MSCs start to die when not attached to a surface and generally they need to be removed to be counted. Thus, cell death might lead to inaccuracies in the results. That is not to say that an assay has no effect on the cells, but it is to be hoped that it would be much kinder than counting.

Of course there are also more mundane reasons for modifying or developing new analysis techniques; cost, efficiency and practicality among others.

2.6.2 Cell Proliferation Media Assay

Assessing cell proliferation is the most logical way of determining a tissue engineering scaffold or biomaterial’s viability. The most basic was of doing this is to simply count the cells either unaided [33] or in conjunction with a stain [64]. However, this method is usually destructive as it involves removing the cells from the surface of whatever material is under investigation. This is adequate if only one timepoint is being considered but problems arise when regular, continuous measurements are required. It is also time consuming and there is always a risk that some cells may remain on the surface thus confusing the results.

In general a media assay is preferable as it allows the same samples to be used for each timepoint due to the fact that the media is removed and analysed leaving the cells unharmed. Assays generally involve adding a chemical to the media and measuring a colour change based on

cell activity. There are numerous assay techniques available to measure the metabolic activity of cells, some common ones being live/dead staining, DNA assays and MTT assays. There are pros and cons to all, e.g. the MTT assay is very sensitive to the conditions under which it is performed. And, in addition, most require a high level of expertise and finance.

One of the most popular activity assays is AlamarBlue®[81], [82]. The active ingredient in AlamarBlue® is a compound called resazurin. Over time, cells metabolise the resazurin and reduce it to resorufin which fluoresces [83]. By measuring the difference in fluorescence of each sample the activity of the cells and, thus, their proliferation can be assessed.

The main drawback to AlamarBlue® is its expense. As a result, a cheaper alternative that performs to a similar standard is highly desirable. One way of doing this is to obtain the compound resazurin sodium salt in its powdered form and to mix up a solution “in-house”. This has been done before on a rougher scale to detect the presence of bacteria [84], [85]. Such a solution would also be useful as a more sensitive between-group comparator if employed using an AlamarBlue® protocol as each experiment provides its own controls [83]. Magnani *et al.* [86] used a similar protocol to detect changes in the metabolism of serum-starved PC-12 neural cells. They concluded that the technique was cheap, easy to implement and readily automatable.

While the resazurin technique is simple, easily applied and very cheap it does have some limitations that would not normally be associated with commercial assays. One, there is no general standard; a new batch of resazurin is made up for each experiment, this allows only comparisons of groups within individual experiments. Two, the assay relies heavily on the accuracy of the performer for its repeatability; again due to the need for a new mixture for each experiment. Despite these drawbacks, it was felt that the simplicity and volume provided by the resazurin technique far outweighed them and this was the method of choice adopted for proliferation measurement over the course of this work.

2.6.3 Cell Types

It is standard practice when assessing the *in vitro* performance of scaffolds intended for bone tissue engineering to use some form of mesenchymal stem cell. This makes sense as the MSC is one of the key responders to injury of skeletal tissue and has the potential to differentiate along the osteoblastic lineage. However there are potential problems when the aim is to measure the metabolic rate of MSCs and these stem from their pluripotency. While they are proliferating, the MSC metabolic rate is fairly steady [87]. However, when they differentiate their metabolism can change. Thus it is important to verify that any changes in metabolic rate observed are due to proliferation rates and not differentiation. Differentiation in itself is not necessarily undesirable and, in fact, may be unavoidable given that the cells will be cultured on calcium phosphates [88]. But the primary purpose of this project is to increase proliferation.

With this in mind, other cell types may be used to verify any conclusions drawn from the MSC results. A suitable example would be murine THP1 cells. These are derived from mouse bone marrow and are non-adhesive macrophages. They have a number of positive attributes including being another important cell involved in injury response. And their non-dependence on adhesion means they provide a counterpoint to the purely adhesive MSCs.

2.7 Research Objectives

Project Aim: *Define, produce and evaluate an optimized ceramic scaffold for use in oro-maxillo-facial bone tissue engineering.*

To achieve this aim, the following objectives are intended:

1. Induce topographical changes in HA scaffolds by
    a. Sintering temperature variation.
    b. Nanophase addition.
2. Develop a method for quantifying surface topography in a manner relevant to cell behaviour.
3. Monitor phase stability.
4. Assess surface performance using cell activity and thus determine the effectiveness of surface topography as a method of enhancing cell proliferation on HA scaffolds.
5. Compare the optimized scaffold to an industry competitor using the metrics of cell activity and inflammatory response.

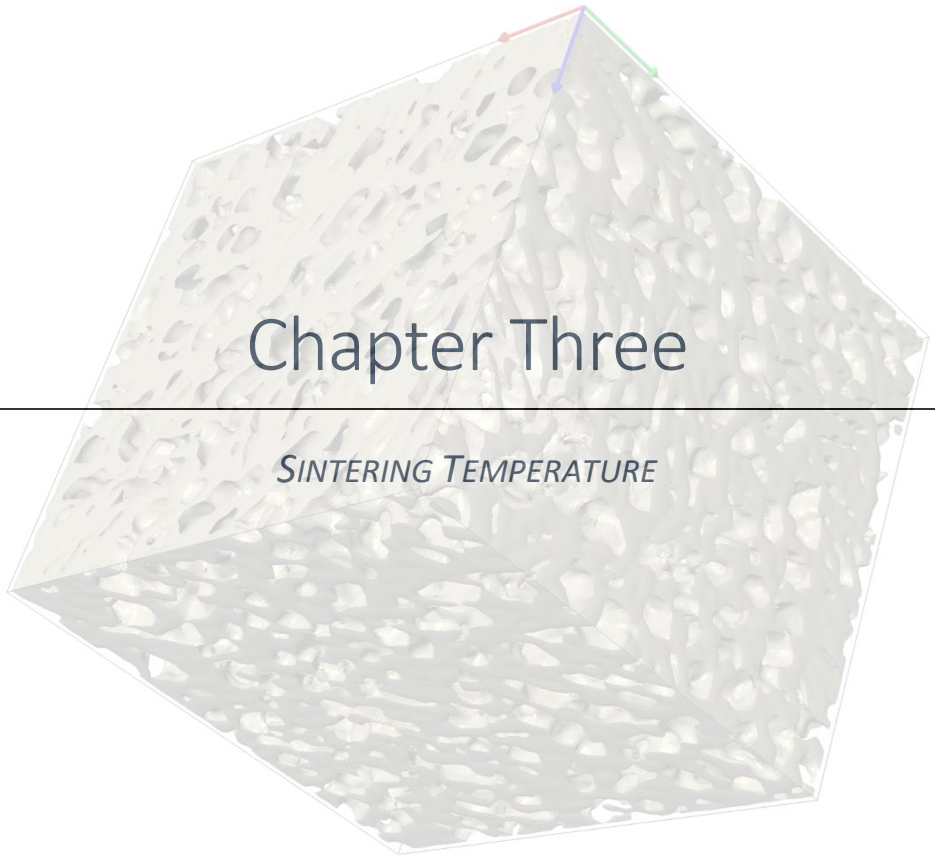

Chapter Three

SINTERING TEMPERATURE

3.1 Introduction

The first method employed to alter the surface topography of the scaffolds and, thus, attempt to increase cell activity, was modulation of the sintering temperature. Not only is this an easy and inexpensive parameter to control but it fits with the general brief of keeping the whole manufacturing process within the bounds of industrial scalability. In addition, as discussed in Chapter 2, it is important that any manufacturing parameter used to affect the surface topography be able to work throughout a three-dimensional pore structure. Sintering temperature fulfils this criterion.

3.2 Materials and Methods

3.2.1 Scaffold Manufacture

3.2.1.1 Green Body Preparation

Scaffolds were manufactured using a freeze-drying and sintering technique previously described by Buckley [4]. The HA (puriss., ≥90%) (Sigma-Aldrich, catalogue number 04238)[6] precursor powder was gradually added (final solid content of 38%w/v) to a conical flask containing 2wt% (to 100wt% precursor powder) Darvan 811 dispersant (RT Vanderbilt Company Inc., Norwalk, CT, USA) and the correct volume of deionised water. The suspension was mixed manually before slowly adding Methocel 60HG binder (Sigma-Aldrich) to yield a final concentration of 2.5%w/v. The suspension was further homogenised in a Turbula mixer (WAB Ltd., Welwyn Garden City, UK) at 23rpm for 12 hours.

The suspension was cast into stainless steel rings (Stock, Dublin, Ireland) sealed on one side with Parafilm and placed on the cooling shelf of a VirTis AdvantagePlus freeze-dryer (SP Scientific, Suffolk, UK). Samples were then subjected to a freeze-drying cycle (Table 3.1).

[6] No data was available on the particle size or size distribution of this batch of HA.

Step	Temp. (°C)	Time (mins)	Ramp/Hold	Pressure (Torr)
1 (Start)	20	10	Hold	760
2 (Ramping)	-40	65	Ramp	760
3 (Temp. Hold)	-40	60	Hold	760
4 (Drying)	-40	5	Hold	0.2
5 (Drying)	0	160	Ramp	0.2
6 (Drying)	0	1020	Hold	0.2
7 (Drying)	20	40	Ramp	0.2
8 (Drying)	20	30	Hold	0.2

***Table 3.1**. Detail of the scaffold freeze-drying cycle.*

3.2.1.2 Wax Infiltration

To facilitate cutting and shaping, the green bodies were infiltrated with paraffin wax (Fluka). The wax was melted in Pyrex dishes. The green bodies were placed gently on top of the wax and allowed to submerge under their own weight. The dishes were then placed in a vacuum oven (Binder, Tuttingen, Germany) and the vacuum applied and held for 15 minutes at 65°C. Once removed from the oven, the green bodies were removed from the wax bath and allowed to cool to room temperature.

3.2.1.3 Wax Removal and Sintering

Scaffolds were cut to desired size and shape and placed in Pyrex dishes. The bulk of the wax was removed by melting in an oven at 65°C for an hour. Scaffolds were placed in alumina crucibles and sintered in a chamber furnace (Lenton, Hope, UK) under the following regime.

1. Ramp at 3°C/min up to 250°C.
2. Hold for one hour to facilitate burnout of organic components.
3. Ramp at 3°C/min up to maximum sintering temperature (1100-1350°C).
4. Hold for three hours.
5. Ramp at 3°C/min to room temperature.

3.2.2 Disk Manufacture

In order to investigate the effects of topography on cell behaviour, the scaffold pore surfaces were modelled using two-dimensional disks. These were made from the same precursor powders as the scaffolds and pressed as lightly as possible to maintain an accurate simulation of the surface morphology created by the freeze-drying and sintering processes. This approach removes any confounding factors such as pore-size and shape.

The 2D HA discs were made by lightly pressing 200mg of the precursor powder for two minutes in a ø13mm die (International Crystal Laboratories, Garfield, NJ, USA) followed by sintering in a chamber furnace (Lenton, Hope, UK). The sintering regime was as described for the scaffolds.

HA disks exhibiting a variety of surface topologies were produced by varying the maximum sintering temperature. These were then sintered to final temperatures of 1100, 1150, 1200, 1250, 1300 and 1350°C.

3.2.3 X-Ray Diffraction (XRD) Analysis

It was important to define the phases present in the samples as the sintering temperature was increased from 1100-1350°C. High-temperature decomposition of HA into tri-calcium phosphate (TCP) can be a problem and this would present a confounding factor in the ensuing analysis. Hence, phase stability was monitored using XRD. Appendix I offers further discussion on the varying stability of HA powders from different sources.

XRD was carried out on powder samples that had been mixed and sintered to the same specifications as the scaffold precursors. The machine used was the Bruker D5000 in TCD Geochemistry which has a 2.2 kW Cu long fine focus (0.4 x 12mm filament). The following optical configuration was used: 2.5° primary soller, 2 mm aperture diaphragm, 2 mm scattered radiation diaphragm, 2.5° secondary soller, 0.6 mm detector diaphragm and a secondary curved graphite monochromator ahead of the scintillation counter. Sample measurements were made at 1 sec/ 0.02° step from 10 to 65 °2Θ at 40 kV and 40 mA. Sample rotation was used.

3.2.4 Scanning Electron and Helium-ion Microscopy

The best way to get a qualitative expression of the surface topographies at cellular length scales was electron microscopy. These versatile instruments allow high-resolution imaging at the nanoscale. This technique was imperative for confirming that the surfaces of the 2D disks matched the pore surfaces of the 3D scaffolds. In addition it allowed the cells to be observed directly on the surfaces, providing confirmation of adhesion and morphology.

Initially, the temperature controlled samples were imaged using a Zeiss Ultra Scanning Electron Microscope (Carl Zeiss Microscopy, Jena, Germany). All samples were carbon coated using a sputter coater (Cressington Scientific Instruments, Watford, UK) prior to imaging. Cells were fixed to the surfaces in 3% gluteraldehyde (Merck, Hohenbrunn, Germany) for two hours,

followed by dehydration, in 10 minutes stages, through a series of ethanol concentrations (10%, 30%, 50%, 70%, 95%) followed by 30 minutes in 100% ethanol and atmospheric evaporation.

Where possible, samples were imaged using a Zeiss Orion Helium-ion microscope (Carl Zeiss Microscopy, Jena, Germany) which eliminated the coating step. Cells were fixed in the same way as before. The He-ion system gives greater depth of field than traditional SEM and the lack of need for a coating makes the images more accurate. Images are labelled clearly depending on what form of microscopy was used.

3.2.5 White-Light Interferometry

SEM and He-ion microscopy give excellent images of the substrates. However, they offer no quantitative information on the surface topographies. A standardised quantitative descriptor was highlighted in Chapter 2 as having a key role in bringing clarity to the literature on the topic of tissue engineering scaffold topography. White-light interferometry was used to gather the raw data from which such descriptors can be drawn.

White-light interferometry was performed in the TCD Centre for Microscopy Analysis. The system used for image capture was an Omniscan MicroXAM interferometer running Mapvue AE 2.27.1 capture software. Scan sizes were $1mm^2$. Images were analysed using Gwyddion v2.37 [89].

3.2.6 Cell Culture

3.2.6.1 MSCs on HA Disks

Surfaces were assessed based on their tendency to increase proliferation of MSCs. The proliferation of the cells was measured using the expression of their metabolic activity. High

activity corresponded with high levels of proliferation. The relationship between cellular activity levels and cell numbers is discussed in Appendix II.

Prior to culture all samples were sterilized by heating to 121°C for one hour in a vacuum oven (Binder, Tuttingen, Germany). All samples were seeded with porcine bone-marrow-derived MSCs at a density of 40,000 per well. Samples were incubated at 37°C for four hours before adding 500µl of media consisting of Dulbecco's Modified Eagle Medium (DMEM) Glutamax (Gibco, Dublin, Ireland), 10vol% foetal bovine serum, 2vol% penicillin/streptomycin and 0.1µl/ml amp-B (all Sigma-Aldrich) to each. Cells were cultured for various periods up to one month at 37°C and assayed for metabolic activity every three or four days. Cells cultured directly on tissue-culture plastic were used as a control.

3.2.6.2 MSCs with HA disks – Non-Contact

It was noted that, although culturing the MSCs directly on the HA substrates would show any general differences in response, this experimental set-up would be unable to differentiate between effects caused directly by the surface topography and those caused by any potential ionic diffusion or particulate dissolution products. To account for this, MSCs were also cultured in the presence of the substrates but not in direct contact with them (Figure 3.1).

The general culture conditions were the same as those described for the contact experiment described above. After seeding on tissue culture plastic, the cells were allowed four hours to adhere. The HA samples were then introduced; contained in Millicell culture plate inserts (Merck Millipore Ltd., Cork, Ireland) with a polycarbonate membrane mesh of pore size 8µm. 500µl of media was added and the culture and assays proceeded as before. This setup allowed the cells and samples to occupy the same media with free association allowed through the insert

membrane but without direct contact. Cells cultured in the absence of substrates both with and without inserts were used as controls.

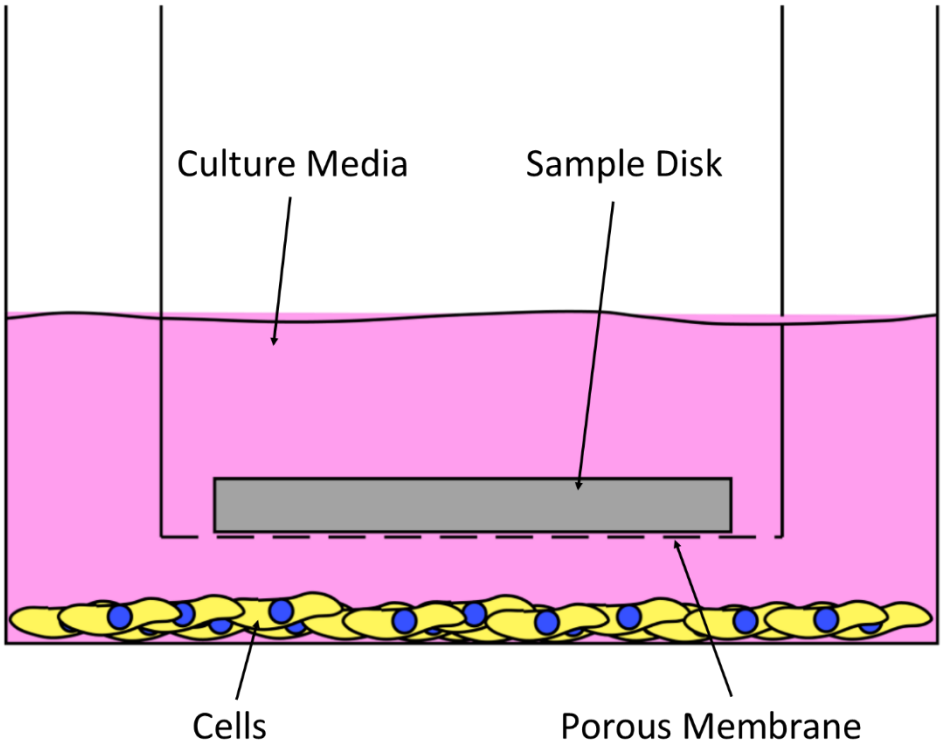

Figure 3.1. *Schematic of the experimental set-up for the MSC non-contact study.*

3.2.6.3 THP1 Macrophages on HA Disks

As a further test of the non-surface effects of the HA substrates, samples were analysed using non-adherent THP1 murine macrophages. This cell line has the additional characteristic of being non-differentiating, allowing a further comparison with the MSCs. The THP1s were seeded at a density of 100,000 per sample.

Due to the non-adherent nature of these cells, it was not possible to assay the same samples across multiple timepoints. Instead, individual samples were cultured to specific

timepoints. Media refreshment was achieved by removing half the old media and replacing with new. This is possible due to the fact the cells tend to sink and aggregate at the bottom of the well.

3.2.7 Resazurin Media Assay

Proliferation and activity of both MSC and THP1 cells was assessed using a media assay very similar to AlamarBlue® but non-proprietary. A 1mg/ml solution of resazurin sodium salt (Sigma-Aldrich) in deionised water was prepared, sterile-filtered and stored at 4°C (for up to one week).

At regular intervals, the samples were removed from the incubator, the old media removed and new media consisting of 10vol% resazurin solution was added and the samples returned to the incubator for four hours. This resazurin media was removed from the wells and 100µl from each sample was added to a Nunc black 96-well plate (Fisher Scientific) in triplicate. After the assay the samples were gently washed with phosphate buffered saline (Sigma-Aldrich) to remove any excess resazurin before being returned to the incubator.

During incubation the cells partially reduce the resazurin to resorufin which fluoresces. This fluorescence (at excitation 530nm, emission 590nm) was then measured using a Synergy HT microplate reader (BioTek, Winooski, VT, USA). The percentage reduction of resazurin was calculated using the formula

$$\%\, reduction = \frac{S_x - S_{control}}{S_{100\%\, reduced} - S_{control}}$$

Where S_x is the fluorescence signal of the sample at day x, $S_{control}$ is the signal generated by a 10%vol resazurin media solution and $S_{100\%\ reduced}$ is the signal of the 100% reduced resazurin solution (generated by autoclaving a sample of the control at 121°C for 15 minutes).

Due to the non-adherent nature of the THP1 cell type, it was not possible to culture each of these samples longitudinally as before. Hence, at each timepoint three samples from each group were selected and 50% of their media removed with care being taken not to disturb the cells at the bottom of the well. A double concentrate resazurin solution was then added to these wells and incubated for four hours as before. This solution was analysed as described above.

3.2.8 Statistical Analysis

All experiments were duplicated. Groups were evaluated using one-way analysis of variance (ANOVA) and Tukey's comparison test. A sample number, n, of six was used for all studies apart from the THP1 cells on the HA substrates; in this case an n of three was used. Results with a $p \leq 0.05$ were considered significant. All analysis was performed in Minitab (Minitab Ltd., Coventry, UK). Graphs were produced in GraphPad Prism 5 (GraphPad Software Inc., La Jolla, CA, USA).

3.3 Results

3.3.1 Surface Morphology

3.3.1.1 Disk Morphology

By varying the sintering temperature from 1100-1350°C, a range of surface morphologies was achieved (Figure 3.2). The HA particles did not fully sinter together at the lowest temperatures which resulted in a discrete, granular topography most pronounced at 1100°C and 1150°C. This contrasts with the higher temperatures where the individual HA particles fused into large, glassy grains. Average feature sizes at 1100°C were approximately 500nm while at 1350°C they were on the order of 10µm.

3.3.1.2 Scaffold Morphology

The SEM images reveal some similarity between the morphologies of the disks and those of the scaffolds sintered under the same conditions (Figure 3.3). The topography is a little harder to identify in 3D due to the porosity of the scaffold matrices. However, small granular features are clear at low temperatures, ranging up to smooth, glassy surfaces at high temperatures. This resemblance was taken as support for the assumption that the disks are appropriate models for the freeze-dried scaffolds.

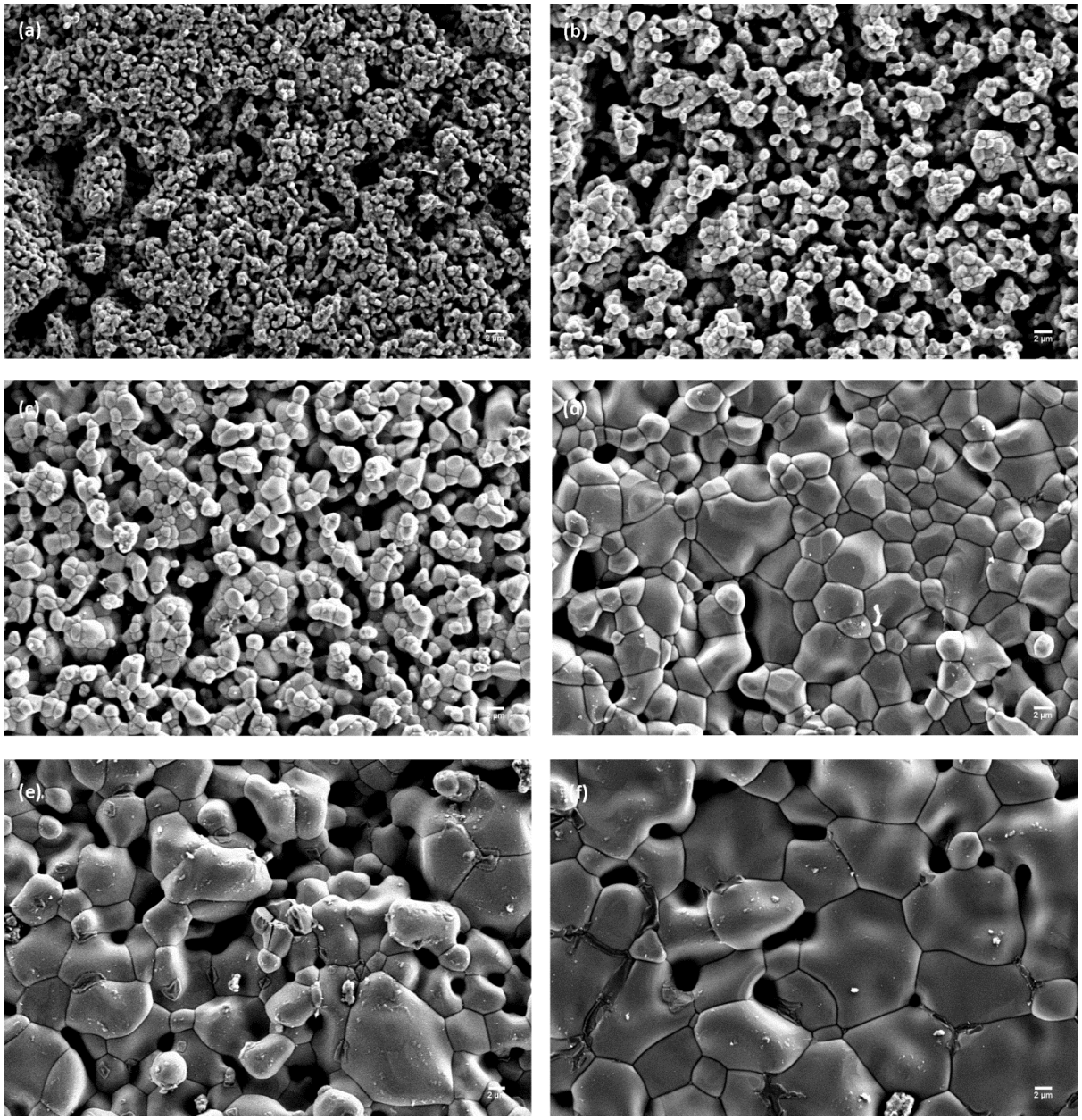

Figure 3.2. *SEM images of HA disks sintered from (a) 1100°C – (f) 1350°C. Scale bars are 2µm.*

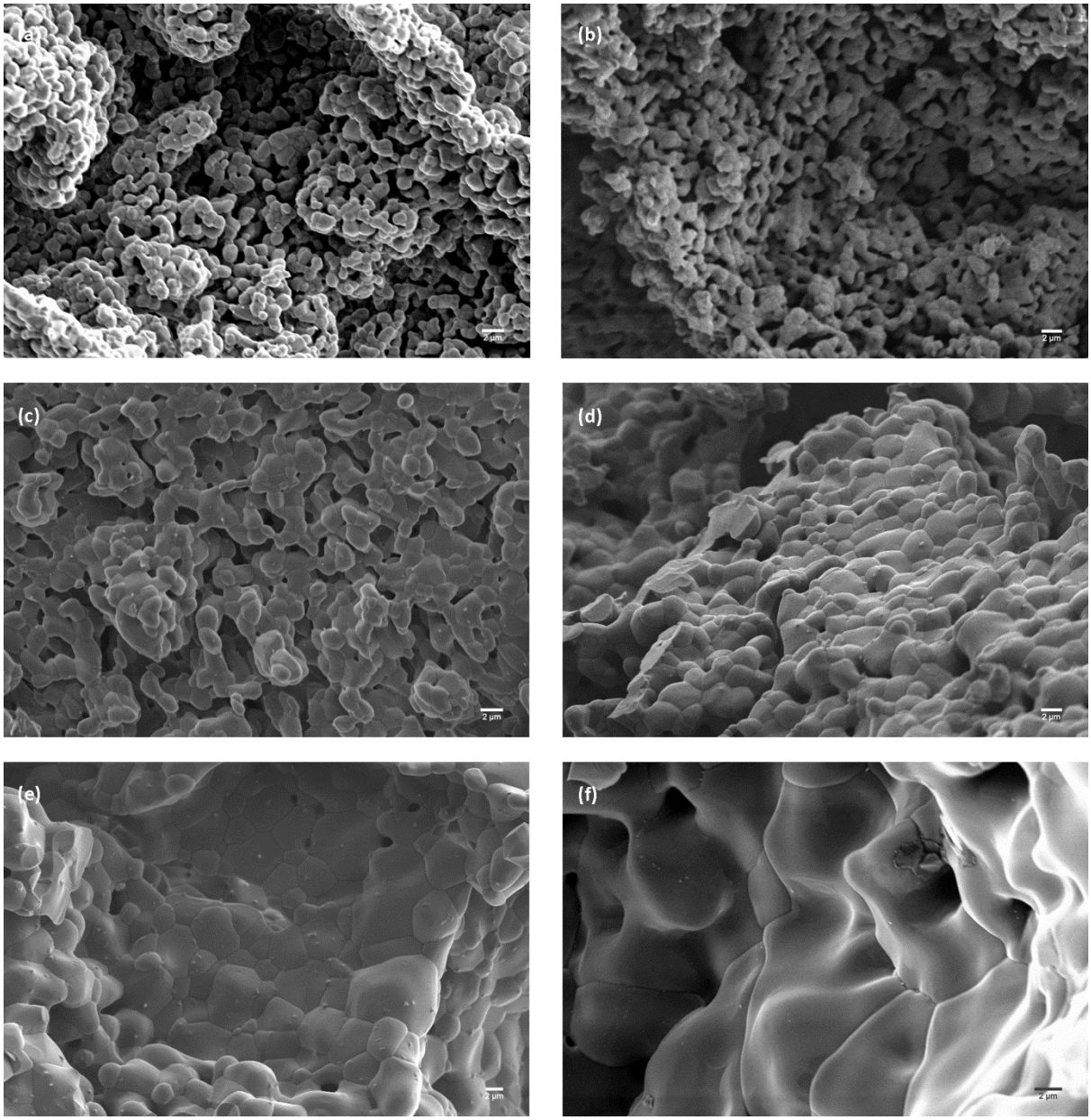

***Figure 3.3**. SEM images of HA scaffolds sintered from (a) 1100°C – (f) 1350°C. Scale bars are 2µm.*

3.3.2 Surface Quantification

One of the major problems in using surface topography as a biological tool is finding a way of quantifying it rigorously. This is explained in more detail in Chapter 2 but the salient point is that there is no consensus in the literature on how to numerically describe a tissue engineering

surface to best effect. Here, white light interferometry was used to gather quantitative data on the various surfaces.

Despite the obvious variations in surface morphology apparent in the SEM images of the HA substrates (Figures 3.2 and 3.3), the most commonly used surface descriptors were unable to differentiate them. This data is summarised in Table 3.2. Here, R_a and R_q were taken from the average of four independent line profiles drawn across 10,000µm^2 regions of interest of the full 1mm^2 scans. S_a, S_q and S_{dr}, being three-dimensional parameters, were computed statistically by Gwyddion directly from the regions of interest. As can be seen from Table 3.2 there are no obvious trends in the data as sintering temperature is increased.

	1100°C	**1150°C**	**1200°C**	**1250°C**	**1300°C**	**1350°C**
R_a (µm)	0.1138	0.1098	0.078	0.0836	0.16	0.124
R_q (µm)	0.1526	0.1502	0.11	0.1112	0.216	0.168
S_a (µm)	0.475	0.404	0.41	0.332	0.76	0.6
S_q (µm)	0.599	0.514	0.51	0.419	0.93	0.79
S_{dr}	1.2	1.19	1.12	1.12	1.31	1.21

Table 3.2. *Common surface descriptors for HA substrates sintered from 1100-1350°C. Note the lack of any coherent trends.*

The number selected to describe the surfaces presented here was the average surface wavelength. This is a hybrid parameter and so gives more information than a more basic number such as R_a alone. The average wavelength of a line profile is given by the formula;

$$\lambda = 2\pi \frac{R_a}{\Delta_a}$$

Where R_a is the average roughness of the profile and Δ_a is the absolute average slope computed from each consecutive data point in the profile. Hence, the surface wavelength describes a combination of the amplitude of the topography and the spacing of the features. Both of which, intuitively, might be relevant to cell response.

The raw data from the white light interferometer was imported into Gwyddion and four line profiles drawn from each 1mm^2 scan; a centred vertical and horizontal profile; and the two corner-to-corner diagonals. The average wavelength of each set was then plotted (Figure 3.4).

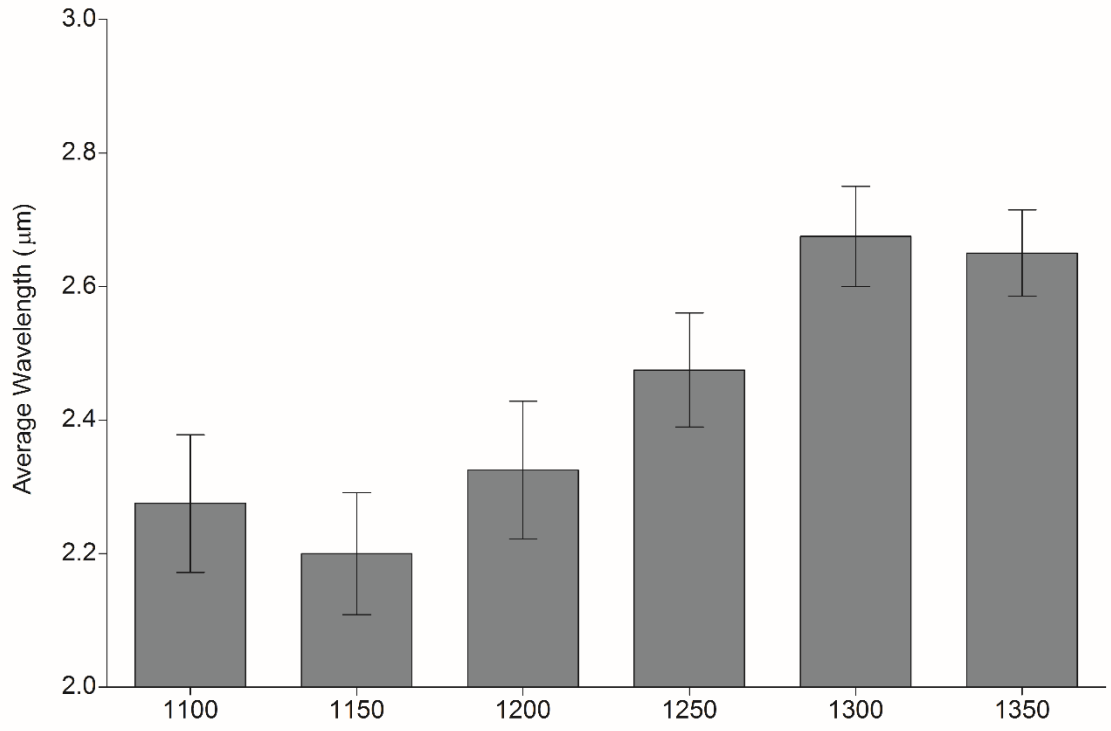

Figure 3.4. *Average surface wavelengths of HA disks sintered from 1100-1350°C. Bars are one standard error from the mean of four measurements. An increasing trend is apparent from 1100-1350°C.*

A one-way ANOVA revealed that both the 1300°C and 1350°C groups have significantly longer wavelengths than the 1100°C and 1150°C groups ($P = 0.04$). The overall trend of increasing wavelength with temperature is also apparent.

It is also notable that, although significance was not captured by the ANOVA, when isolated and analysed by t-tests, both the 1300°C and 1350°C groups are distinctly elevated from the 1200°C group ($P < 0.05$).

3.3.3 Phase Stability

It is natural to assume that the act of high temperature sintering would affect the phase composition of the HA in some way. The literature notes that in particular, HA has a tendency to decompose into α-tricalcium phosphate at higher temperatures (See Appendix I). Before any conclusions were drawn about the efficacy of the various topographies described above, it was important to ensure that they remained chemically similar. XRD was employed to achieve that aim. Figure 3.5 shows a comparison of the XRD patterns of unsintered HA; and HA sintered at 1100°C, 1250°C and 1350°C. The other temperatures were omitted for clarity.

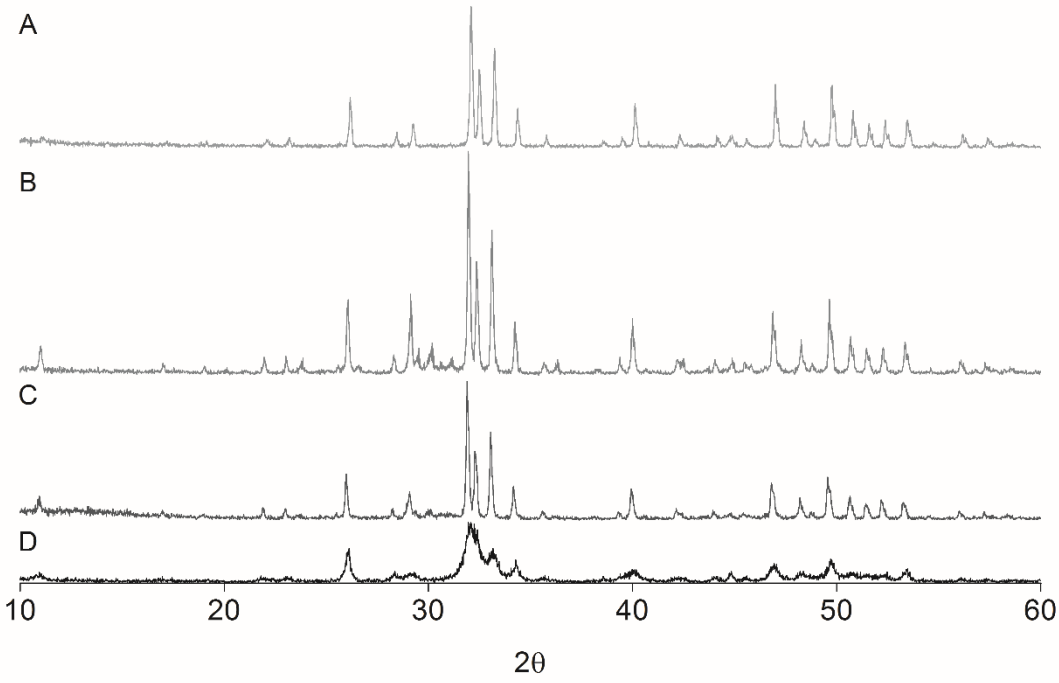

Figure 3.5. *XRD patterns of (a) HA sintered at 1100°C, (b) HA sintered at 1250°C, (c) HA sintered at 1350°C and (d) unsintered HA. The data shows that phase stability was maintained across the temperature range.*

The XRD data clearly shows phase stability was maintained across the four samples. The three large peaks at 2θ values of 31.8°, 32.2° and 32.9° are indicative of the HA phase. If decomposition had occurred to α-TCP, significant peaks at 30.7° and 34.2° would be expected instead; these were not apparent here.

The increased crystallinity of the material achieved upon sintering is also apparent. This is signified by the increased definition and height of the peaks of the sintered samples compared to the unsintered.

3.3.4 Cell Response

3.3.4.1 Contact MSC Response

The best *in vitro* test for the efficacy of a particular surface topography is to culture cells on it and observe their responses. Here, porcine, bone marrow derived mesenchymal stem cells were employed as they are cheap, readily available and are widely used in literature to analogue bone cell behaviour.

HA disks sintered at 1300°C consistently induced higher cell responses than the other groups and the tissue culture plastic control over 19 days of incubation (Figure 3.6). By day 19 the 1350°C samples also outperformed the control ($P = 0.02$) and were statistically indifferent from the 1300°C (Figure 3.7).

The most striking result was the complete lack of cell life observable on the 1100-1200°C surfaces. This was not just a lack of proliferation as it was evident from the very first timepoint at 24 hours. Clearly, the MSCs were unable to adhere to those surfaces sintered below 1250°C and, as they cannot survive for more than a few hours in suspension, subsequently died.

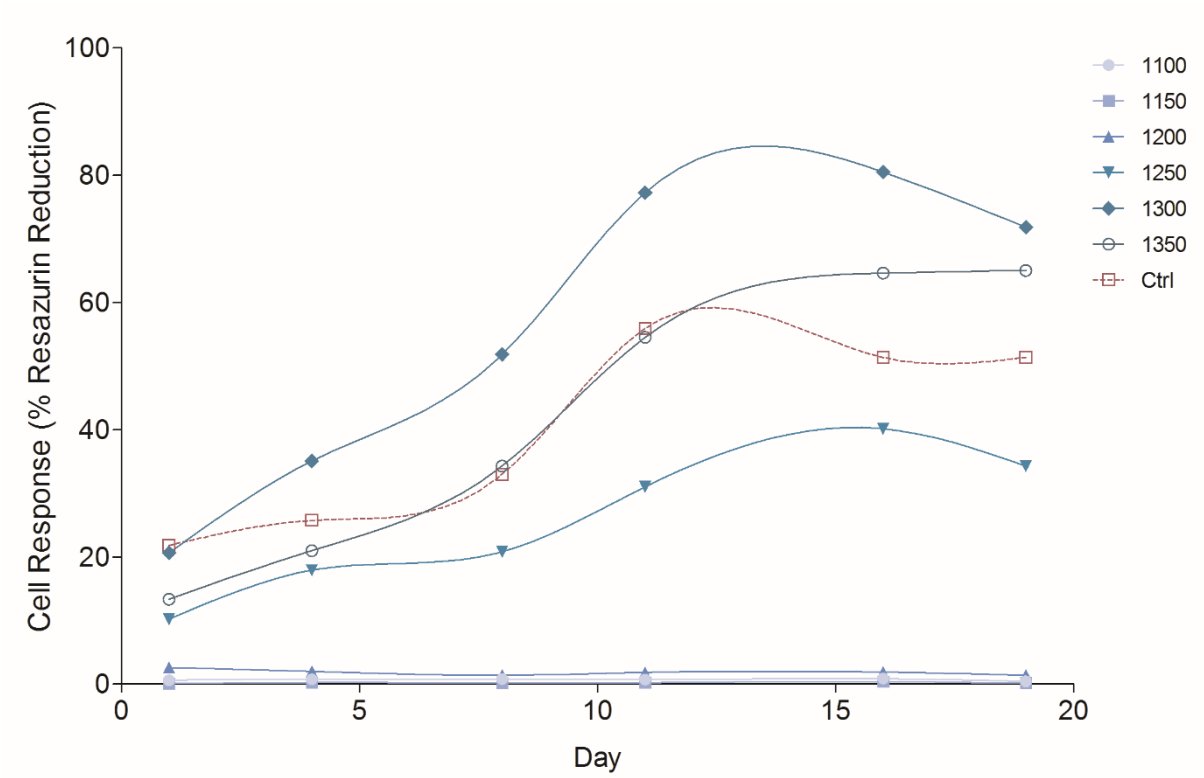

Figure 3.6. *MSC response to HA disks sintered from 1100-1350°C, cultured for 19 days, n = 6. No cell life was observed on the 1100-1200°C surfaces. 1300°C and 1350°C induced the highest cell responses.*

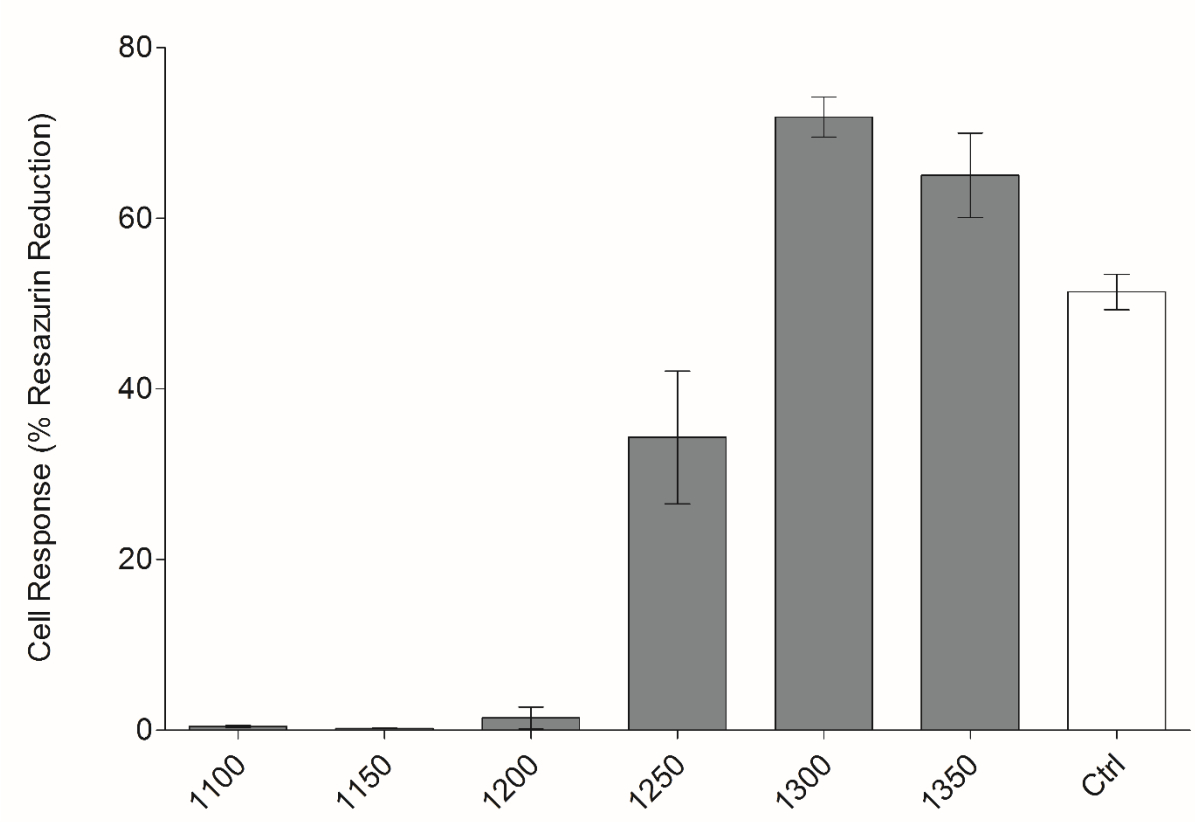

Figure 3.7. *MSC response at day 19 to HA disks. Bars are one standard error from the mean, n = 6. No significant cell life is apparent on the 1100-1200°C surfaces while 1300°C and 1350°C outperform the control.*

As can be inferred from Figures 3.4 and 3.7, the increase in cell response appears to coincide with increasing surface wavelength. A simple regression analysis revealed a strong correlation between surface wavelength and cell response at day four of culture (R^2 = 0.8944) (Figure 3.8). This was in direct contrast to the absence of any trends in the more conventional roughness measurements detailed in Table 3.2.

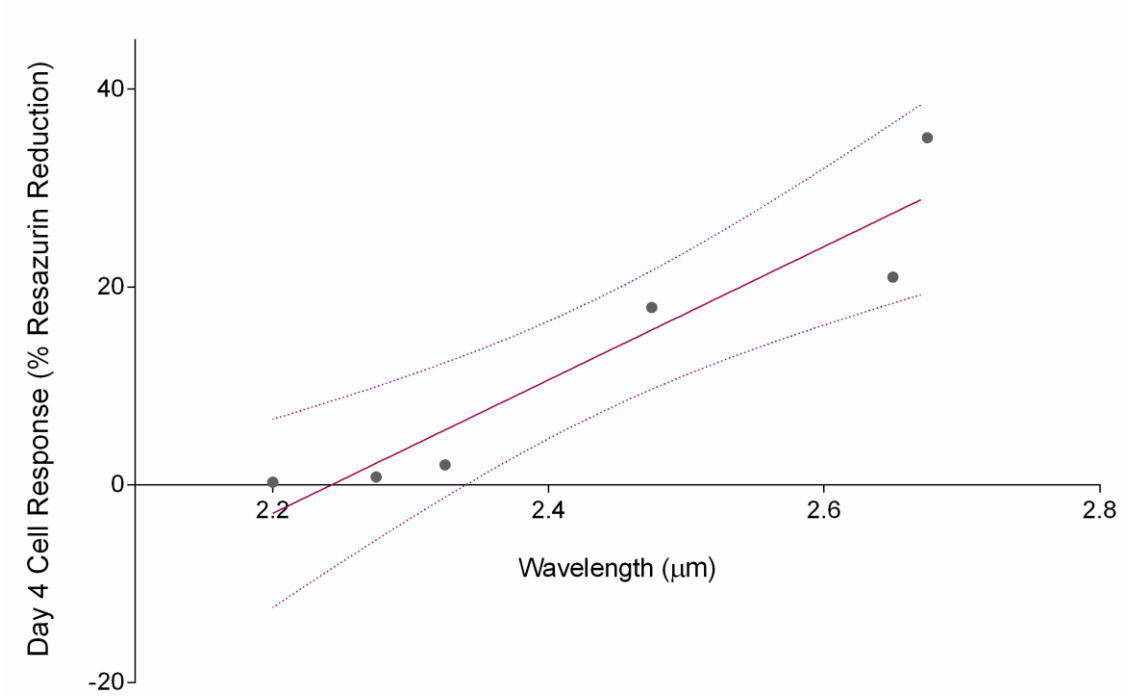

Figure 3.8. *Linear regression of surface wavelength with MSC contact response to the respective HA substrates at day four, $R^2 = 0.8944$. A strong correlation is apparent between surface wavelength and cell response.*

3.3.4.2 Non-Contact MSC Response

MSCs were also cultured in the presence of the various samples but not in direct contact with them (Figure 3.9). This was done in order to help differentiate topographical effects from solution effects; be they ionic diffusion or particulate dissolution. From the ensuing data it is clear that in the first week of culture the difference in sintering temperature had no discernible effect on the cell responses. However, over time the low temperature samples (<1250°C) had an apparent inhibitory effect on cell proliferation. Although the extreme cell death observed on these samples when in contact with the MSCs (Figure 3.6) never became apparent.

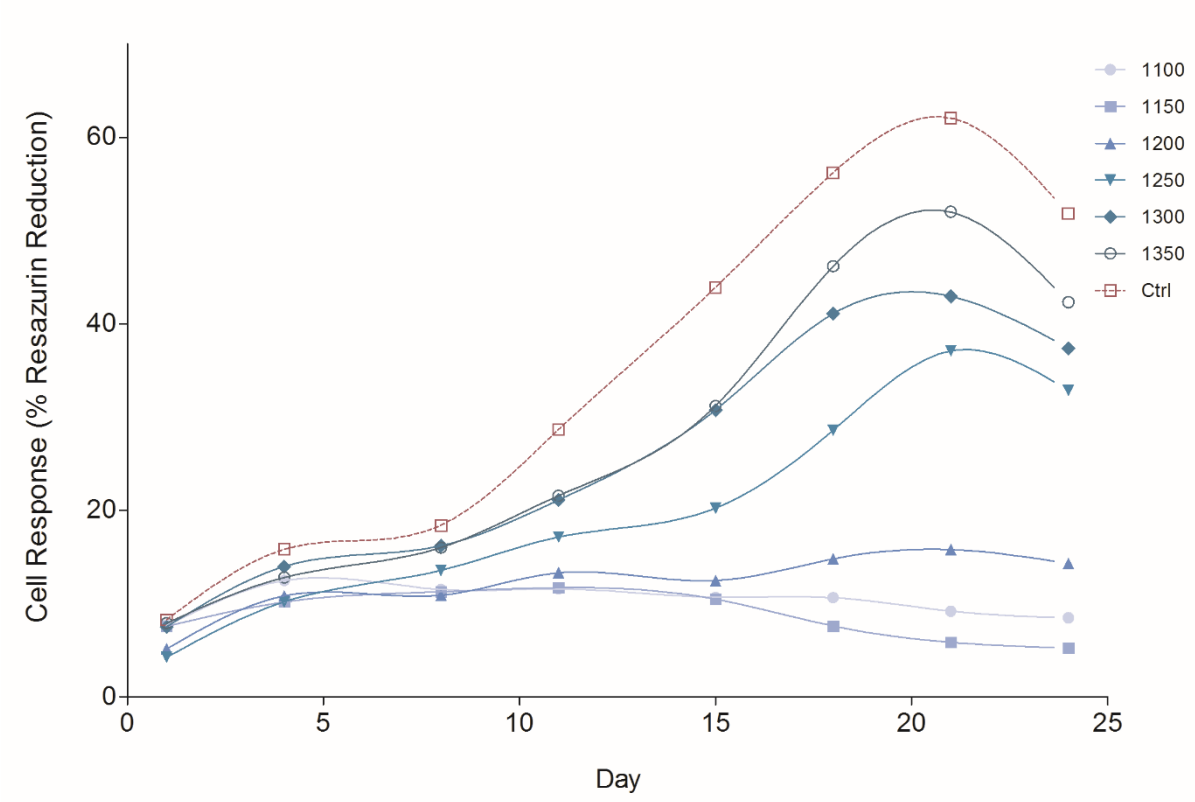

Figure 3.9. *Non-contact MSC response to HA disks sintered from 1100-1350°C, cultured for 24 days, n = 6.*

3.3.4.3 THP-1 Response

Due to the adherence issue experienced by the MSCs in the contact experiment, it was decided to assess the performance of a non-adherent cell line on the same surfaces. Murine bone marrow derived THP-1 macrophages were employed for this purpose.

Differences in cell response were also observable with this cell type (Figure 3.10). Being macrophages and non-adherent meant they could survive and proliferate in suspension and were not dependent on topography for adhesion and subsequent survival. Although cultured for a shorter time period, a similar trend was observable to that displayed by the non-contact MSCs; the materials sintered above 1150°C induced higher cell activity than those sintered at 1150°C and below. Again, an important difference was apparent between the THP-1s and the MSCs

cultured in contact with the HA surfaces; the THP-1s could survive and even proliferate on the low-temperature (<1250°C) samples although in a delayed manner.

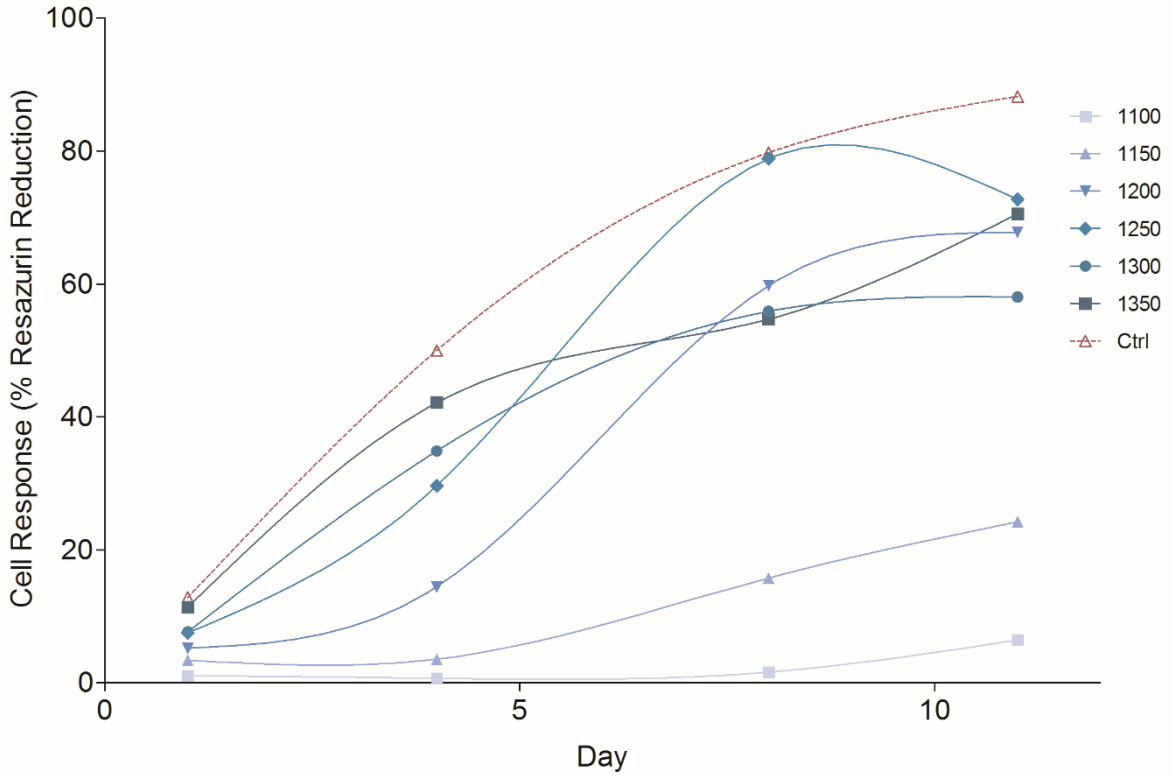

Figure 3.10. *THP-1 response to HA disks sintered from 1100 to 1350°C, cultured for 11 days, n = 3.*

3.4 Discussion

The key outcome from the SEM images of both disks and scaffolds sintered from 1100-1350°C (Figures 3.2 and 3.3) is that they closely match at each temperature point. It was imperative that the disks provided good analogues of the 3D pore surfaces so that useful conclusions could be drawn from the rest of the data. Furthermore, it addresses the criterion of the surface modulation technique being applicable to a porous 3D scaffold.

The morphologies illustrated in Figures 3.2 and 3.3 are so evidently varied that it is surprising they were not easier to differentiate by one of the common surface descriptors e.g. R_a, S_a, S_{dr}, etc (Table 3.2). However, even if they were, it would not solve the more general problem of the huge variation in the literature regarding this matter. It is important that some parameter is chosen as a standard for surface comparison as repeatability will always be difficult otherwise.

When choosing a surface descriptor the first decision to be made is whether one uses a full 3D parameter (i.e. one that incorporates x, y and z axes) or a 2D one (x and z axes) derived from one or more line-profiles drawn across the surface. The limitations of 2D parameters are immediately obvious; they may not be representative of the surface as a whole in that there will a spatial distribution to any peaks as well as the peak deviations themselves. Additionally, information will be lost with the necessary reduction in data. That said, line profiles are easier to generate and analyse and most of the work done to date pertaining to surface description has used profiles. In future, no doubt 3D analysis will be the standard but for now 2D quantifiers are the norm.

Of these, R_a seems to be the most common choice but it is extremely limited as a descriptor of the kind of complex, pseudo-random surfaces often exhibited on tissue engineering scaffolds. R_a is defined as the integral of the absolute value of the roughness profile height over the evaluation length. This method thus cannot distinguish between a surface with many narrow

peaks and one with many narrow valleys. Likewise it gives no indication of the uniformity or otherwise of a surface.

With that in mind, surface wavelength is a good alternative as it contains more information than many of the more common quantifiers. By combining both R_a and Δ, the slope, surface wavelength gives an indication of average amplitude changes contained in the topography and the relative spacing of those changes. This allows for a more complete comparison between different morphologies. The potential success of surface wavelength as a general standard has been indicated here and it acted as an excellent predictor for cell response (Figure 3.8).

It may be argued that the surface wavelength is nothing more than a peak spacing parameter as height information contained in the R_a component is cancelled by the height information provided in the slope. It must be remembered however that the slope is both localised and dimensionless. Thus, the wavelength distinguishes a long, undulating surface, from a sharp, spiky one, provided their features are on the same length scale. Having said that, use of the average surface wavelength as a descriptor should always be supported by SEM data to qualitatively validate the data.

The MSC responses when in contact with the sintered surfaces were interesting. It was assumed that the introduction of nano-sized features into the topography would engender higher cell proliferation rates indicated by higher metabolic responses. However, clearly this was not the case (Figure 3.6). In fact, almost no cell life was observed on the lower temperature surfaces. This indicates that the cells have a more complex relationship with their topographical surroundings than merely sensing how rough or smooth they are. It may be that the cells could not adhere to those surfaces sintered below 1250°C. This hypothesis would seem to be borne out by the fact that there is no cell life evident from the very first timepoint; 24 hours (Figure 3.6). This indicates that the cells died suddenly, not from a gradual cytotoxicity; it is well established that MSCs cannot survive more than a few hours in suspension. In addition, non-adherent THP-1 cells were

shown to proliferate on the lower temperature surfaces (Figure 3.10). This result, coupled with the XRD confirmation of phase stability (Figure 3.5) indicates a lack of evidence for cytotoxicity and supports the adhesion hypothesis.

The biggest discrepancy in cell life occurs between 1200°C and 1250°C (Figures 3.6 and 3.7). These groups have surface wavelengths of 2.325µm and 2.475µm respectively. The difference is so great as to suggest a threshold wavelength, below which cell adhesion is impossible. If it is assumed to be halfway between the two groups then this value would be 2.4µm. Ideally, surfaces would be produced at exact wavelengths along this range and the resulting responses of seeded cells measured in order to determine the exact threshold. However, such accuracy of manufacture would be highly challenging.

The results of the non-contact experiment (Figure 3.9) add an intriguing twist to this story. Over the first week of culture, the various samples have no apparent effect on cell adhesion to the tissue culture plastic and their subsequent proliferation. However, over the next 10 days, the low temperature samples begin to display an apparent inhibitory effect on cell proliferation. This implies that dissolution products from those samples are affecting cell behaviour; these could be ions or particulates smaller than the culture insert mesh size of 8µm. It has been shown that increasing the sintering temperature of calcium phosphate ceramics decreases their dissolution rate [90]. It is difficult to tease out how precisely the dissolution products are inhibiting the cells' proliferation. The XRD evidence of phase stability across the temperature range would suggest that it is a particulate effect that is occurring. If, for some reason, HA becomes more prone to ionic diffusion as its sintering temperature is lowered then it is possible that a significant increase in calcium ions could trigger an apoptotic response in the cells [91]. However, complete cell death is never reached so this would argue against a calcium-apoptosis link. In any event, this result shows that even if the low temperature substrates had surface morphologies that were

favourable for cell adhesion, they would still be inadequate due to their propensity for dissolution.

Finally, as mentioned above, the THP-1 cells do slowly proliferate on the lower temperature surfaces. If apoptotic signals were being generated because of ions diffusing from the disks it would be reasonable to expect the opposite response. One possible reason for the culture profiles shown by the THP-1s here is a particulate effect resulting from decomposition of the low temperature surfaces i.e. debris particles dissociating from the bulk material during incubation. The THP-1s are macrophages and would deal with particulates by phagocytosis (engulfment of the particles). It is possible that during this process the cells either die or produce signals that depress proliferation. In this case, only after most of the particles have been subsumed would the remaining cells begin to proliferate. This might explain the initial poor survival of the cells after seeding but subsequent proliferation (Figure 3.10).

The THP-1 data also covers another potential issue in relation to the MSC response to direct contact with the HA surfaces. THP-1s are not known to be pluripotent (unless specifically induced using chemical factors). Therefore, any changes in their metabolic activity can be attributed to survival and proliferation actions. This fact provides a check on the MSC results and helps support the assertion that the differences in MSC activity are also due to proliferation and not differentiation events.

This chapter has shown the profound effect that a modified topography can have on cellular activity. A relatively small variation in HA sintering temperature can produce surface morphologies that are either conducive to cell life, or completely non-viable. These results indicate that there is potential in this technique to further improve cellular performance on the scaffold surfaces. While an increase in proliferation over the original scaffold was not achieved here, key learnings have been gathered from the various experiments that can be taken forward

through the project. These include the HA phase stability at 1350°C, the non-contact experimental technique and, most particularly, the use of the surface wavelength to predict cell response.

The requirement for a surface to be conducive to cell adhesion, apparently indicated by a long surface wavelength (>2.4µm), leads to an interesting question; is it possible to provide both an adhesive surface and topographical features to stimulate cell proliferation? And, if so, what form would such a surface take? Figure 3.11 attempts to describe such a surface in relation to a cell. It is not to scale and is merely intended as a representation of the concept. In terms of implementing it, an additional phase would be the easiest and most scalable method. A biocompatible material that had a significantly higher sintering temperature than HA would be ideal. This would allow the HA particles to fuse and form the underlying basal layer while the new phase stayed discrete to form the nanoscale features. The next chapter details the efforts to realise such a surface.

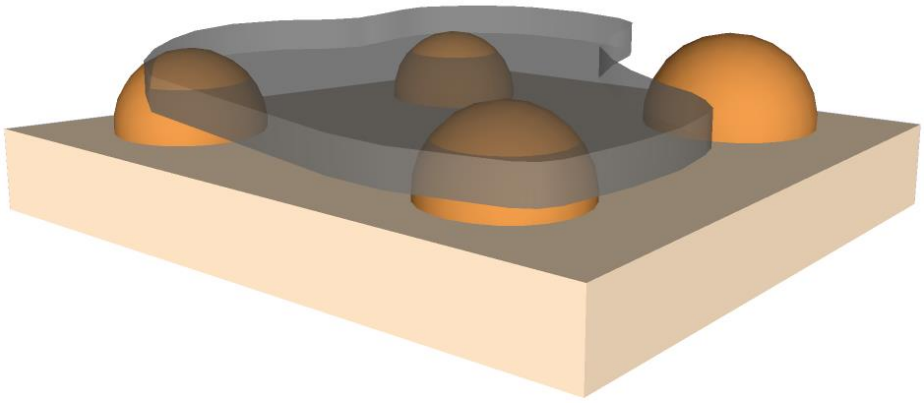

Figure 3.11. *Target surface designed to promote both cell adhesion and proliferation, incorporating a smooth, underlying basal layer and raised nanoscale topographical features. Not to scale.*

3.5 Conclusion

This chapter describes how readily the surface topography of HA scaffolds can be altered using sintering temperature. Contrary to the hypothesis that surface features in the nanoscale range would enhance MSC proliferation on the HA surfaces, cells performed best on the smoothest substrates sintered above 1200°C. It was shown that the surface descriptor that best predicted this phenomenon was surface wavelength; wavelengths above 2.65µm proved optimum for cell adhesion and subsequent proliferation. Furthermore there is an apparent threshold wavelength of ~2.4µm, below which cell adhesion appeared impossible.

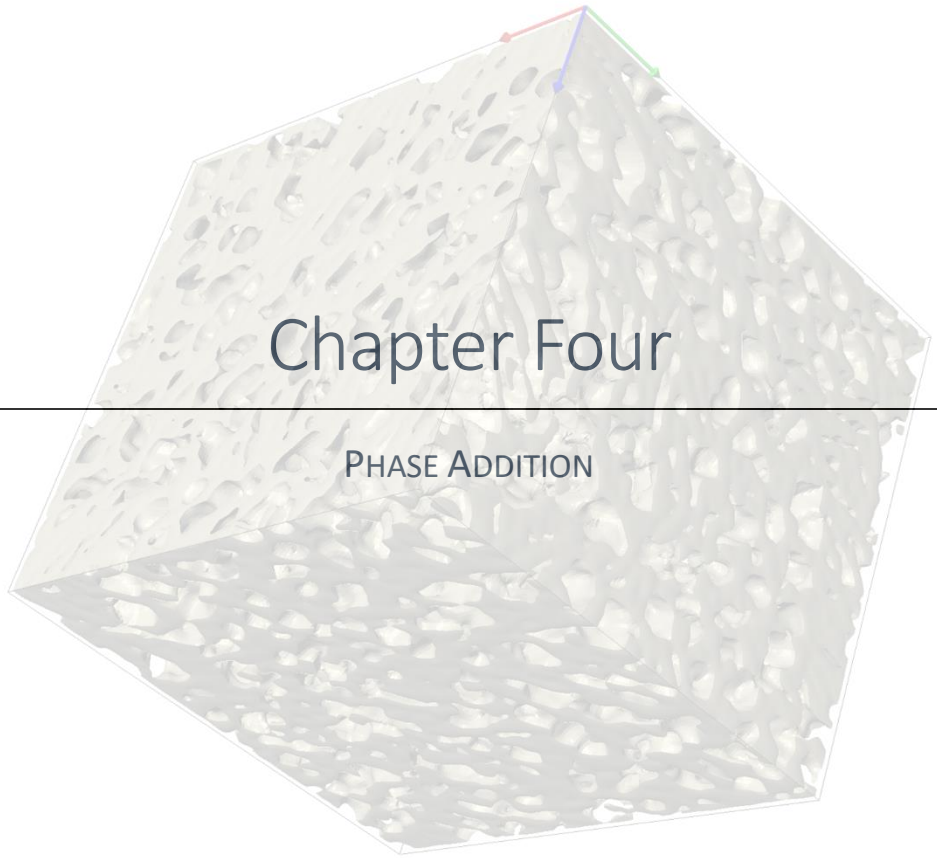

Chapter Four

Phase Addition

4.1 Introduction

Based on the conclusions drawn from Chapter 3, the addition of a second phase to the HA matrix was chosen as a likely method of producing the desired surface topography. This phase needed to be biocompatible and stable at high temperatures; alumina was selected as it fulfils these criteria and is already widely used as a strengthening agent in bone tissue engineering implants [46], [92], [93]. It also has a much higher melting temperature (~2000°C) than hydroxyapatite; so it was expected that the individual particles would remain discrete within the sintered matrix of HA. A nanoscale powder was sourced with a nominal particle size of 135nm. It was intended that these particles would form the nanoscale surface features that would provide the relevant stimulation to the cells to increase proliferation.

The addition of the alumina nanopowder had the desired effect, in small quantities (<10wt%) it induced up to 236% more cell activity than pure HA. However, in concentrations greater than this, it proved detrimental to cell proliferation with quite a sudden change in behaviour between 10wt% and 12wt%. The search for an explanation of this phenomenon forms a large part of this chapter.

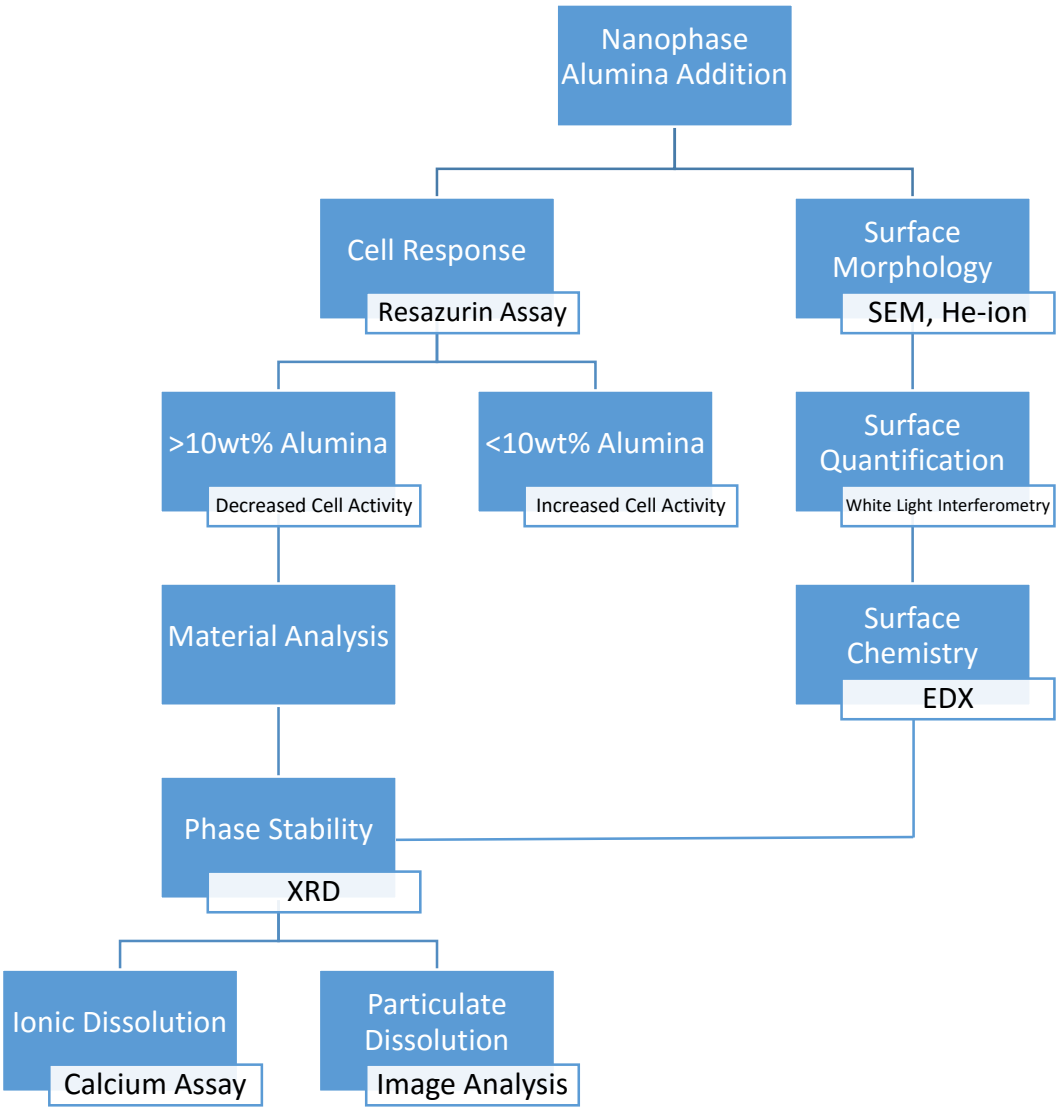

Figure 4.1. *Flowchart describing the methodology and processes of the nanophase alumina addition.*

4.2 Materials and Methods

4.2.1 HA/Alumina Surface Preparation

Precursor powders were prepared by adding alumina nanopowder (US Research Nanomaterials Inc., Houston, TX, USA) with nominal particle size of 135nm to hydroxyapatite (puriss, ≥90%, Sigma-Aldrich) and ball milling overnight at 23rpm in a Turbula mixer. Concentrations of between 2% and 14wt% alumina were examined.

As in Chapter 3, the scaffold pore surfaces were represented by 2D disks. These were made by lightly pressing 200mg of precursor powder and sintering under the same conditions as those described before.

With such small quantities involved in the ball-milled samples, it was felt that there was a possibility of much of the alumina being lost in the bulk of the disk. In order to maximise the amount of alumina present at the surface, an additional substrate was produced by dropping a suspension of alumina nanoparticles onto pre-sintered HA disks. Pure HA disks were sintered to 1350°C in order to close as much of the bulk porosity as possible and ensure the majority of the alumina nanoparticles remained on the surface. A 100mg/ml suspension of nanopowder in isopropanol (Vishay Measurements Group, Basingstoke, UK) was mixed overnight on a rotator table at 50rpm. The suspension included the dispersant Darvan 811 (RT Vanderbilt Company Inc., Norwalk, CT, USA) at a concentration of 2wt% to 100% alumina. 100µl of this suspension was then dropped onto the pure HA disks. These samples then underwent another sintering cycle to 1350°C.

4.2.2 Repeated Analysis

SEM, He-ion, XRD and white light interferometry were all employed to characterise the surfaces as before in Chapter 3. In addition, the same mesenchymal stem cell culture techniques

were used; both in contact with the surfaces and in a non-contact experimental set-up. Cell response was measured by the resazurin media assay.

4.2.3 EDX Analysis

Energy-dispersive X-ray spectroscopy (EDX) was used to characterise the chemistry at the surface of the HA/alumina samples. The EDX apparatus was mounted to the same Zeiss Ultra machine used for SEM imaging and data was analysed using Oxford Instruments INCA system (Oxford Instruments, High Wycombe, UK).

4.2.4 Calcium Assay

Results from the cell culture experiments showed a change in response from the MSCs across the 10-12wt% alumina threshold. Furthermore, XRD revealed phase changes occurring in the HA with increasing alumina content. It was hypothesised that the adverse reaction of the cells to concentrations of alumina >10wt% could be due to excess calcium ions diffusing into the media from the decomposing HA. Excess calcium has been linked with cellular apoptosis [91].

In order to determine whether various HA + alumina combinations produced different amounts of calcium ions in solution, a standard calcium assay was performed on media containing pure HA, HA+6wt% alumina and HA+14wt% alumina disks.

Disks were individually weighed and then incubated at 37°C for one week in cell culture media. After removal from the incubator, supernatant media from each sample and from blank control wells was diluted by 50% using 1M HCl. Groups were then analysed using a Sentinel Calcium Kit, (Sentinel Diagnostics, Milan, Italy).

The kit consists of a calcium standard and two reagents; reagent one: 2-aminoethanol buffer 1.0 mol/L pH > 10.0 and reagent two: hydrochloric acid 0.12 mol/L pH < 2.5, cresophthalein complexone 0.3mmol/L, 8-hydroxy-quinoline > 10mmol/L. These reagents were mixed in a ratio of 5:2 to form the working solution. Samples were compared against a standard curve of seven dilutions of the calcium standard from 0 – 800ng/well. 10µl of each standard and sample were placed in a clear, round-bottomed microplate and 140µl of working solution added to each. The plate was covered and allowed to incubate for 10 minutes at room temperature before reading in a Synergy HT plate reader (BioTek, Winooski, VT, USA) at 570nm absorbance.

4.2.5 Disk Debris Analysis

During the manufacturing process it was noted that samples with higher alumina contents (approximately >10wt%) appeared to be structurally less stable and more prone to formation of particulate debris. Again, this was viewed in conjunction with the fact that cells responded negatively to alumina concentrations in excess of 10wt%. Microscale particles have been shown to have an adverse effect on cellular proliferation [94] and this was believed to offer an explanation for the poor proliferation seen on those substrates with >10wt% alumina contents.

In order to verify and quantify any particulate dissolution from the samples, pure HA, HA+6wt% alumina and HA+14wt% alumina disks were incubated in cell culture media for one week. These alumina concentrations were chosen as they occur on either side of the apparent threshold for positive cell response, ~10wt%. Samples were imaged using an Olympus BX 41 microscope system (Olympus, Tokyo, Japan) and QCapture-Pro software (QImaging, Surrey, BC, Canada). The resulting images were then examined for debris using the “Analyse Particles” function of ImageJ [95].

This function works by scanning a thresholded, binary version of the image until it detects the edge of a particle. It then outlines and measures the particle, fills it in to make it invisible and repeats the process until no more particles remain. A table of descriptive statistics is produced detailing, amongst other things, the number, size, shape and position of the various particles.

4.2.6 Statistical Analysis

The significant success of the low alumina concentrations coupled with the sudden, unexpected decrease in performance at >10wt% alumina led to the contact cell culture experiments being performed independently in triplicate. All other studies were verified through duplication. In general, it was not possible to pool the data from the experiments due to varying culture conditions and manufacturing batches. Hence, the data presented were taken from single experiments and the conclusions verified across the repeated tests. A high sample number, n, of six was used in each study unless otherwise stated to increase the power of the individual trials.

Groups were evaluated using one-way analysis of variance (ANOVA) and Tukey's comparison test. Results with a $p \leq 0.05$ were considered significant. All analysis was performed in Minitab (Minitab Ltd., Coventry, UK). Graphs were produced in GraphPad Prism 5 (GraphPad Software Inc., La Jolla, CA, USA).

4.3 Results

4.3.1 Surface Morphology

He-ion microscopy (Figure 4.2) provided evidence that, when ball-milled together overnight, the alumina nanoparticles combined with the HA matrix to provide the idealised surface suggested in Chapter 3. The HA formed a smooth, underlying basal layer while the alumina nanoparticles were embedded into the HA matrix forming features of approximately 200-500nm in diameter. These are larger than might be expected from a nanopowder with a reported nominal particle size of 135nm. However, when allowances are made for particle size distribution and manufacturing induced aggregation, 200-500nm is an acceptable final feature size.

Figure 4.2 also highlights the difference in topography on a pure HA surface (A) and that achieved by adding alumina nanoparticles to the HA at a concentration of 5wt% (B and C). These images indicate the significant increase in surface features produced by the alumina compared to the smooth, undistinguished surface of the pure HA disk.

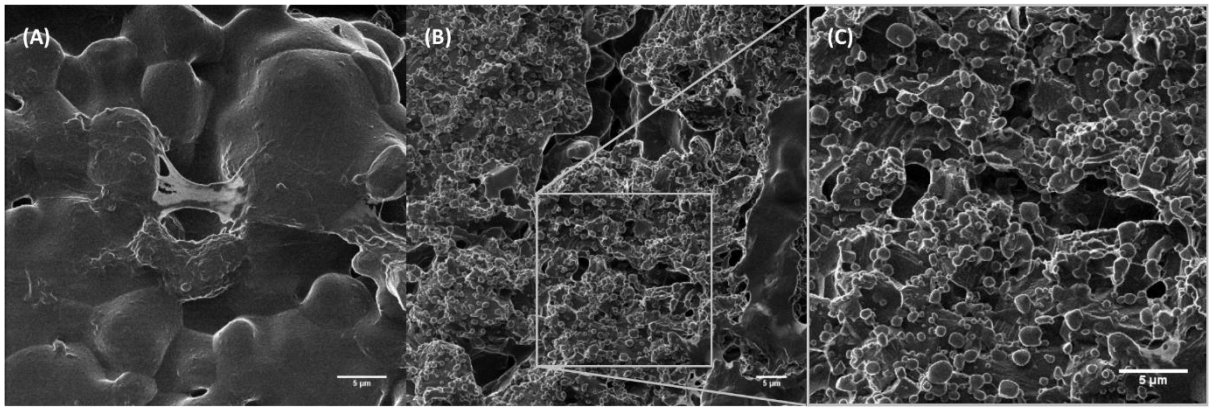

Figure 4.2. *He-ion images of the surfaces of (A) pure HA, (B and C) HA+5wt% alumina disks. Scale bars are 5um. Note the increase in topographical features apparent in the alumina samples.*

There were also notable variations in morphology between the ball-milled HA/alumina samples and the samples where alumina was deposited in suspension (Figure 4.3). On the deposition surfaces, the alumina appeared to have aggregated into large areas in contrast to the

even distribution of topographical features evident on the ball-milled surface. In addition, some sintering of the alumina nanoparticles was apparent on the deposition surfaces. The combined effect of these phenomena was a loss in fidelity of the features provided by the alumina, resulting in a less distinct morphology. On this basis, it was determined that the ball-milled surface provided the best analogue of the ideal topography proposed in Chapter 3.

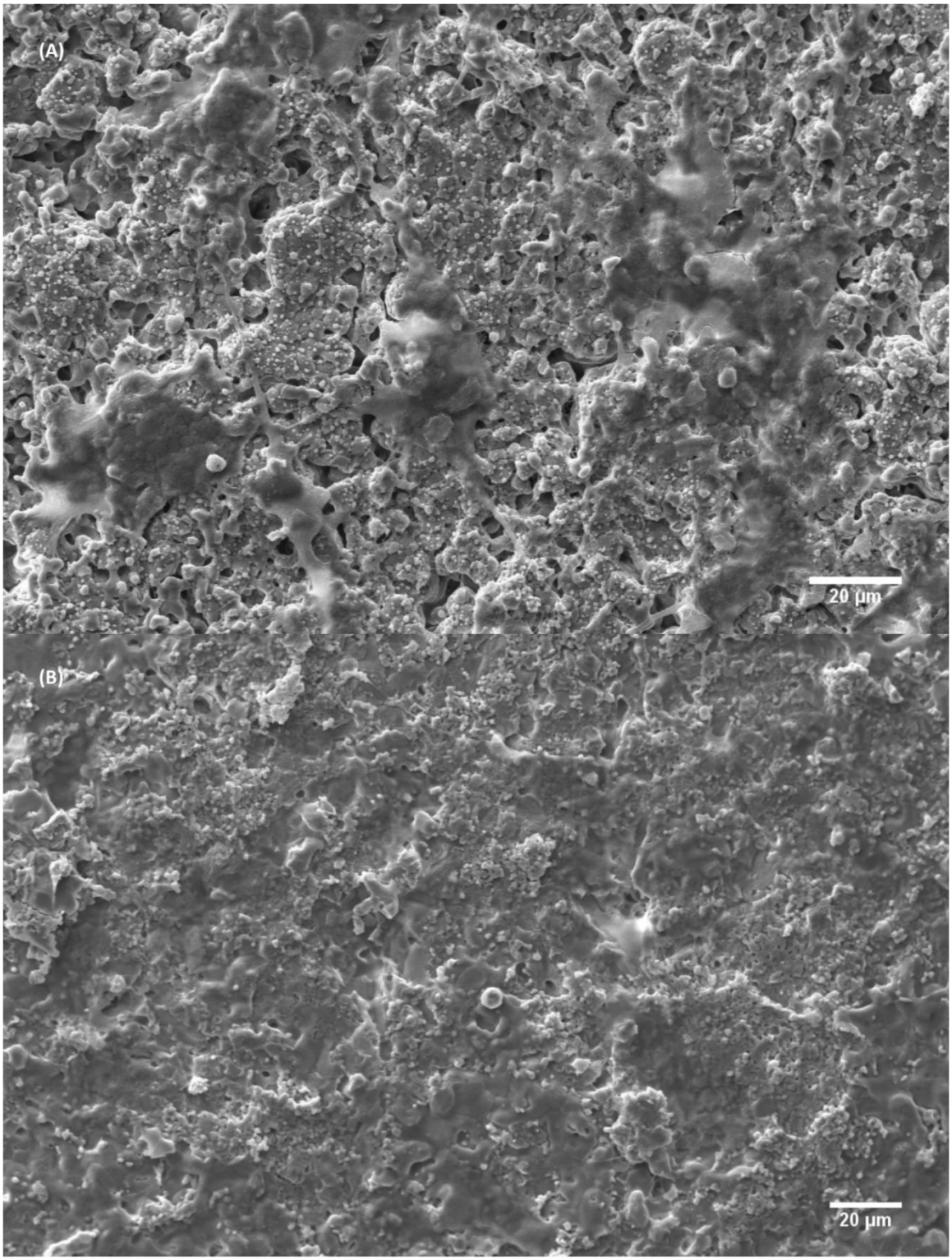

Figure 4.3. *SEM images of (A) Ball-milled HA+5wt% alumina and (B) Alumina suspension deposited on HA surface. Scale bars are 20µm.*

4.3.2 Surface Quantification

One of the key conclusions drawn from the sintering temperature experiments in Chapter 3 was that there was a threshold surface wavelength (~2.4µm) below which cell adhesion and subsequent survival were greatly compromised. Hence, it was imperative that when the alumina was included into the HA matrix it did not alter this parameter. Ideally, the new surfaces would be comparable to the optimum value established by the same experiments (~2.65µm) (Chapter 3). In order to assess the surface wavelengths of the Ha/alumina substrates, white light interferometry was again employed.

Figure 4.4 shows the surface wavelengths of pure HA and HA+2-14% alumina sintered at 1350°C. All of the surfaces displayed wavelengths above the required value of 2.4µm. Furthermore, there was no significant difference between any of the groups. Thus it is reasonable to expect that the new HA/alumina surfaces will at least be as conducive to initial MSC adhesion as the pure HA. Particularly the 2 and 6% alumina samples which were well above the 2.65µm optimum surface wavelength.

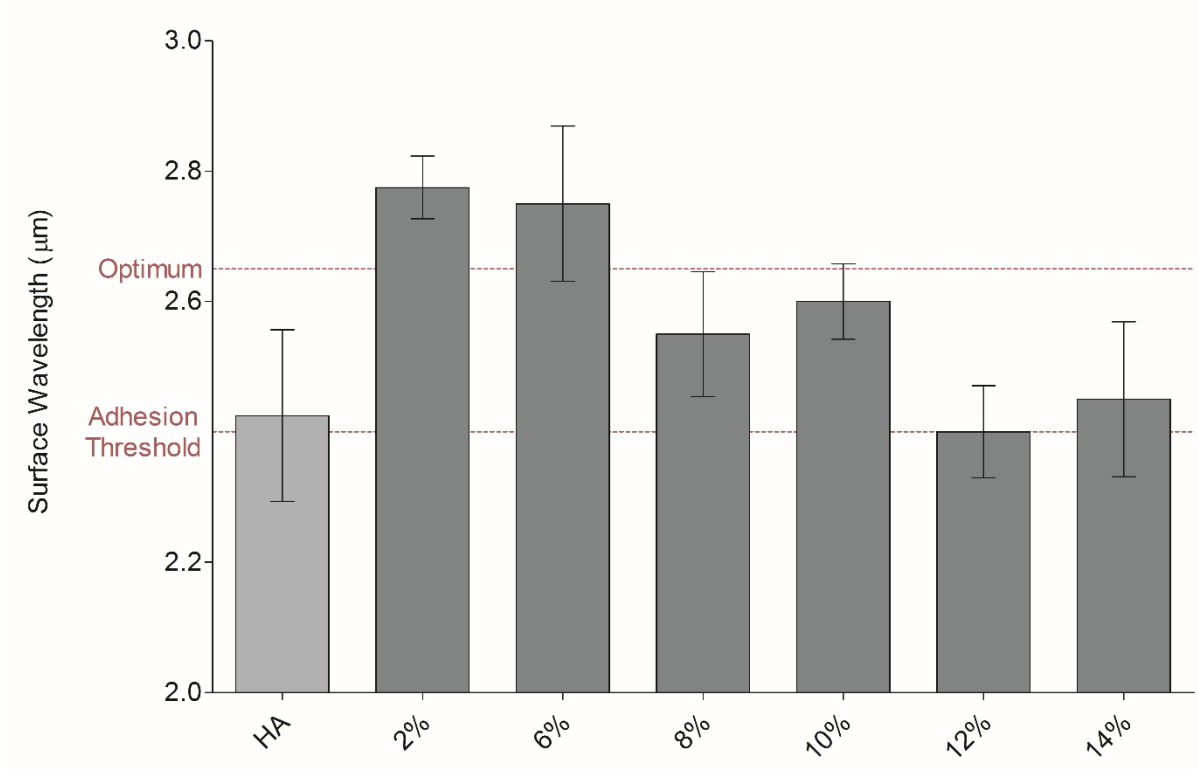

Figure 4.4. *Surface wavelengths of pure HA and HA+2-14wt% alumina. Error bars represent one standard error of the mean.*

4.3.3 EDX Analysis

In order to confirm that the nanoscale features observed in the He-ion images were formed from the alumina as hypothesised, EDX analysis was carried out on the surface of a HA+10wt% alumina sample (Figure 4.5).

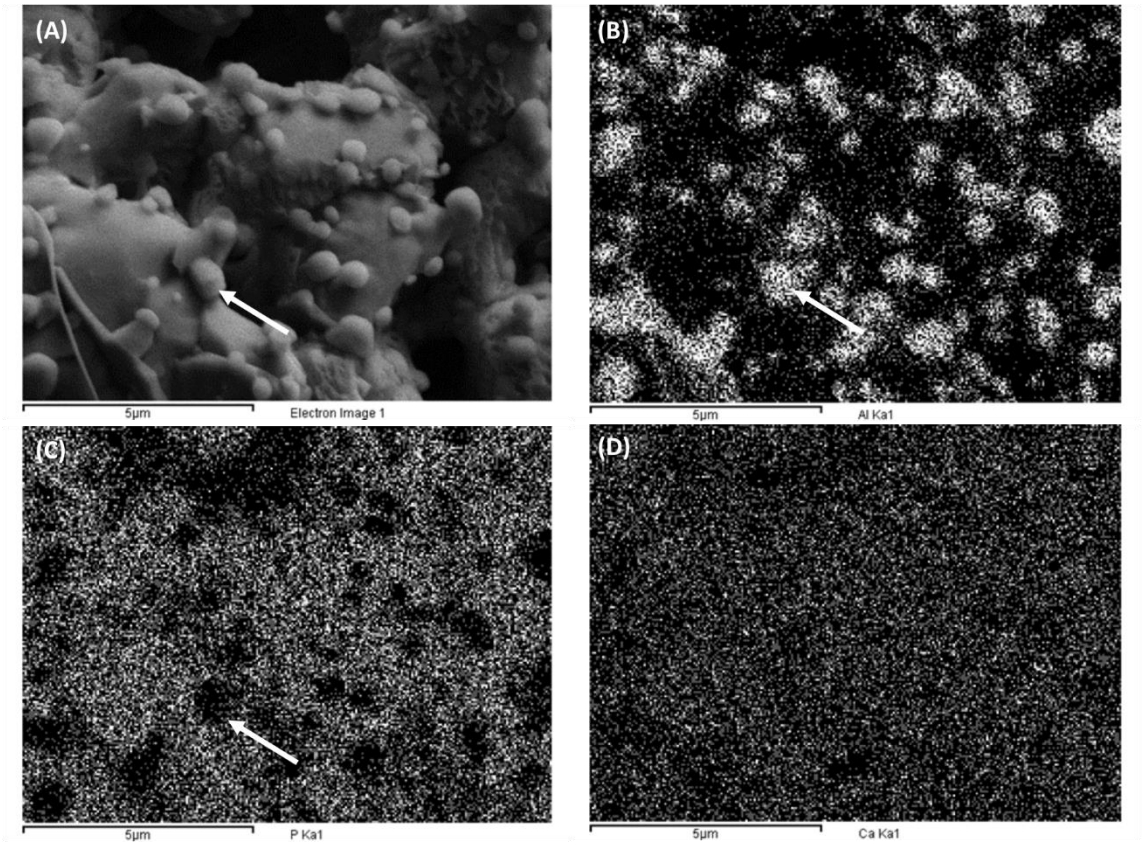

Figure 4.5. *EDX analysis images. (A) Raw SEM image. (B) EDX map for aluminium. (C) EDX map for phosphorus. (D) EDX map for calcium. Scale bars are 5µm. One nanoparticle has been tracked and indicated by white arrows.*

EDX is an elemental analysis and, as such, cannot yield information on the combinatorial nature of the elements it detects. However, the data is still useful as it shows the extent to which ionic diffusion may or may not have taken place between phases in a sample. These data show that the locations of high concentrations of aluminium (Figure 4.5(B)) correspond to the positions of the nanoscale features shown in the SEM image (Figure 4.5(A)). This demonstrates that the alumina particles have had the desired effect and created nanoscale topographical features in the HA matrix.

It is also interesting to note that the alumina particles are highlighted by negative spaces in the EDX map of phosphorus (Figure 4.5(C)) but not in the map of calcium (Figure 4.5(D)). This shows that the phosphate groups of the HA have remained *in situ*. Conversely, some of the

calcium has diffused into the alumina particles, hinting at a potential reaction between the alumina and the calcium ions.

4.3.4 XRD Analysis

X-Ray diffraction was employed to assess the phase stability of the HA/alumina composites after sintering. The EDX data gave this analysis even greater importance as the apparent diffusion of calcium ions implies a phase change is occurring.

Repeated XRD analyses revealed a certain amount of batch variability in the HA/alumina samples. The variability was small and was attributed to the relatively small quantities of powders being mixed to form the precursors. The key finding from the XRD analysis was that as alumina content increased in the samples, the HA progressively decomposed to α-tricalcium phosphate (α-TCP) (Figure 4.6). At low concentrations (1-2wt%) of alumina, the HA remained relatively pure with only very faint peaks indicating the presence of the α-TCP phase. With increasing alumina content however, the ratio of HA to α-TCP steadily increased to a point where the only major detectable phase was α-TCP. The exact concentration of alumina at which pure α-TCP occurred was difficult to establish due to the batch variability however it appeared to occur between 8-10wt% alumina.

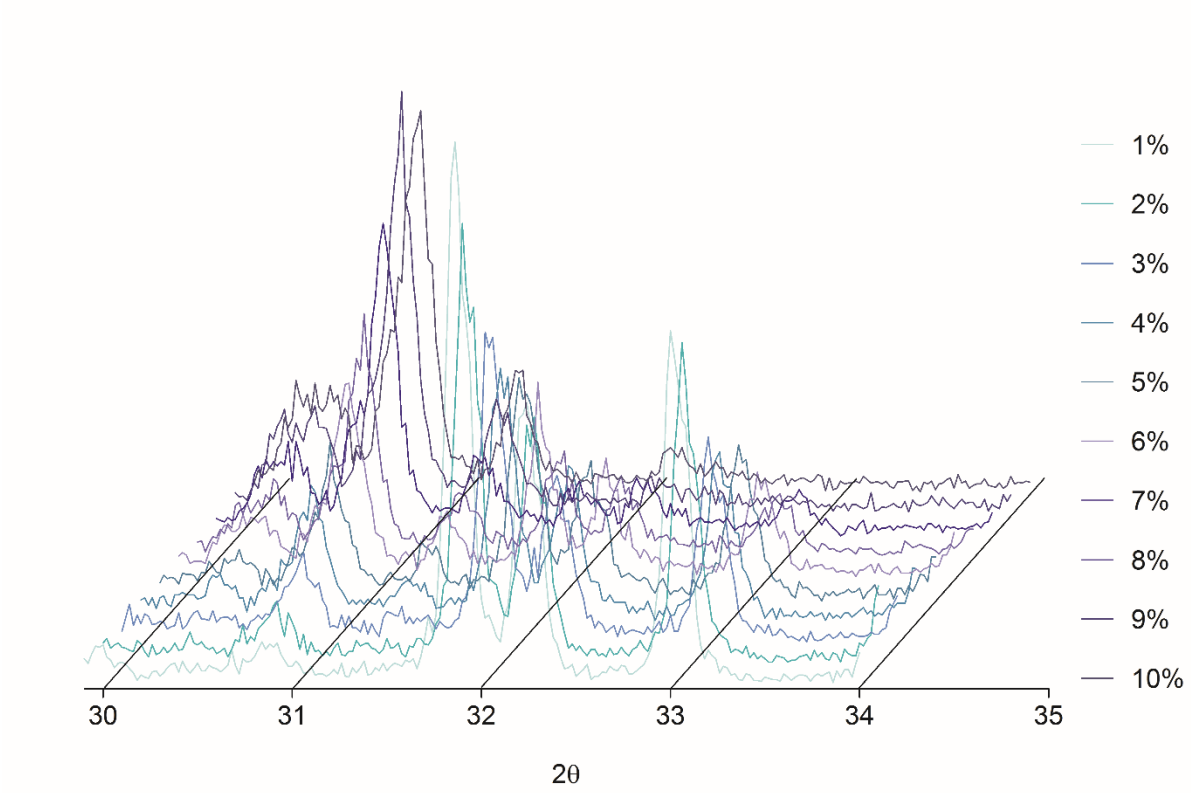

Figure 4.6. *XRD patterns for HA + 1-10wt% alumina. For clarity only data from 29.9-34° is shown. The peaks at 30.2°, 30.8° and 31.3° correspond to α-TCP. The peaks at 31.9°, 32.2° and 30.0° correspond to HA.*

It is also interesting to note that there was no evidence in the XRD data of the alumina phase. It is possible that it was present in too small a quantity to be apparent amongst the stronger calcium phosphate peaks. However, coupled with the EDX analysis it increases the evidence of a reaction taking place between calcium ions diffusing from the HA matrix and the alumina nanoparticles. Conceivably this reaction could result in a new phase not identifiable from the XRD data e.g. calcium aluminate.

4.3.5 Cell Response

4.3.5.1 Cell Response to Ball-Milled Substrates vs. Deposition Substrates

A preliminary cell culture experiment was performed to determine if either the ball-milling or direct deposition methods of adding the alumina produced better responses in the

MSCs. The cells were cultured for 10 days and proliferation was measured by resazurin assay. The resulting data show that the balled-milled HA+5wt% alumina samples tend to induce significantly higher MSC proliferation rates than the deposition samples (Figure 4.7). The superior performance of the ball-milled surfaces in this experiment, coupled with the greater simplicity of the ball-milling procedure, led to this method being selected as the protocol of choice for phase addition. All subsequent analysis was done on ball-milled HA+alumina samples.

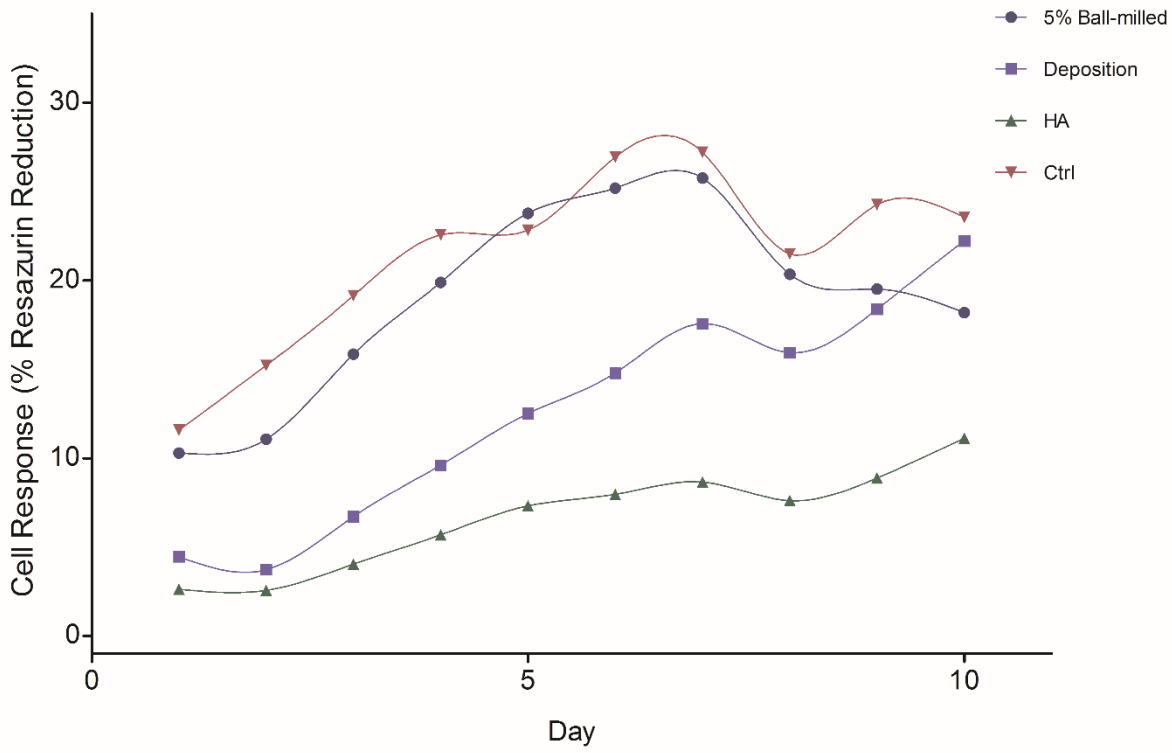

Figure 4.7. *Cell response to ball-milled HA+5% alumina, HA + alumina deposition, pure HA and tissue culture plastic control. Culture period was 10 days.*

4.3.5.2 Contact MSC Response

After determining the best method for adding the alumina into the surfaces, it was required to assess what concentration of alumina produced topographical features that induced the best cell proliferation. Cells cultured in contact with surfaces comprised of HA+2-10wt%

alumina showed significantly higher proliferation profiles than those cultured on both pure HA and the tissue culture plastic control (Figure 4.8). This manifested itself as an acceleration in proliferation across the first 15 days of culture. Overall, HA+2% alumina was the best performer although at no stage was there a significant difference between the 1-10wt% samples. At day 15, HA+2wt% alumina exhibited 185% of the cell activity of pure HA and 430% of the activity on the control. Thereafter, the high rate of proliferation was maintained across the HA+1-10wt% alumina samples whereas both pure HA and control experienced a plateau effect. The highest cell activity occurred at the end of the culture period, day 32. By then the best performer, HA+8wt% alumina, was generating 261.5% of the activity of pure HA and 447% of the control. This represents a remarkable increase on the proliferative capacity of the surfaces caused by the addition of the alumina.

Strikingly, the beneficial effects on cell response apparent from the HA+1-10wt% samples were completely absent in the HA+12wt% and HA+14wt% alumina groups. In Chapter 3 complete cell death was observed on HA surfaces sintered below 1250°C. However here, even on the lowest performing samples, there remained some cell activity. Thus, the problem is unlikely to be a lack of cell adhesion as was hypothesised for the low-temperature substrates. Even so, on the high alumina samples the cellular activity and thus proliferation were greatly compromised with a general downward trend across the culture period.

	% Resazurin Reduction	% of Control	% of HA
Control	17.035	100	58.5
HA	29.129	171	100
2%	68.643	403	236
8%	76.182	**447**	**261.5**
14%	4.172	24.5	14

Table 4.1. *Abbreviated results from Day 32 of the contact cell culture period. The performance of HA+8wt% alumina is highlighted.*

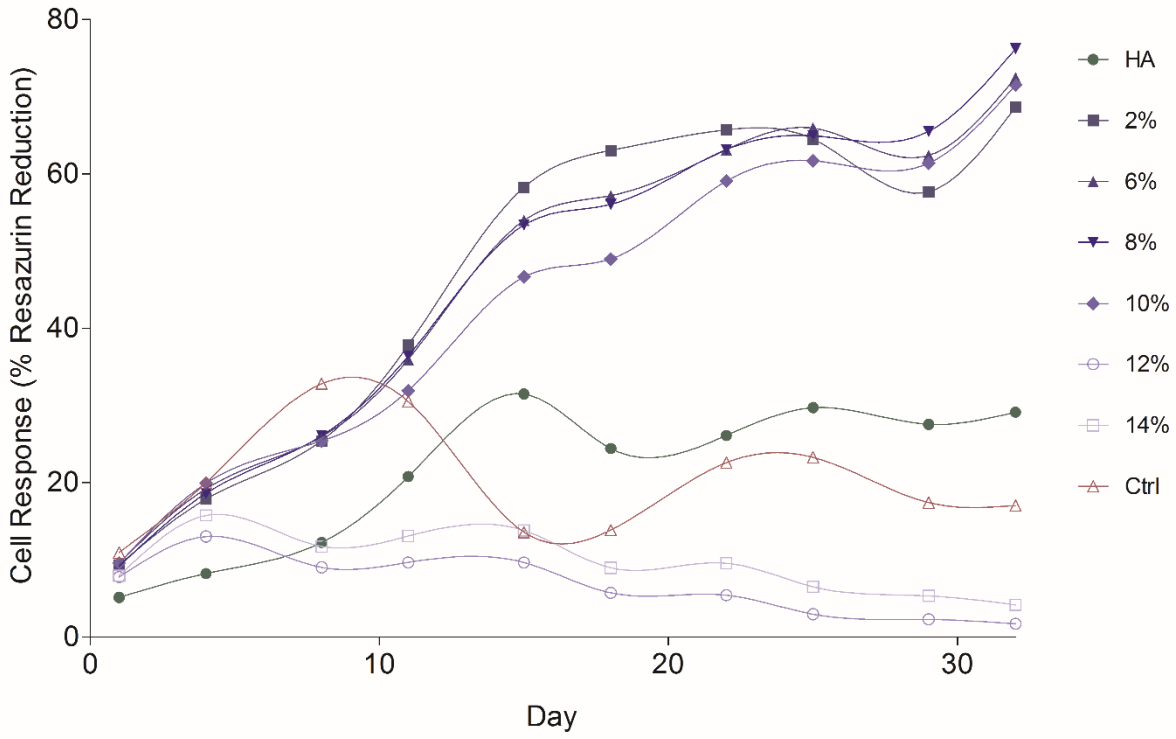

Figure 4.8. *MSC response to contact with pure HA, HA+2-14wt% alumina and tissue culture plastic control surfaces across 32 days of culture, n = 6. Error bars have been omitted for clarity.*

To give a more statistical representation of the data presented in Figure 4.8, the last three days of culture have been graphed separately and error bars representing standard error of the mean included (Figure 4.9). This graph highlights the three distinct levels of cell response to the various surfaces; low activity on the 12wt% and 14wt% substrates, relatively moderate activity on the pure HA and control surfaces and the much higher activity on the 1-10wt% samples. In addition it is interesting to note that the 1-10wt% groups are tightly bunched with overlapping error bars indicating the lack of significant difference between them.

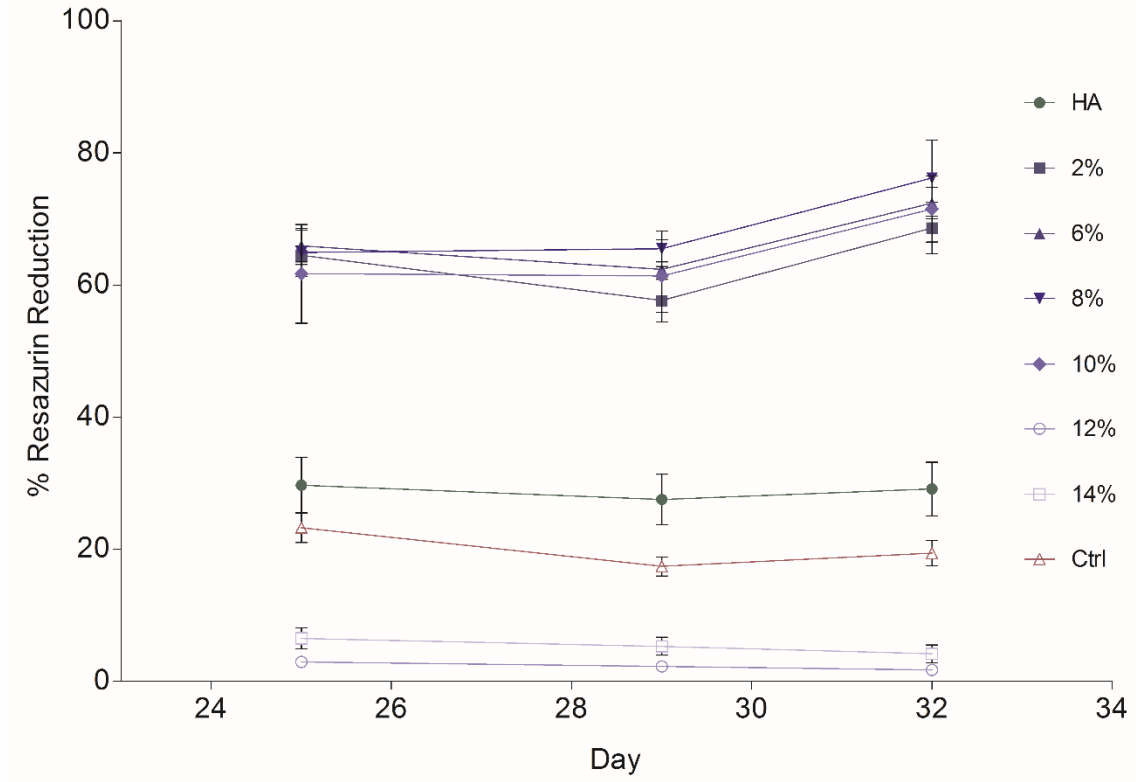

Figure 4.9. *MSC response to contact with pure HA, HA+2-14wt% alumina and tissue culture plastic control surfaces across day 25-32 of culture, n = 6. Error bars represent standard error of the mean.*

4.3.5.3 Non-Contact MSC Response

To separate topographical effects from dissolution effects, MSCs were again cultured in the presence of HA+2-14wt% alumina substrates but not in direct contact with them (Figure 4.10).

Cells were seeded onto the bottom of 24-well plates. The HA+alumina disks were then introduced, separated from the cells by polycarbonate mesh cell-culture inserts.

There was little separating the different groups in this case, although the 12% and 14% samples appeared to slightly depress proliferation again. Most importantly, the highly positive effect of the HA+1-10wt% alumina surfaces on cell response (Figure 4.8) was lost with pure HA now the highest performer. This indicates that the beneficial effect seen on these groups previously was due primarily to the novel nanoscale topography provided by those substrates and that cells must be in contact with the surfaces to benefit from it.

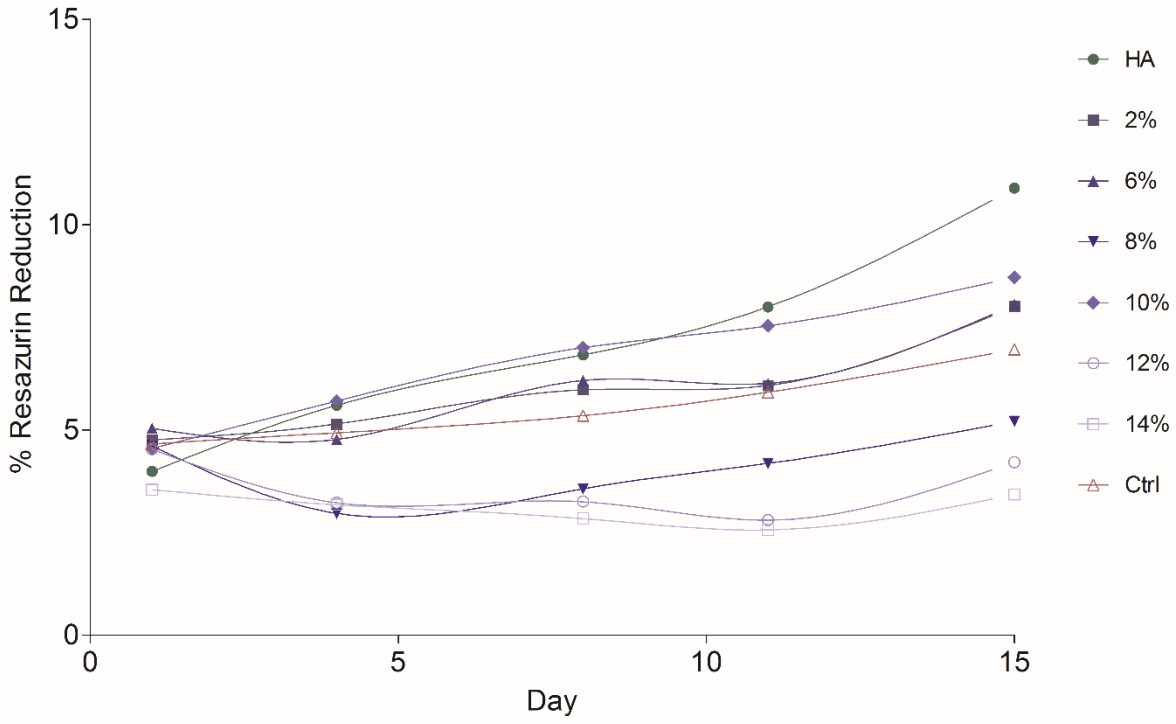

Figure 4.10. *Non-contact MSC response to pure HA and HA+2-14wt% alumina surfaces across 15 days of culture, n = 6. There were no significant differences between samples.*

Although there was no significant difference between groups in the non-contact MSC experiment, the general trend of the 12 and 14wt% alumina groups was still lower than the other groups. This appeared to mirror the results of the contact experiment. It was thought that this could point to a difference in dissolution behaviour between the samples; either ionic or

particulate. To investigate this, experiments were designed to test whether potential dissolution products were having a detrimental effect on cell proliferation on the high alumina samples.

4.3.6 Calcium Assay

Excess calcium has been suggested as having a apoptotic effect on cells [91]. With this in mind, a calcium assay was employed to determine whether there was any difference in the amount of calcium ions diffusing from the bulk of samples both above and below the 10wt% threshold. Pure HA, HA+6wt% alumina and HA+14wt% alumina disks were incubated for seven days in acellular media. Calcium concentrations in the supernatants were then determined by assay and compared to blank media controls (Figure 4.11).

Results are shown as both nanograms of calcium per well (Figure 4.11(A)) and nanograms of calcium released per milligram of original sample (Figure 4.11(B)). This was to account for any disk-to-disk variation and normalise the results by weight. In the first instance none of the groups are significantly different from the cell culture media control (Figure 4.11(A)). This indicates that none of the disks are releasing significantly more calcium ions into the supernatant than would already be found in the media. When the results are normalised by weight (Figure 4.11(B)) there is no significant difference in calcium released by pure HA and HA+14wt% alumina. Hence, the difference in cell response to these two formulations cannot be attributed to excess calcium dissolution.

Combined with the XRD and EDX analysis, the lack of free calcium ions in the supernatant means that they must remain bound in the bulk material. Diffusion of calcium from the hydroxyapatite into the alumina has already been shown. Hence, a reaction resulting in calcium aluminate at that point now looks more likely.

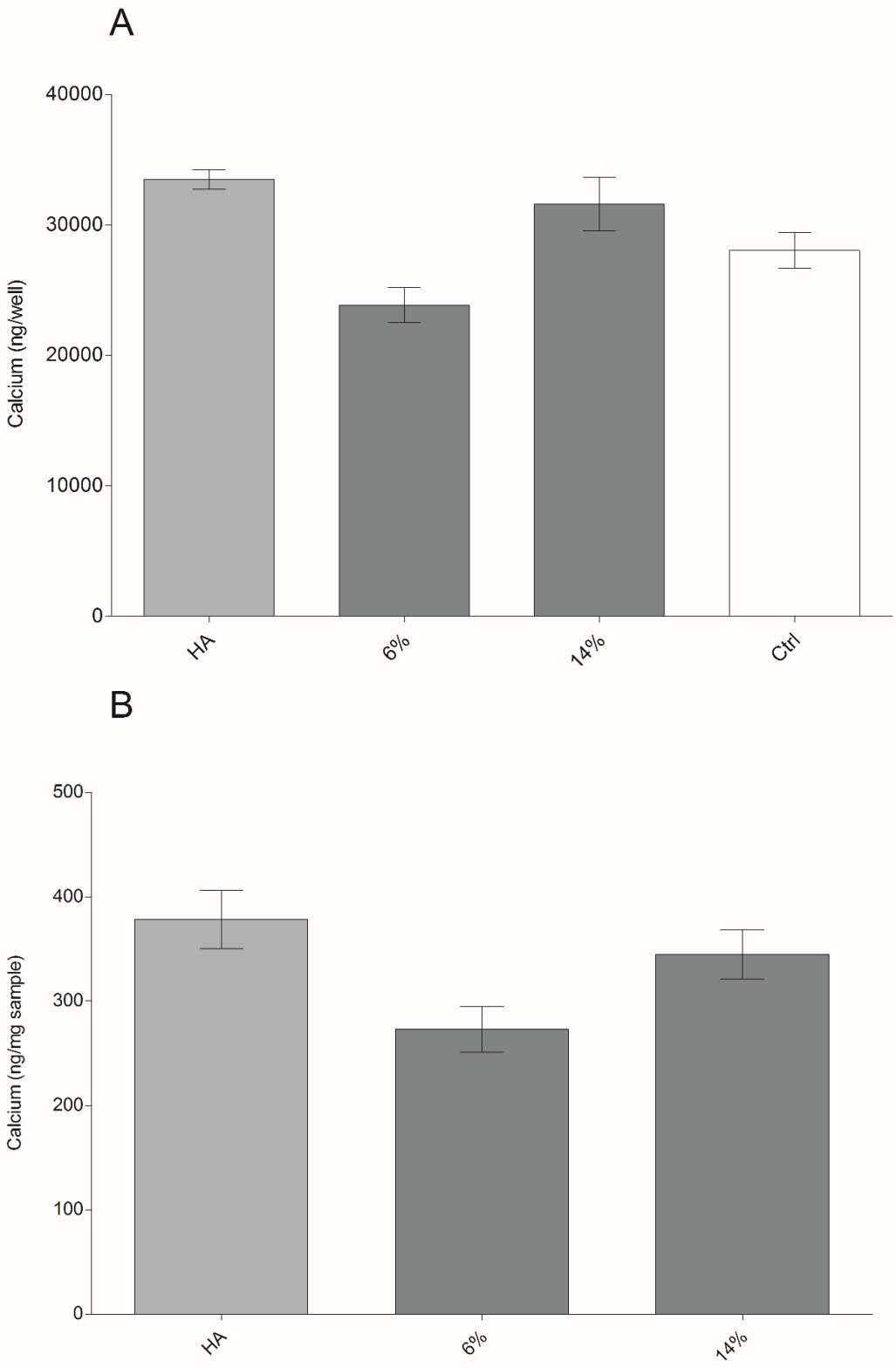

Figure 4.11. *Calcium released by pure HA, HA + 6wt% alumina and HA + 14wt% alumina expressed as (A) nanograms per well and (B) nanograms per milligram of sample. Error bars represent one standard error of the mean.*

4.3.7 Disk Debris Analysis

Another potential explanation for the poor cell response to substrates with high alumina content is particulate debris released from the samples during incubation. Such debris has been shown to adversely affect cell proliferation and viability [94]. It was noted during the manufacturing phase that higher alumina content samples appeared more prone to particulate dissociation. This experiment was an attempt to both verify and quantify that dissociation using microscopy and subsequent image analysis. Again, HA+6wt% and HA+14wt% alumina surfaces were chosen to examine as they are below and above the cell viability threshold (10wt%) respectively. Comparisons were drawn with respect to pure HA.

Examples of the images used to perform the analysis are shown in Figure 4.12. It is immediately apparent that the pure HA disks produced the least amount of debris (Figure 4.12(A)). HA+14wt% alumina appears to produce the most (Figure 4.12(C)). This is confirmed by the data (Figure 4.13(A)). HA+14wt% alumina produces twice the number of particulates than either pure HA or HA+6% alumina. Interestingly, the HA+14wt% sample also produces larger particles on average than either pure HA or HA+6wt% alumina (Figure 4.13(B)). Thus, it may be a combination of both the size and number of particulates that has an adverse effect on cell response.

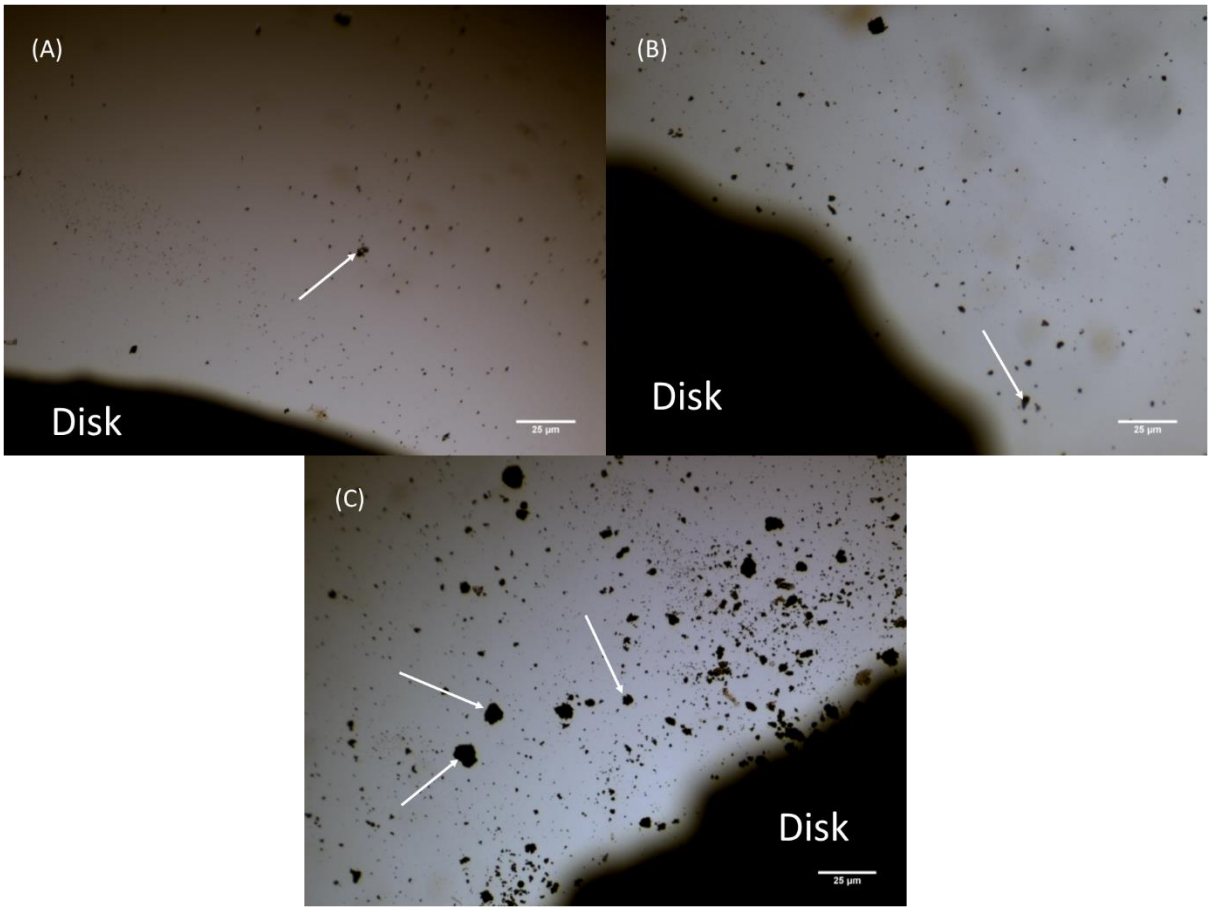

Figure 4.12. *Images of debris from disk samples after one week incubation in cell culture media. (A) Pure HA, (B) HA+6wt% alumina and (C) HA+14wt% alumina. Scale bars are 25µm. White arrows indicate examples of particulates. Note the increased debris surrounding the HA+14wt% disk.*

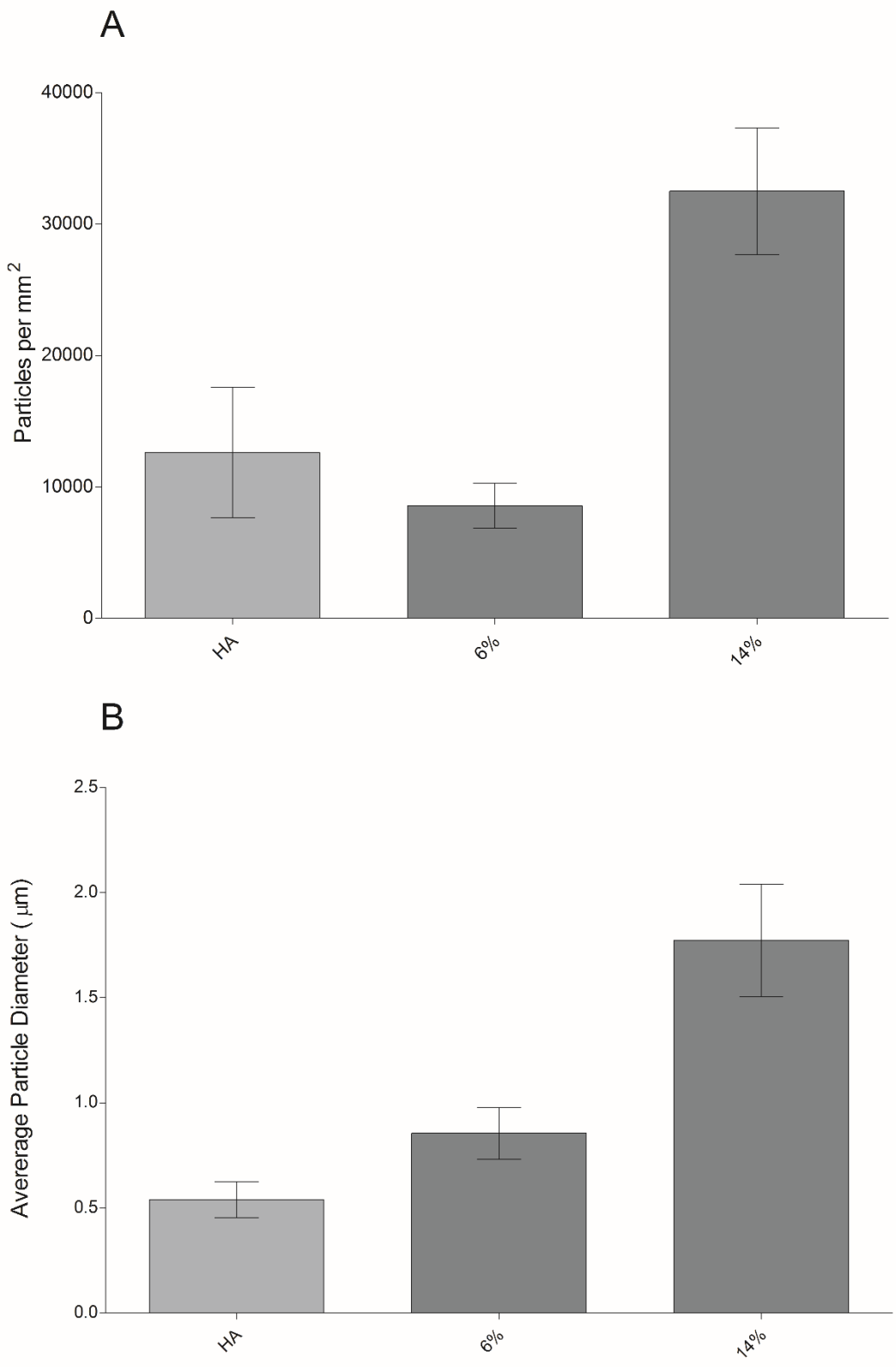

Figure 4.13. *(A) Number of debris particles per mm^2. (B) Average particle diameter. Data is based on the mean of three images each. Error bars represent one standard error of the mean.*

4.4 Discussion

4.4.1 Ball-Milling vs. Direct Deposition

The key objective arising from the sintering temperature experiments in Chapter 3 was to develop a custom topography consisting of an underlying basal layer with a surface wavelength parameter appropriate for MSC adhesion. Into this basal layer nanoscale topographical features were to be incorporated to provide the stimulus for cell proliferation. Two methods were attempted to achieve this end; ball-milling a mixture of HA and alumina and directly depositing an alumina suspension onto the HA surface. The surface resulting from direct alumina deposition was somewhat irregular and unpredictable as well as the topographical features being muted and indistinct (Figure 4.3). Furthermore, it induced a depressed cell response in comparison to the ball-milled surfaces (Figure 4.7). These factors, along with the greater simplicity of the ball-milling protocol, led to ball-milling becoming the method of choice for phase addition. All subsequent project work relates to topographies generated by ball-milling HA and alumina precursor powders.

4.4.2 Material Analysis

A comparison between the idealised design and the result of alumina nanophase addition to the HA precursor is shown in Figure 4.14.

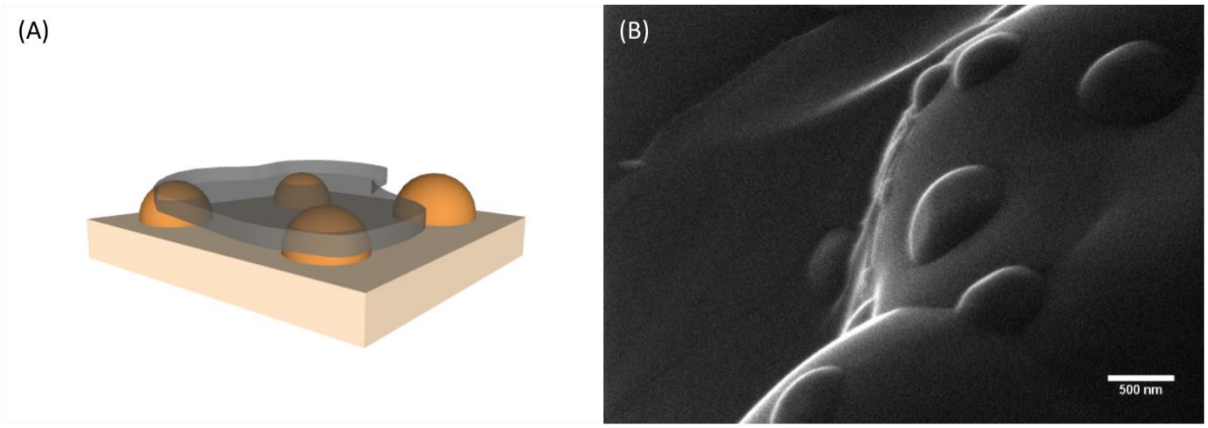

Figure 4.14. *(A) Representation of target surface including underlying basal layer and embedded topographical features. (B) He-ion image of HA+5wt% alumina surface. Scale bar is 500nm.*

It is clear that the alumina nanopowder has had the desired effect; forming surface features 200-500nm in diameter. This is possible due to the much higher melting temperature of alumina, allowing it to remain discrete while the HA matrix sinters and changes shape around it. The alumina nanoparticles were confirmed to be in position post-sintering using EDX (Figure 4.5(B)).

White-light interferometry was used to produce quantified data on the surface morphologies. It does not appear as though this technique is capable of discerning the alumina nanoparticles from the surrounding HA matrix. This could be a resolution issue which, for white-light interferometry, is not as accurate in the XY plane as it is in the Z direction. However, the procedure proved capable once again of providing data on the underlying basal layer of the topography; specifically, the average surface wavelength. It will be recalled from Chapter 3 that this was the parameter that differentiated the surfaces modulated by sintering temperature. Whilst the surface wavelength did not differentiate the surfaces here, it did confirm that all the HA+alumina substrates exhibited surface wavelengths above the threshold value of 2.4µm that was deemed necessary for cell adhesion (Figure 4.4).

The XRD data revealed an interesting trend in the phase stability of the samples. The alumina acted to initiate the decomposition of the HA to α-TCP. This decomposition amplified steadily with increased alumina weight percentage up to approximately 10wt% whereupon all of the HA had been decomposed to α-TCP (Figure 4.6). It is hypothesised that the alumina nanoparticles act as nucleation points for decomposition to occur, as the pure HA used throughout this project has proved repeatedly to be phase stable at the sintering temperature employed (1350°C, see Appendix I). The variable HA to α-TCP ratio may have a useful application. It is generally understood that calcium phosphates display differing dissolution behaviour *in vitro* and differing resorption behaviour *in vivo* with HA being far less soluble than α-TCP [96]–[98]. The fact that the addition of the alumina nanophase allows control over the HA to α-TCP ratio means that the ultimate rate of resorption of the finished scaffold *in vivo* should be controllable also. A large-scale dissolution study would be required to verify this concept before animal trials but the underlying principle is sound.

The EDX data shed further light on what is happening at the interface between the HA matrix and the alumina nanoparticles. As mentioned above, the EDX map of aluminium (Figure 4.5(B)) shows that the alumina particles formed the nanoscale surface features as intended. In addition, EDX maps were produced for both phosphorus and calcium (Figures 4.5(C) and 4.5(D) respectively) which, together, should correspond to the location of the calcium phosphate. The phosphorus remains *in situ* in the calcium phosphate matrix as indicated by the negative spaces in that map being consistent with the locations of the alumina nanoparticles. Conversely, the calcium map is almost uniform in appearance with no such negative spaces. This strongly suggests that calcium ions have diffused across the HA/alumina interface and into the nanoparticles. This transfer of calcium ions would explain the shift in HA to α-TCP. It is possible that the calcium would then react with the alumina to form various calcium aluminates. This decomposition and subsequent reaction has been suggested before for this system [44], [51]; although with the

formation of an intermediate phase of calcium oxide. The reaction is given by Viswanath *et al* [51] as follows:

$$Ca_{10}(PO_4)_6(OH)_2 + 6Al_2O_3 \rightarrow CaO \cdot 6Al_2O_3 + CaAl_2O_4 + 3Ca_3(PO_4)_2 + H_2O$$

It should be noted that no phase other than HA and α-TCP could be detected from the XRD data presented here (Figure 4.6); be it calcium oxide, alumina or calcium aluminate. It may be that the calcium phosphate peaks are simply too strong and are masking the new phase. Viswanath *et al* [51] report this exact problem in determining the phases formed from the reaction of the calcium and alumina. The phosphate peaks were simply too strong and obscured the relevant calcium aluminate peaks. They resolved the issue by dissolving the composites in hydrochloric acid and filtering the solutions. The calcium aluminates did not dissolve and could thus be examined by XRD after drying. That method was not attempted here due to time constraints.

If the XRD data from Viswanath's calcium aluminates is compared with that of the HA+10wt% alumina material described here, the problem can be illustrated (Figure 4.15).

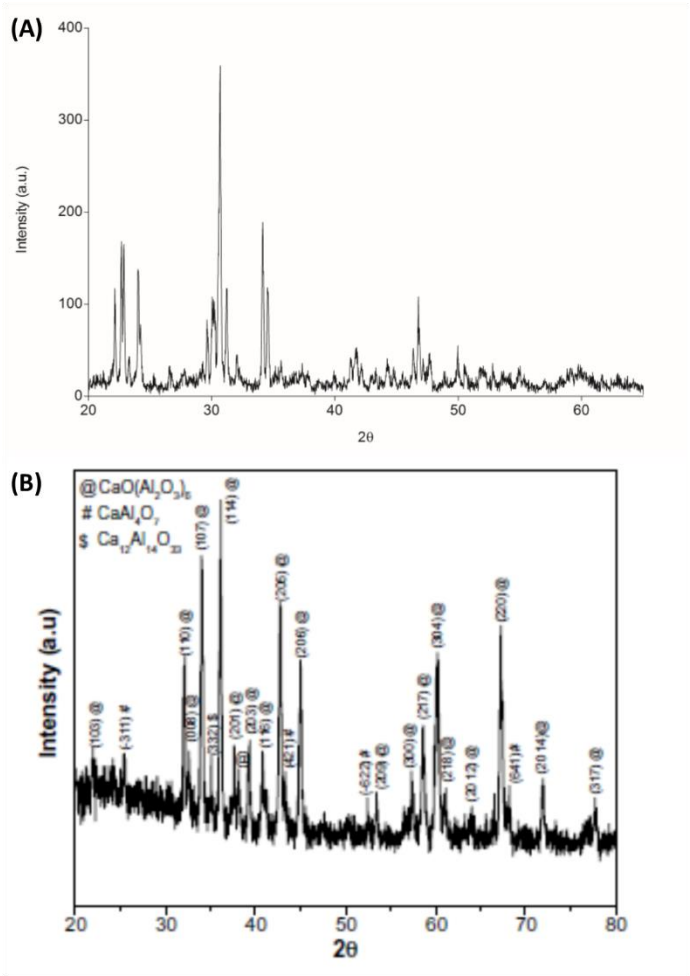

Figure 4.15. *XRD data for (A) HA+10wt% alumina and (B) calcium aluminates as described by Viswanath et al [51].*

Many of the distinctive peaks for calcium aluminate (Figure 4.15(B)) are located between 30 and 45°. This is also where many of the characteristic calcium phosphate peaks are located (Figure 4.15(A)). Even if this were not the case, the intensities of the two phases could be vastly different (unfortunately no indication of the peak intensities of the calcium aluminate is given by Viswanath *et al*), again serving to hide the calcium aluminate peaks.

The available XRD and EDX data combined with the consensus in the literature leaves one or more calcium aluminates as the most likely candidate for the new chemical formulation of the nanoparticles after sintering.

4.4.3 MSC Response

The surface wavelength results implied that all of the HA+alumina topographies should be conducive to cell adhesion. This proved to be the case, with cell activity significantly above zero on all substrates at day one (Figure 4.8). However, over a longitudinal culture period, there proved to be substantially differing behaviour from the cells across the various groups. The key result here is the huge increase in cell proliferation observable on the 2-10wt% alumina disks. This manifested itself as an acceleration in activity across the first two weeks of culture followed by a high plateau level of activity for the subsequent two weeks. On the other hand, both pure HA and the tissue culture plastic control both had slower initial rates of proliferation and overall lower equilibrium levels of cellular activity during the latter stages of culture. In fact the proliferation rates of both pure HA and the control actually decreased between days 11 and 18 before levelling off.

The biggest differences between the various groups occurred at the halfway point of culture, day 15, and at the end, day 32. By day 15, HA+2wt% alumina (overall the best performer) exhibited 185% of the cell activity of pure HA and 430% of the activity on the control. At day 32, HA+8wt% alumina generated the best response with 261.5% of the activity of pure HA and 447% of the control. This represents a major increase on the proliferation rates attainable on either tissue culture plastic or pure HA. As such, the addition of the alumina nanophase in quantities from 2-10wt% in order to increase cell proliferation can be deemed highly successful. HA+2wt% alumina was the best performer in general but 6%, 8% and 10wt% were statistically indistinct from it (Figure 4.9).

The increased proliferation of the MSCs on the 2-10wt% alumina substrates over pure HA can be directly attributed to the novel topography on the alumina surfaces. The non-contact experiment results (Figure 4.10) show that once the cells have been removed from direct contact with the substrates they lose the benefits provided by the alumina surfaces. In the non-contact

set-up, pure HA was the highest performer overall. This was in spite of the fact that all the cells were still in fluidic contact with the samples through the insert membrane. Thus it is unlikely that the positive effect observed when the cells were in contact with the 2-10wt% alumina surfaces was due to any chemical or dissolution effect as this would still be expected to appear in the non-contact data.

It will be immediately noted of course that the success of the alumina nanophase addition did not extend to the 12wt% and 14wt% alumina groups. In fact, these samples consistently underperformed all others in quite a striking low-activity plateau in the contact results (Figure 4.8). Furthermore, they continued to underperform the other groups in the non-contact experiment, although not as significantly. The fact that this phenomenon was apparent in both contact and non-contact environments suggests that it is not a topographical effect but rather some factor that manifests in solution or is at least fluid transportable.

The reason for the sudden collapse in cell viability between 10-12wt% alumina is not immediately clear. One initial theory was that some unanticipated cytotoxic phase had been created as a by-product of the HA decomposition to α-TCP in combination with the alumina. However, no evidence of such a phase could be gleaned from the XRD data. In addition, the literature suggests that the only chemical phases that arise from this system are calcium oxide, tri-calcium phosphate and calcium aluminates [44], [51]; none of which are known to be cytotoxic. In fact, calcium aluminates have previously been used in tissue engineering scaffolds and are widely employed in dental cements [92], [99]. Hence it appears unlikely that a cytotoxic phase has been created between the 10wt% and 12wt% alumina concentrations.

As alluded to briefly in Section 4.3.6, excess calcium ions have been linked with programmed cell death or apoptosis [91]. From the EDX data here (Figure 4.5) it was shown that calcium ions are diffusing out from the HA matrix into the alumina nanoparticles. Thus it is not unreasonable to suggest that given enough nucleation points (i.e. a high enough concentration of

alumina), an excess of calcium might diffuse into the surrounding media and have an adverse effect on the MSCs. The purpose of the calcium assay was to determine if this was the case. The results showed that it was not (Figure 4.11). Statistically, there is no more calcium released from either pure HA, HA+6wt% alumina or HA+14wt% alumina disks then would be expected to be found in the cell culture media anyway. Even when normalising that data to take account of the weight of each individual sample it is noticeable that both the HA and 14wt % groups were statistically indistinguishable. Therefore, an excess of calcium ions in solution cannot be blamed for the poor performance of the cells on the high alumina surfaces.

Another potential cause for the inhibited cell activity on the 12wt% and 14wt% alumina groups could be debris particles dissociating themselves from the bulk material during immersion in the cell culture media. Research has been done on the effects of particulates on bone-related cells due to the propensity of orthopaedic implants to produce wear debris over time [94], [100], [101]. Much of this work has focussed on titanium alloys and medical grade plastics as they form the common materials in orthopaedic prostheses. However, the results of these studies can still be illuminating. For example, one study by Vermes *et al.* and described in a review by Goodman *et al.* [94], showed that proliferation of MG-63 osteoblasts decreased in a dose-dependent manner when exposed to <3µm diameter particles of titanium alloys and chromium orthophosphate. They also showed that the cells engulfed the particles by phagocytosis. Thus it is reasonable to suggest that if one or more of the HA/alumina groups described here was undergoing greater particulate dissociation than the others, this might trigger a corresponding drop in proliferation as the MSCs phagocytosed the debris.

Samples with >10wt% alumina indeed proved to be producing more particulate debris than either pure HA or those with 10wt% alumina or less after a week's immersion in cell culture media. The microscope images in Figure 4.12 give a good qualitative description of the additional debris surrounding the main 14wt% disk. Using ImageJ to run a "Particle Analysis" on cleaned and

thresholded regions of interest from each image, quantitative data was also be obtained. 14wt% alumina produced over two and a half times the number of particles per mm^2 than pure HA and over three and half times those produced by the 6wt% disks (Figure 4.13(A)). This is a striking difference and one which strongly suggests that the cells find it difficult to deal with excess particle debris and necessarily greatly reduce their proliferative capacity.

In addition to the 14wt% samples producing a higher number of particles, the particles themselves were, on average, larger (Figure 4.13(B)). This implies a wholesale disintegration of the outer surface of the disk. Such an unstable surface would naturally provide cells with an extreme adhesion challenge. This is different to the instant cell death observed on low sintering temperature samples in Chapter 3. In that case, even initial cell adhesion proved impossible. Here, cell survival is possible but proliferation is non-existent and viability decreases over time. Thus, it may be that in addition to a reduction in proliferation due to the phagocytosis of particulates, cells are being lifted from the surface due to its dissociative nature. Cells left in suspension would quickly die and further negate any potential proliferation.

From the data available, the particulate debris theory provides the best explanation for the depressed performance of the 12wt% and 14wt% alumina groups. No additional cytotoxic phase was evident from the data or predictable from the literature. Ionic dissolution was indifferent across the various groups. There has been some suggestion that alumina nanoparticles in isolation can cause fibroblast and macrophage apoptosis after being phagocytosed [102]. However, the particles used in that study were 13nm in diameter, so at least 10 times smaller than those employed here. The same study found no cytotoxic effect from nanowires 200-400nm in length, so again this indicates a phagocytic effect and nuclear damage to the cell after engulfment of the smaller nanoparticles. Taken together, these strands all point to the excess debris from the 12wt% and 14wt% groups causing the reduced proliferative capacity. Further biochemical study is required to examine how exactly the cells are behaving on the various

surfaces and to ultimately determine the reason for the MSCs' aversion to the 12wt% and 14wt% alumina surfaces.

This chapter is the proof of concept for the optimized scaffold. A novel topography was designed and implemented which served to radically increase cell proliferation on the surface. It was felt that this result was good enough to take forward to full 3D benchmarking to assess the new scaffold's performance in as rigorous and *in vitro* environment as possible. The addition of the alumina phase to the HA also raised some interesting questions; not all of which have been fully addressed. The apparent cell viability threshold at 10wt% is the obvious one. While every effort has been made to find a logical explanation for this, more work is certainly required. Having said that, the disk debris hypothesis is a strong one and fits all the data currently available.

Ultimately, the salient result from this chapter is the vastly increased cell proliferation achievable with the addition of between 2wt% and 10wt% alumina nanopowder to the HA precursor. The next step in the project was to translate this formulation into full, three-dimensional scaffolds and verify its efficacy. The following chapter details that work along with extensive *in vitro* benchmark testing.

4.5 Conclusion

It was found that the addition of nanophase alumina to HA precursors and sintering at 1350°C produced a smooth, basal topography with raised features 200-500nm in diameter. This topography, produced by formulations of HA+2-10wt% alumina, proved capable of improving cell proliferation by up to 261.5% over pure HA alone. The addition of the alumina also had the effect of accelerating decomposition of the HA to α-TCP resulting in a gradual shift in the ratio from pure HA at 1wt% alumina to pure α-TCP at 10wt% alumina. Concentrations of alumina greater than 10wt% produced substrates that were not conducive to proliferation and long-term cell survival.

It is hypothesised that this is due to the bulk instability of these materials producing excess particulate debris and resulting in cell phagocytosis.

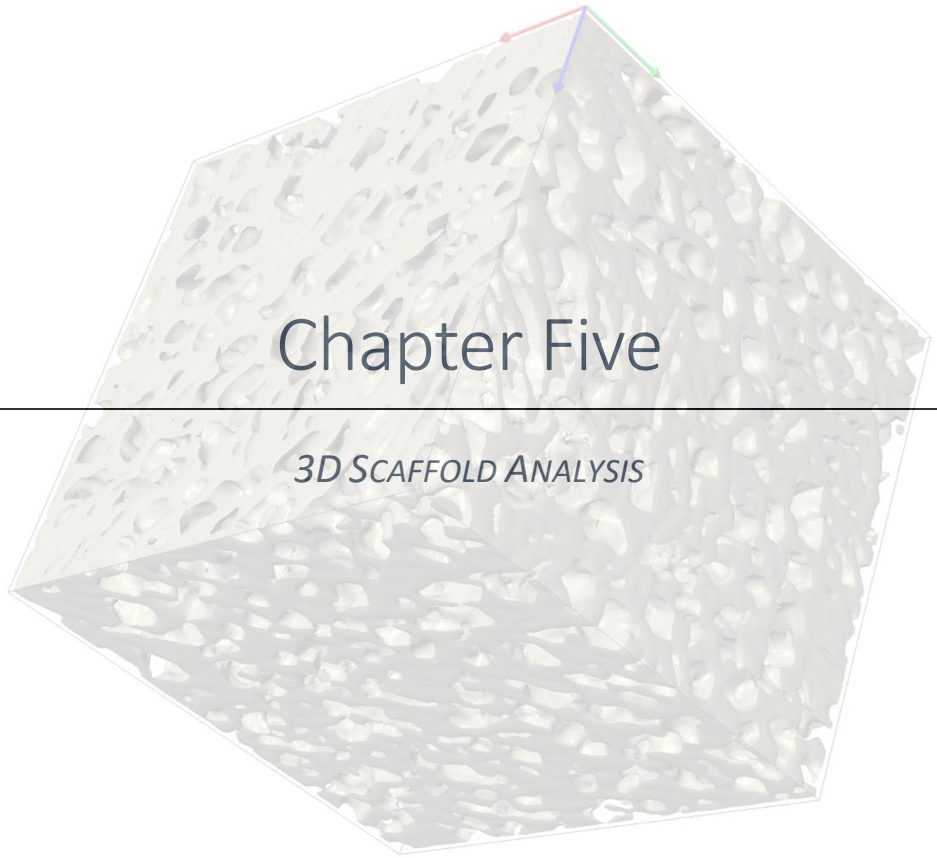

Chapter Five

3D SCAFFOLD ANALYSIS

5.1 Introduction

Despite the many positive results seen in the analysis of the disks in previous chapters, the real proof of concept comes when those results are repeated in full 3D constructs. Furthermore, it is in three dimensions that the novel scaffold must be assessed against its potential industrial competitors. It has been stated repeatedly that much of the value of this work relies on the fact that changes to the scaffold's topography must be translatable from 2D to 3D. This chapter aims to prove that that is the case with the formulas introduced in the previous chapter. In addition, general evaluation and benchmark testing of the construct are described along with a study on its inflammatory properties. All of this information is crucial for determining the overall practicality, both commercially and clinically, of the scaffold.

5.2 Materials and Methods

5.2.1 Scaffold Manufacture

Scaffolds were manufactured to the same specifications laid out in Chapter 3. HA/alumina precursor powders were prepared as per the formula in Chapter 4.

5.2.2 *In Vitro* Scaffold Analysis

Based on the disk results described in Chapter 4, HA+5wt% alumina was deemed to be the most appropriate scaffold formulation to take forward for full 3D investigation. Some additional work was also performed on HA+10wt% alumina to ensure that trends seen with increasing alumina percentage in 2D were repeated in 3D.

5.2.2.1 Cell Culture

As with the disks previously tested in Chapters 3 and 4, all samples were sterilized by heating to 121°C for one hour in a vacuum oven (Binder, Tuttingen, Germany) prior to culture. Samples were seeded with porcine bone-marrow-derived MSCs at a density of 50,000 per scaffold in 50µl of media. Samples were incubated at 37°C for four hours before adding a further 700µl of media consisting of Dulbecco's Modified Eagle Medium (DMEM) Glutamax (Gibco, Dublin, Ireland), 10vol% foetal bovine serum, 2vol% penicillin/streptomycin and 0.1µl/ml amp-B (all Sigma-Aldrich) to each. Cells were cultured for varying periods up to one month at 37°C and assayed every three to four days. Pure HA scaffolds were employed as controls.

5.2.2.2 Scaffold: Exposed Interior vs. Exterior Performance

As part of the manufacturing process, a thin, relatively dense layer can form on the top and bottom edges of the scaffold green body. In order to determine what effect this layer might have on cell performance, the activity of cells seeded on the top surface of scaffolds was compared with the activity of those seeded on scaffold surfaces from the interior of the green body. Interior surfaces were exposed by cutting away the outer layers of the scaffold green body before sintering.

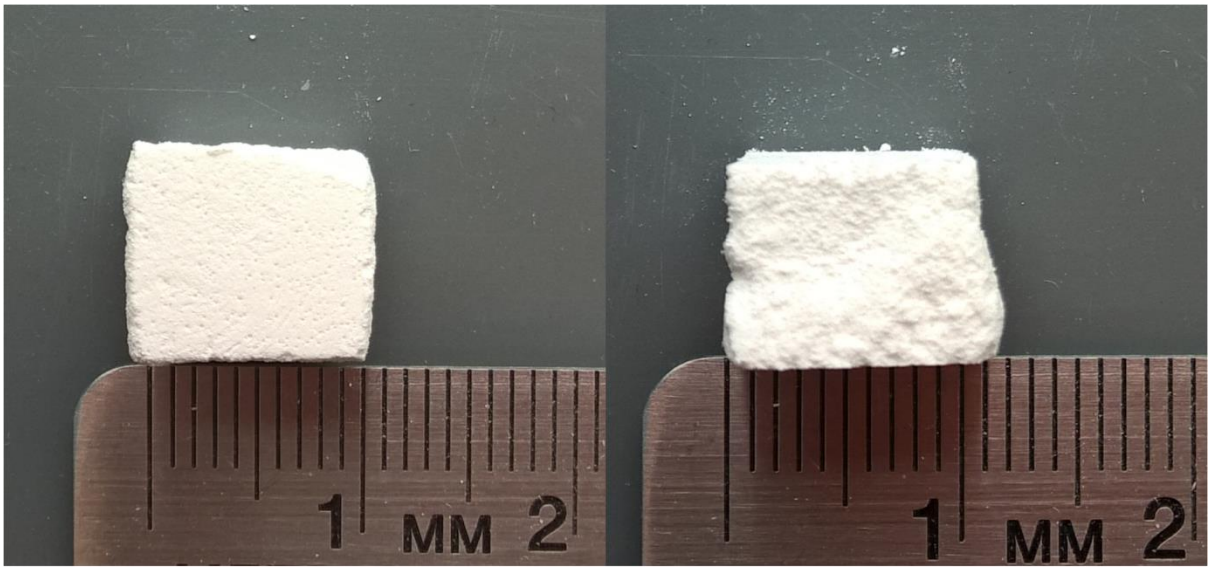

Figure 5.1. *Exterior (left) and interior (right) surfaces of a scaffold green body.*

5.2.2.3 Benchmark Testing

An industry leading bone graft substitute Bio-Oss® (Geistlich Sons Ltd., Manchester, UK) was used as a comparator to assess the construct's overall performance. Bio-Oss is a decellularized bovine bone product widely used in the field of oro-maxillo-facial and dental surgery. It is available in both block and granular forms; blocks being used mainly for larger, restructuring applications and granules for cavity filling. Both were employed here to inspect the full range of capabilities of the novel HA+alumina scaffolds.

The Bio-Oss block was cut down to 5x5x5mm cubes for ease of analysis using an Accutom-50 diamond saw (Struers Ltd., Rotherham, UK). These cubes were compared to Ha+5wt% alumina samples of a similar size.

Granular Bio-Oss was sourced in the 1-2mm nominal particle size range. HA+5wt% alumina scaffold samples were lightly ground in a pestle and mortar to make granules of a similar size for comparison.

5.2.3 Resazurin Media Assay

Cell proliferation and activity were assessed using the same resazurin method described in Chapter 3.

5.2.4 Alkaline Phosphatase Activity (ALP) Assay

Alkaline phosphatase production is an early marker of osteogenesis in pluripotent cells. The test was introduced here to assess how the scaffold formulations and matrices as a whole affect the tendency of the MSCs to differentiate down the osteogenic line. 2-10wt% alumina samples were tested along with pure HA and a tissue culture plastic control in order to examine whether ALP production varied with alumina content.

The ALP activity induced in MSCs by scaffolds of various concentrations of alumina was measured using a SensoLyte pNPP Alkaline Phosphatase Assay Kit (Colorimetric) (Eurogentec SA, Seraing, Belgium). Cell culture proceeded as per the proliferation assay and samples were analysed at days seven, 14 and 21.

ALP standards were prepared and at each timepoint 50µl of each standard and sample was transferred in triplicate to individual wells of a clear, round-bottomed microplate. Under minimal lighting conditions, 50µl of colorimetric ALP substrate was then added to each well. The

plate was covered and allowed to incubate for 40 minutes before being read in a Synergy HT microplate reader (BioTek, Winooski, VT, USA) at 405nm absorbance.

5.2.5 Inflammatory Response to Materials *in Vitro*

As outlined in Chapter 2, the potential for any implanted material to cause an acute inflammatory response should be fully understood. To this end, a relatively simple experiment was performed to assess the difference in immune response to scaffolds of various alumina concentrations and Bio-Oss.

Experiments were performed using bone marrow derived dendritic cells from C57 mice and repeated using macrophages from the same source. These cells play a significant role in the immune system and would be heavily involved in any potential reaction to an implanted scaffold. Cellular supernatant was analysed for expressions of IL1-α, IL1-β and TNF-α with culture media providing the control.

Cells were primed with lipopolysaccharide (LPS) (100ng/ml) and seeded directly onto the construct surfaces ($1x10^6$ cells/ml). After 24 and 72hours the supernatants were harvested and the concentrations of the various cytokines produced were quantified using DuoSet ELISA kits (R&D Systems Inc., Minneapolis, MN, USA), according to the manufacturer's instructions.

5.2.6 Helium-ion Microscopy

Prior to imaging, cells were fixed to the scaffolds in 3% gluteraldehyde (Merck, Hohenbrunn, Germany) for two hours, followed by dehydration, in 10 minutes stages, through a series of ethanol concentrations (10%, 30%, 50%, 70%, 95%) followed by 30 minutes in 100% ethanol and atmospheric evaporation.

In order to avoid the difficulty of sputter coating the porous constructs and to take advantage of its greater resolution and depth of field, samples were imaged using a Zeiss Orion Helium-ion microscope (Carl Zeiss Microscopy, Jena, Germany).

5.2.7 Statistical Analysis

All experiments were duplicated. Groups were evaluated using one-way analysis of variance (ANOVA) and Tukey's comparison test. Results with a $p \leq 0.05$ were considered significant. All analysis was performed in Minitab (Minitab Ltd., Coventry, UK). Graphs were produced in GraphPad Prism 5 (GraphPad Software Inc., La Jolla, CA, USA).

5.3 Results

5.3.1 Surface Morphology

In Chapter 3 it was shown that the surface morphologies produced by varying sintering temperature were comparable in both two- and three-dimensions. The same comparison can be made with the surfaces generated by alumina nanophase addition. Figure 5.2 is a He-ion microscope image showing the detail of a HA+5wt% alumina scaffold pore surface. The raised alumina features can clearly be distinguished from the surrounding HA matrix.

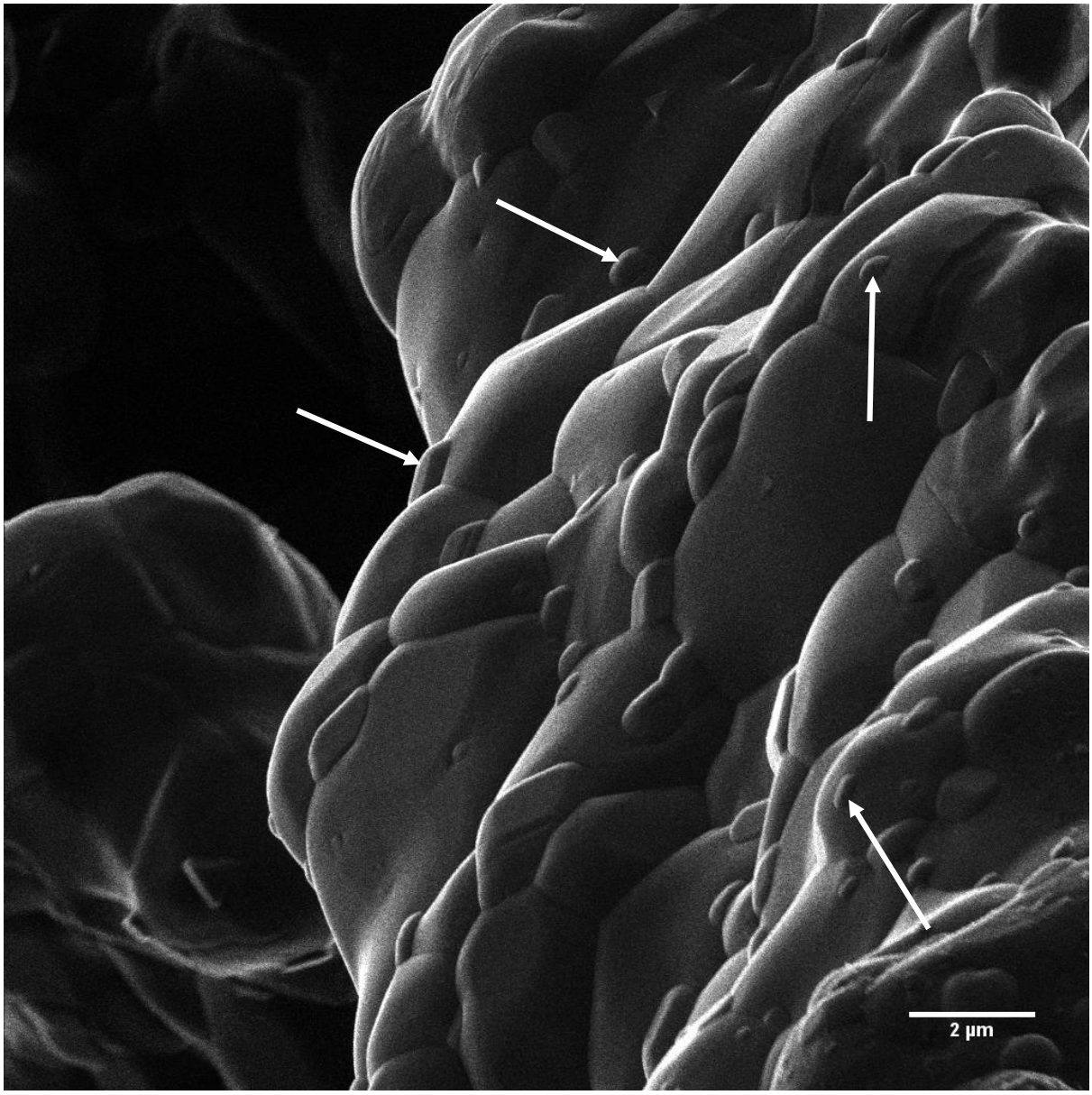

Figure 5.2. *He-ion microscope image of HA+5wt% alumina scaffold pore surface. Examples of alumina nanoparticles indicated by arrows. Scale bar is 2µm.*

5.3.2 Cell Culture

5.3.2.1 HA/Alumina Scaffolds with MSCs

It was imperative in the scale-up to three dimensions that the positive results described in Chapters 3 and 4 translated to the full constructs. To verify this, MSCs were seeded onto pure HA,

HA+5wt% and HA+10wt% scaffolds and cultured for two weeks with activity measured by resazurin assay.

The positive effects of 5wt% alumina addition were again apparent with 5wt% alumina significantly outperforming the pure HA and 10wt% alumina constructs. By day 14 the 5wt% alumina scaffold induced 157% of the cell response caused by pure HA (Figure 5.3). As was observed before on the 2D disks, 10wt% alumina gave a lower response than either 5wt% or HA but still allowed cell survival.

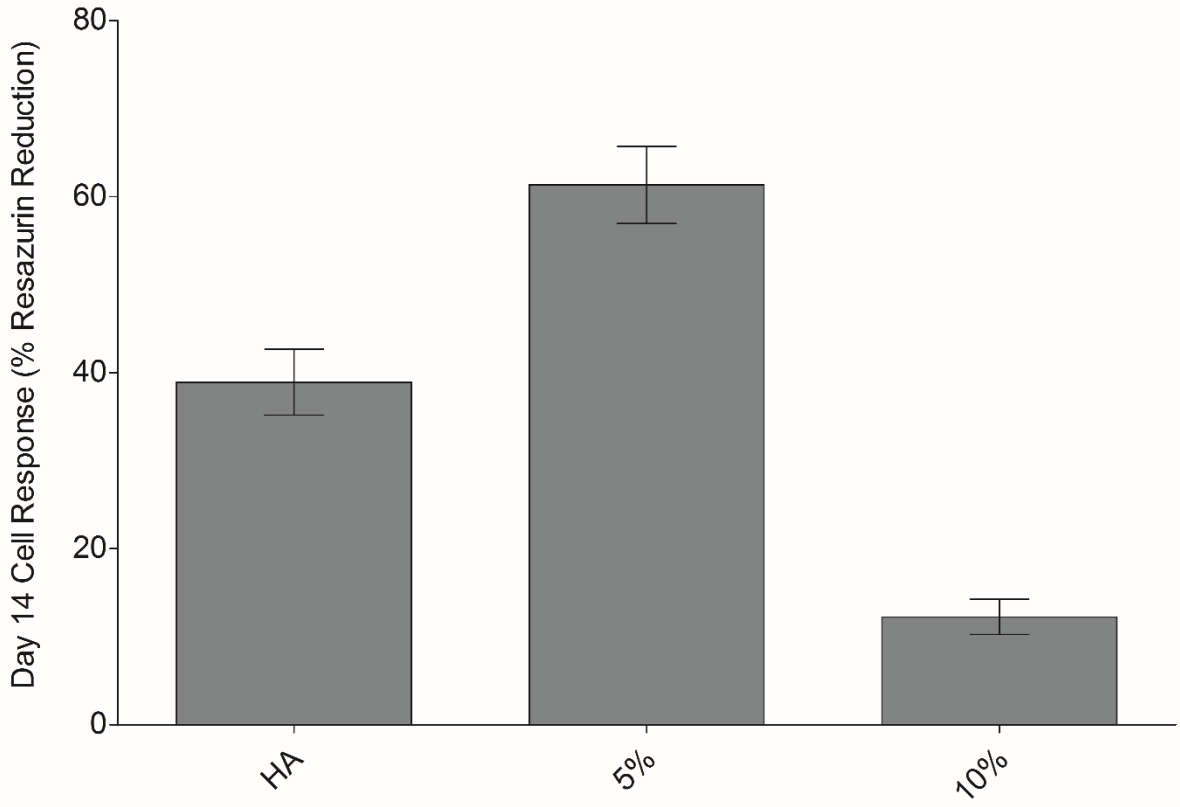

Figure 5.3. *Day 14 cell response to pure HA, 5wt% and 10wt% alumina scaffolds. Error bars represent one standard error of the mean.*

5.3.2.2 Exterior Surface vs. Exposed Interior Surface

It was suspected that the dense layer that forms on the outer surfaces of the scaffold block during the manufacturing process would affect the MSCs behaviour. In order to investigate this, cells were cultured on scaffolds either with the layer in place or with it removed.

Seeding cells onto scaffold surfaces exposed from the interior of the green body proved significantly more conducive to proliferation than the alternative of seeding the cells directly onto the outer surfaces. The increased cell activity was observed on all three samples; pure HA, HA+5wt% and HA+10wt% alumina (Figure 5.4). 5wt% alumina remained by far the strongest performer with 150% more cell activity apparent by day 14 than on the pure HA equivalent.

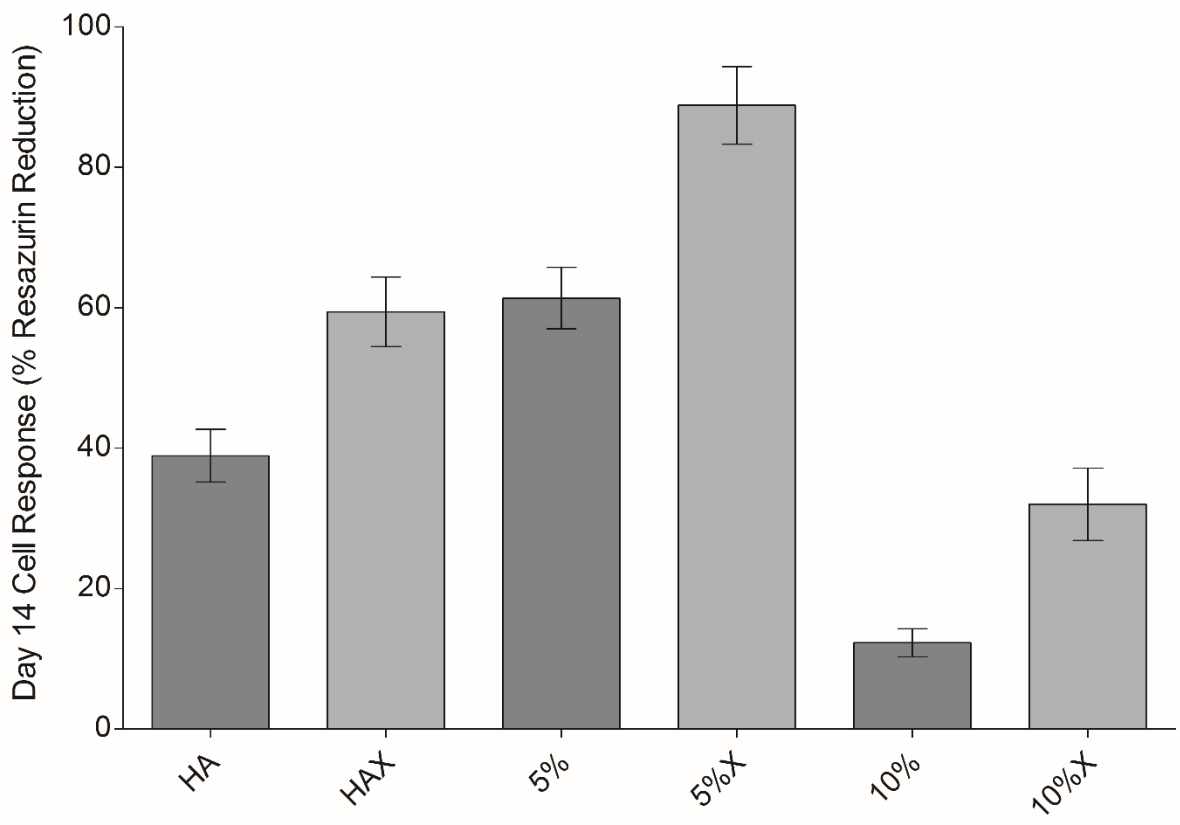

Figure 5.4. *Day 14 cell response to both the interior (denoted by "X") and exterior scaffold surfaces. Error bars represent one standard error of the mean.*

5.3.3 Benchmark Testing

Aside from full *in vivo* trials, one of the most rigorous tests that can be applied to a new biomaterial is direct comparison to a leading industrial competitor. Geistlich Bio-Oss was selected for this purpose due to its widespread use in clinical practice. The indications of cellular proliferation on HA+5wt% alumina were extremely favourable in comparison to the Bio-Oss block (Figure 5.5). After 18 days of culture there was nearly ten times as much cell activity on the 5wt% alumina scaffold as on Bio-Oss.

A similar result was observable when scaffold granules were used as the vehicle of cell culture (Figure 5.6). By day 12 there was again ten times the cell activity on the 5% scaffold granules an on Bio-Oss.

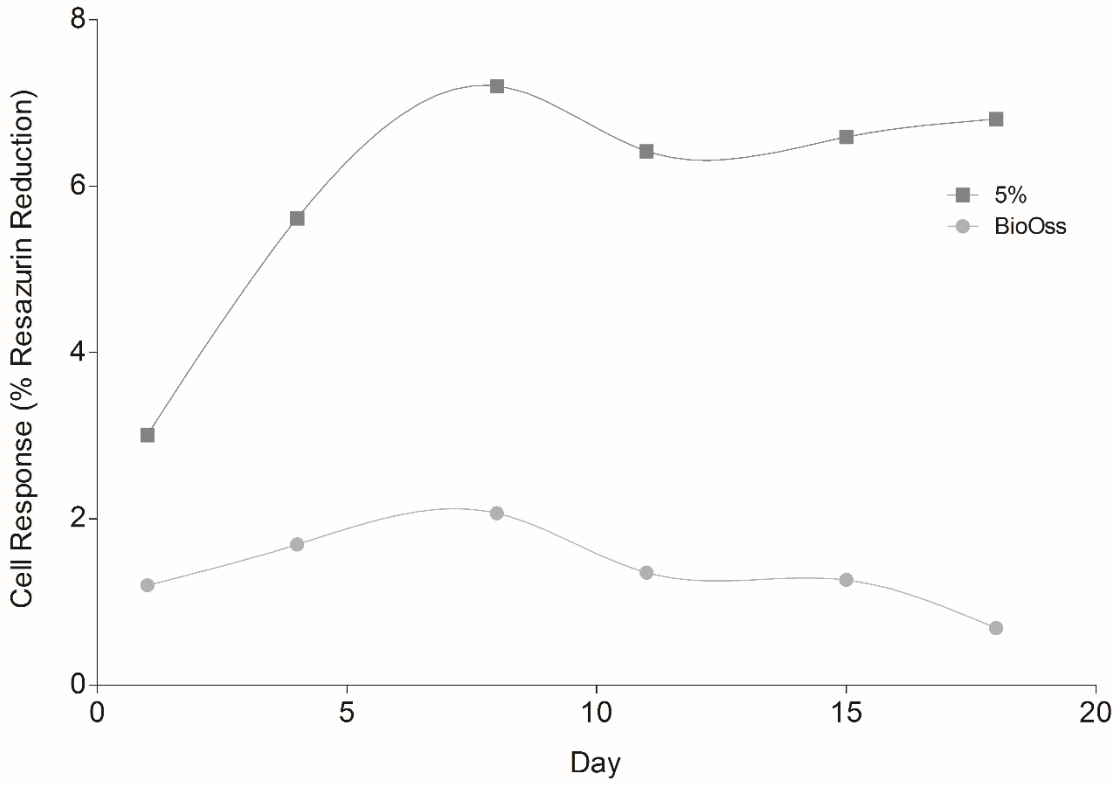

Figure 5.5. *Cell response to HA+5wt% alumina scaffolds and Geistlich Bio-Oss block scaffolds across 18 days of culture.*

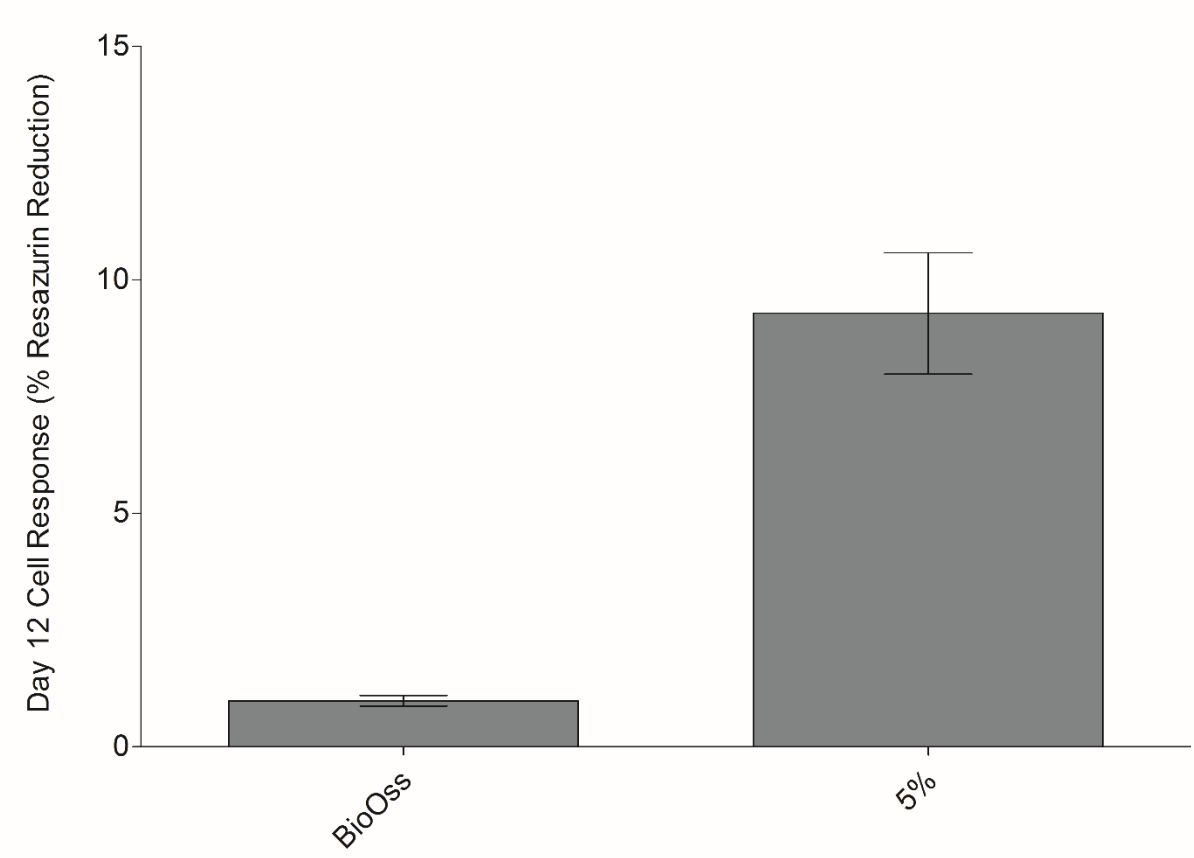

Figure 5.6. *Day 12 cell response to Bio-Oss and 5wt% alumina scaffold granules. Error bars represent one standard error of the mean.*

5.3.4 Alkaline Phosphatase Activity (ALP) Assay

ALP activity is considered an early indicator of osteogenic potential in progenitor cells. The assay was employed here to ascertain if ALP production varied with alumina content in the scaffolds. As this was the first occasion that an ALP assay was being introduced in this work, it was decided to test a range of alumina contents (2-10wt%) along with pure HA and a tissue culture plastic control.

No significant differences are observable in the ALP activity between any of the groups until day 21 (Figure 5.7). At this point it became apparent that the HA induced the most ALP production of any of the scaffolds. There was still no difference between 2-8wt% alumina and the control whereas 10wt% alumina was markedly depressed. In addition 2wt% alumina yielded more

ALP production than any other scaffold at day 21 bar pure HA. This showed that while the addition of the alumina to the HA apparently reduced its propensity to induce osteogenesis, it did not eliminate it completely.

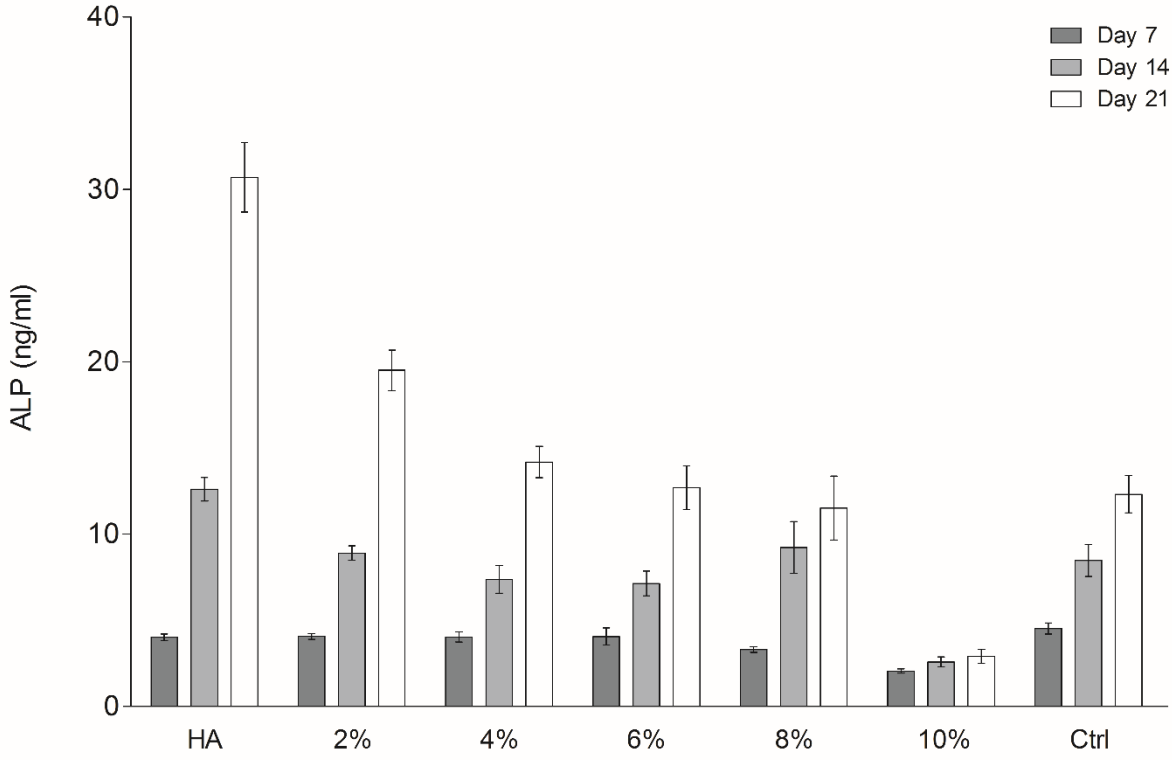

Figure 5.7. *ALP production in MSCs induced by HA, 2-10wt% alumina and control surfaces at days seven, 14 and 21. Error bars represent one standard error of the mean.*

5.3.5 Inflammatory Response to HA/Alumina Scaffolds *in Vitro*

As discussed in Chapter 2, the issue of inflammatory response to implanted biomaterials is often overlooked. Despite this, it can have significant consequences for the healing outcomes of the implant. Here, pure HA, HA+alumina and Bio-Oss scaffolds were tested to investigate their inflammatory tendencies. For the same reasons outlined for the ALP assay, a range of alumina

concentrations (2-10wt%) along with pure HA were tested. Two cell-types were employed in the analysis, both murine; macrophages and dendritic cells. These particular cells were isolated from bone marrow tissue and play a key role in inflammation. Thus, they provide a good model for the potential immune response that might be encountered *in vivo*. Expressed levels of the common inflammatory cytokines TNFα, IL-1α and IL-1β at 24 and 72 hours were examined.

No significant production of TNFα and IL-1α was observed at 24 or 72 hours by either cell type, hence this data has been omitted for clarity. However, significantly more IL-1β was produced by both dendritic cells (Figure 5.8) and macrophages (Figure 5.9) in response to Bio-Oss compared to any of the novel scaffold formulations ($P<0.01$ at 72hrs). This is a clear indication that the novel HA/alumina scaffolds induced a depressed inflammatory response in the cells compared to Bio-Oss.

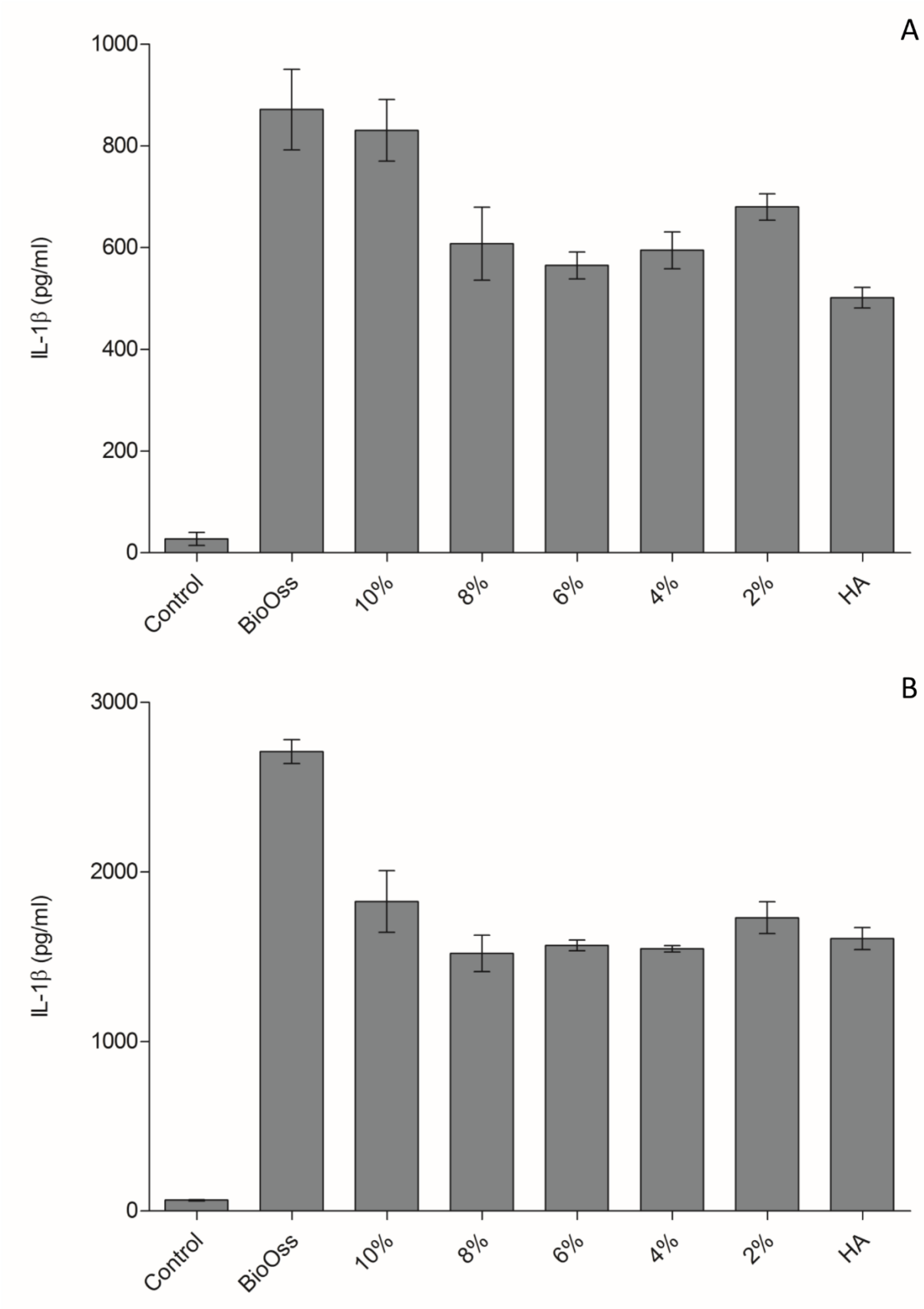

Figure 5.8. *IL-1ϐ expression by murine dendritic cells in response to Bio-Oss, pure HA and 2-10wt% alumina scaffolds at (A) 24hrs and (B) 72hrs.*

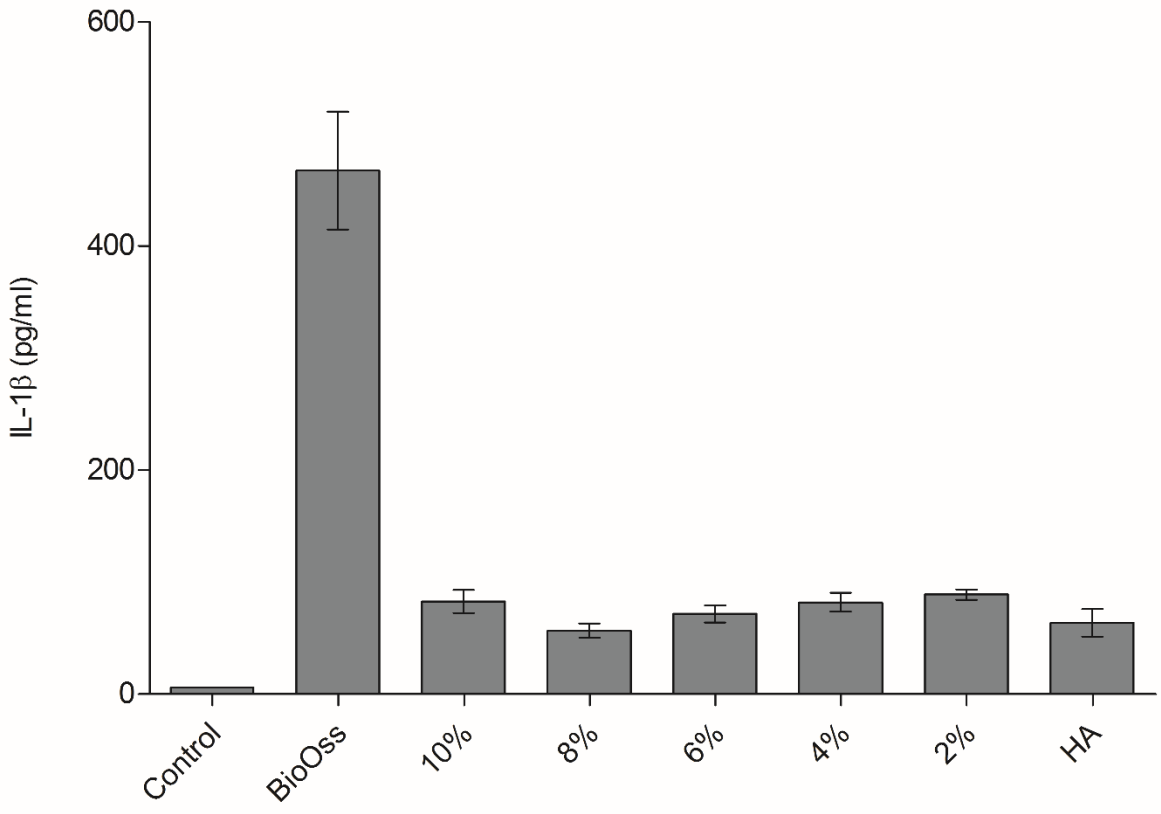

Figure 5.9. *IL-1ß expressed by murine macrophages in response to Bio-Oss, pure HA and 2-10wt% alumina scaffolds at 72hrs.*

5.4 Discussion

In Chapter 4, it was shown clearly by SEM and EDX that the addition of alumina nanoparticles into the HA matrix resulted in raised topographical features of a relevant size in 2D disks. He-ion microscopy showed the same effect here (Figures 5.2 and 5.10) in 3D scaffolds. This achieved the objective of developing a novel surface morphology that can be applied to the pore surfaces of 3D scaffolds using a simple, inexpensive protocol.

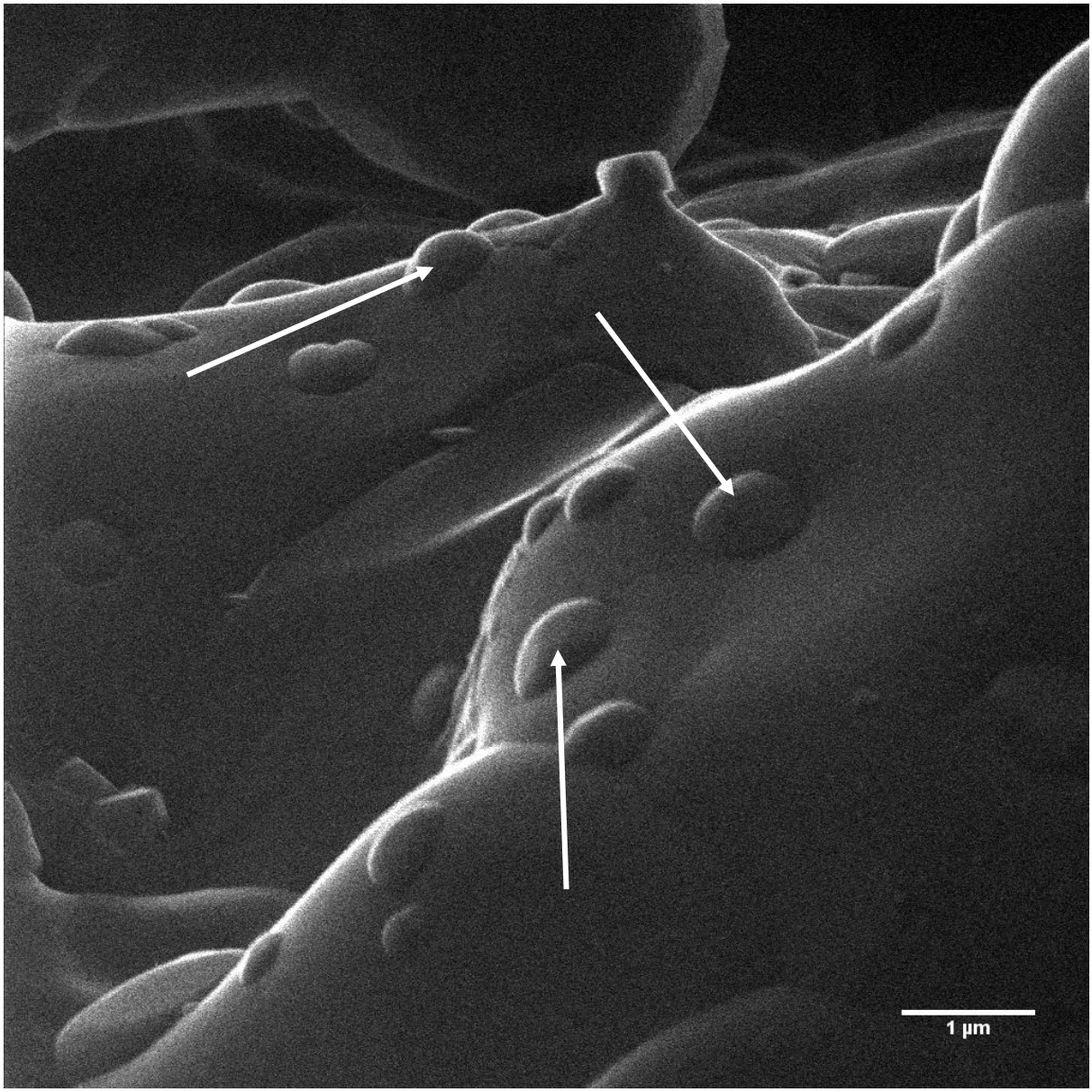

Figure 5.10. *He-ion microscope image of HA+5wt% alumina scaffold pore surface. Alumina particles indicated by white arrows. Scale bar is 1µm.*

Furthermore, this novel topography yielded the same positive results that were apparent in two dimensions. It was shown in Chapter 4 that anywhere between 2% and 8wt% alumina addition resulted in significant increases in cell performance but that this effect was lost above 10wt%. This outcome was borne out here in the 3D scaffolds with 10wt% alumina scaffolds not generating as much cell activity as pure HA. However, the 5wt% alumina constructs outperformed their HA counterparts by 157% by day 14 (Figure 5.3) which is a clear indication of the effectiveness of the new topography.

It was noted during the manufacturing phase of the various scaffolds that during freeze-drying, a dense layer of compacted precursor tended to form on the top surface of the green body. It was hypothesized that this layer would block access to the general pore structure of the matrix and thus hinder the ability of cells to engage with the pore surface topography. This proved to be the case, as when the green bodies were opened up prior to sintering and the cells seeded onto the inner pores of the scaffold, they tended to perform much better (Figure 5.4). This improvement was seen across the three different samples with the 10wt% the biggest improver; undergoing a 155% increase in cell performance. Both pure HA and 5wt% displayed cell activity increases of about 50% when cells were seeded onto the open pores. It is suggested that the reason for these improvements is the greater access to open porosity afforded cells seeded onto the exposed interiors of the scaffolds. The difference in microstructure is apparent from He-ion microscope images, illustrated here by the HA and HAX surfaces (Figure 5.11). Clearly, the exposed interior surface is more porous and offers increased ingress into the scaffold matrix.

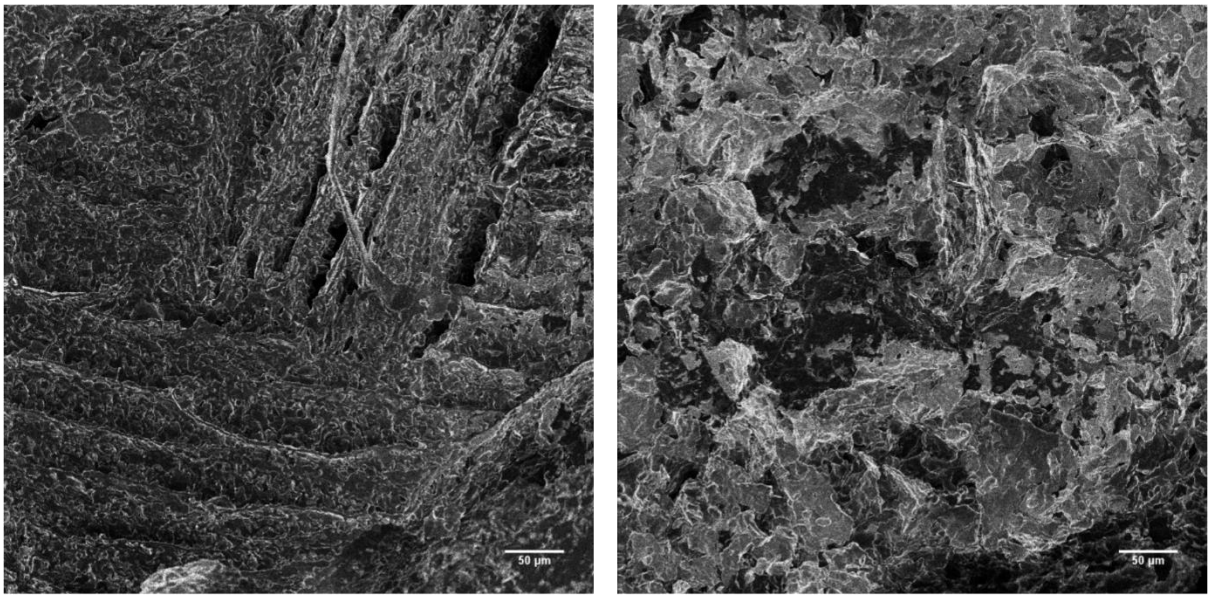

Figure 5.11. *Scaffold surfaces HA (left) and HAX (right). Scale bars are 50µm. Note the more open porous structure of the HAX surface.*

Overall, this result simply demonstrates the importance of continuing to think critically through all the manufacturing stages of a novel scaffold. The dense layer at the scaffold periphery could have seriously hindered the construct's osteoinductive properties, making it less effective as a bone graft substitute. It may be possible to alter the freeze-drying cycle or slurry formulation so that no such layer is formed; although that avenue was not investigated here. A simpler solution however, is simply to remove it either by cutting the green body or polishing the sintered block.

The key performance indicator for the novel scaffold was its comparison with the industry standard Bio-Oss. As described before, Bio-Oss is a decellularized bovine bone product produced in both block and granular forms. It was chosen due to its widespread clinical use in Ireland and abroad. There is some indication in the literature that Bio-Oss may not support cell proliferation to the same degree as some of its competitors [103], [104]. This would seem to be borne out by the data presented here. Certainly the HA+5wt% alumina scaffold strongly outperformed block Bio-Oss across nearly three weeks of culture with a consistently higher cell activity expression. By the end of the culture period, at day 18, nearly 10 times the cell activity was recorded on the

5wt% scaffold as on Bio-Oss. This result was confirmed in the granular forms of both scaffolds with a similar ten-fold increase of cell activity on 5wt% as on Bio-Oss.

The results of the Bio-Oss comparisons offer arguably the greatest indication of the potential for success of these novel scaffolds. The data is unequivocal; cell activity is an order of magnitude higher on the new topography presented here than it is on one of the industry's leading products. This alone is justification of the research as a whole and provides ample reason to continue study of this scaffold formula.

Further evidence in favour of the novel scaffold comes in the form of the inflammatory response of the various construct formulations, compared to the clinical standard Bio-Oss. The apparent lack of attention of much of the literature to the potential for an immune response to implanted biomaterials is discussed in detail in Chapter 2. It is clear that more collaborative work needs to take place between bioengineers and immunologists/biochemists to address some of the problems that will be encountered as the field of implantable technology accelerates. This is emphasised by the outperformance of the novel scaffold over Bio-Oss in the immunological trials described here. IL-1β is a cytokine typically indicative of inflammation [69]. While not directly cytotoxic, it has been shown to induce connective tissues to resorb their surrounding extra-cellular matrix [105]; this has obvious negative consequences for bone. With this in mind, the tendency of the novel scaffold to induce such low IL-1β production is a positive outcome.

It is possible that many of the osteoinductive advantages of current bone graft substitutes are being nullified by the biochemical signals occurring in response to their implantation. From this perspective it is encouraging that the inflammatory cytokine expression is so much more depressed in response to the novel HA and alumina formulas described here, in contrast to BioOss. This result is reinforced through confirmation by two independent cell lines (macrophages and dendritic cells), both of which would play a key role in the host's immune response to the implantation of the scaffold *in vivo*. It is also interesting to note that addition of the alumina

nanoparticles resulted in no discernible increase in cytokine production over the pure HA. This shows that the immune cells do not adversely react to the novel surface topography.

The one drawback to the novel scaffold formulation appears to be its reduced osteogenicity compared to pure HA, as indicated by the results of the ALP assay. ALP is a well-established early marker of osteogenic differentiation in MSCs [25], [81], [106] and its high production by cells cultured on the pure HA substrates is not surprising [88]. The fact that there was such a high rate of cellular proliferation on the low percentage alumina scaffolds means that some trade-off as regards differentiation was always possible. It is likely that it is merely a delayed onset effect and that cells would eventually differentiate down the osteogenic route in response to their chemical and mechanical surroundings; ALP production was shown to be increasing with time on the HA/alumina scaffolds (Figure 5.7). The differing behaviour of the HA and HA+alumina scaffolds throws up the interesting potential for a composite; for example an outer layer of pure HA to kick-start the differentiation process and bone integration, combined with an inner core of 5wt% alumina to increase MSC proliferation and combat core necrosis.

The culmination of this work was the comparison of the novel scaffold with Bio-Oss. The project aim can be said to have been achieved; cell proliferation on the original TCBE scaffold was greatly increased through the use of the novel, tailored surface topography. Furthermore, both proliferation and inflammatory response compare favourably with Bio-Oss. This proves the importance of testing implantable products for their immune response and is something that should become standard practice in the wider tissue engineering community.

The results are favourable enough to warrant further investigation into the scaffold as a commercially viable product. The *in vitro* due diligence has been done so the clear next step in the process is an animal model. This was not attempted here for both financial and ethical reasons. It is important to ensure that as much work as possible is done at the lab bench to save both the cost and any unnecessary suffering of the animal subjects.

5.5 Conclusion

This chapter builds on the work presented in the previous sections. The positive MSC proliferation shown previously in two dimensions were replicated in the 3D environment. This addresses one of the key objectives of this thesis; whatever topography is used to increase cell proliferation, it must be able to be incorporated into the manufacturing process of the full scaffold. This was shown to be the case with the novel formulations used here.

Furthermore, these data present strong justification for the novel HA+5wt% alumina scaffold to be taken forward to an *in vivo* trial. The scaffold outperformed the industry standard Bio-Oss in every test implemented. MSC activity was an order of magnitude higher on the HA+5wt% matrix and it displayed a significant reduction in the immune response in both macrophages and dendritic cells.

This project's main objective was to increase cell proliferation on the pore surfaces of a HA scaffold by optimizing its topography. This has been achieved by successful translation of the topography designed and tested in the previous chapters into a 3D environment.

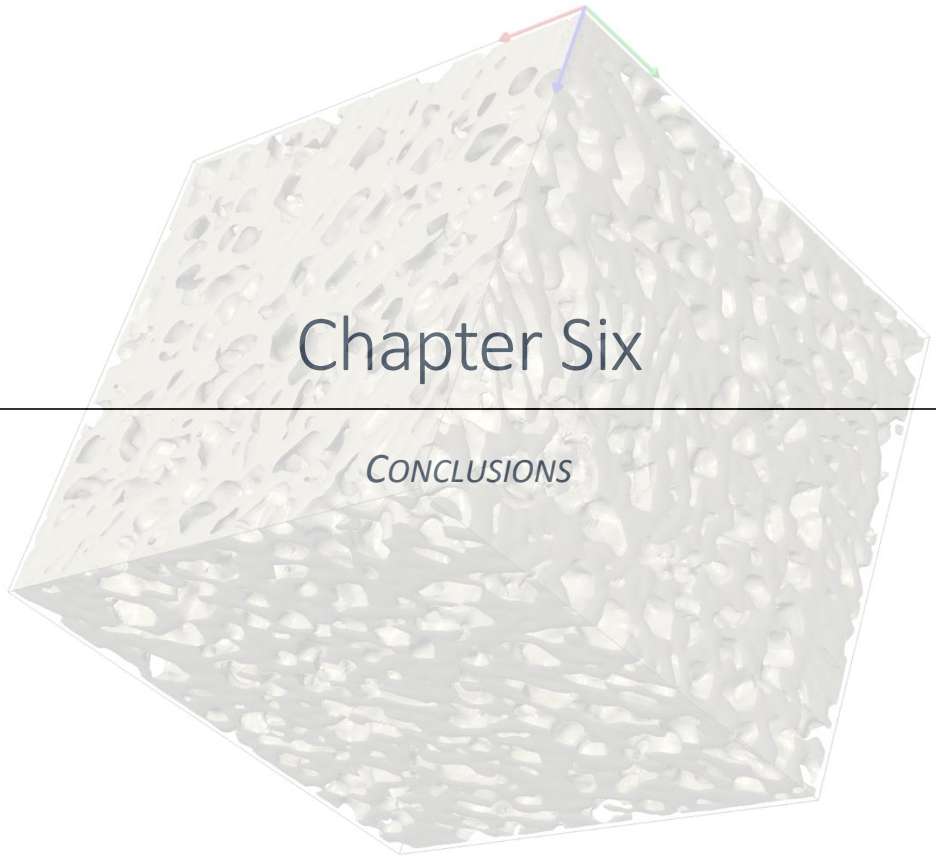

Chapter Six

CONCLUSIONS

6.1 Introduction

The overall project aim was as follows:

Define, produce and evaluate an optimized ceramic scaffold for use in oro-maxillo-facial bone tissue engineering.

Specifically, to achieve this aim, the following objectives were intended:

1. Induce topographical changes in HA scaffolds by
    a. Sintering temperature variation.
    b. Nanophase addition.
2. Develop a method for quantifying surface topography in a manner relevant to cell behaviour.
3. Monitor phase stability.
4. Assess surface performance using cell activity and thus determine the effectiveness of surface topography as a method of enhancing cell proliferation on HA scaffolds.
5. Compare the optimized scaffold to an industry competitor using the metrics of cell activity and inflammatory response.

The chief scaffold feature undergoing optimization was the surface topography of the porous structure. The working hypothesis was that if nanoscale surface features (~100nm-~500nm) could be introduced onto the pore surfaces, they would stimulate cells to proliferate and increase overall bioactivity. This would in turn accelerate the integration of the implant with the host tissue and improve the final healing outcome.

The optimization described above of the original TCBE scaffold was initiated in response to the largely unmet need for alternatives to bone grafting in oro-maxillo-facial procedures. The results of this project were critically examined at regular intervals in conjunction with clinicians

from the Dublin Dental Hospital. This focussed the laboratory efforts on the key features and outcomes of the scaffold relevant to the oro-maxillo-facial clinical experience. The ensuing scaffold is one that meets the requirements of a ready-to-use, malleable, self-supporting and bioactive construct. It Is believed to be of direct commercial applicability.

This chapter focusses on the how the various studies undertaken in this work fit together to address the proposed aim. In doing so, various research objectives were under scrutiny. To clarify this, the particular research objective under discussion is included as a subheading in each section here.

6.2 Sintering Temperature

Aim: Inducing Topographical Changes in HA Scaffolds

Sintering temperature was the first method of altering the scaffolds' surface topography examined in this work. In terms of being a controllable engineering parameter it has several advantages. Altering it adds nothing to the cost, complexity or manufacturing time of a scaffold. Sintering was already an integral part of the TCBE scaffold manufacturing process [4] and so changing it required no additional steps in the protocol.

The morphologies resulting from varying the sintering temperature of the surfaces from 1100-1350°C were diverse (Figure 3.2). The low temperature substrates initially appeared very promising as they seemed to provide a topography to which cells would be responsive; feature sizes were on average 500nm. This fit with what the literature reported as being an appropriate feature size to stimulate cellular response. However, apparently contradictory results were observed here. Cells seeded on the smoother, high temperature surfaces (>1200°C) adhered and proliferated well; statistically the cell responses to these surfaces were indistinct from the response to the tissue culture plastic control (Figure 3.6). Conversely, wholesale cell death

occurred on the low temperature surfaces (<=1200°C). It was noted that this death occurred from the very outset of the culture period. Thus it was concluded that it was not a negative effect on proliferation that was being observed but a negative effect on adherence.

6.3 Surface Quantification

Aim: Developing a Method for Quantifying Surface Topography in a Manner Relevant to Cell Behaviour

The MSC aversion to the nanotopographically featured surfaces produced by low sintering temperatures led to another problem. How to quantitatively define those surfaces. This was necessary to allow the design of further surfaces that avoided the same adhesion problems. Furthermore, it related to the wider issue of the ambiguity in the literature on the same subject.

The most common surface topography descriptors, R_a, R_q, S_a, S_q and S_{dr}, revealed no trend when applied to the sintered morphologies (Table 3.2). This was despite the very obvious and continuous change of morphologies, apparent from the SEM images, as sintering temperature increased. This in itself calls into question the widespread use of these basic factors to describe tissue engineering topography in the literature.

It will be noted that all of the surface descriptors mentioned above rely on deviations in the Z-direction of an XYZ Cartesian system. Even the three dimensional parameters, S_a, S_q and S_{dr}, are merely aggregates of the height deviations of profiles taken across the surface. This leads to a very simplistic view of a surface; one where the primary factor is changes in height of the topography. However, it would be reasonable to assume that the rate at which the height of the topography changed would also be important.It was this line of thought that lead to the implementation of the surface wavelength parameter, λ, in this work. It combines both the height

deviations and the average slope of a line profile of the surface into a single parameter. This allows an indication of the spatial distribution of peaks across the profile.

This parameter revealed a significant trend in the surfaces; surfaces with shorter wavelengths were produced at lower sintering temperatures while longer wavelength surfaces occurred at higher temperatures. Furthermore, there proved to be a strong correlation between cellular response to a sample and the surface wavelength of that sample (Figure 3.8). This proves that surface wavelength is an excellent predictor of cell survival after seeding on the sintered substrates.

This result, combined with the rapid cell death apparent on the low temperature surfaces, led to the conclusion that there exists a threshold surface wavelength (~2.4µm), below which cells cannot adhere. Therefore, when designing a novel topography, the first feature to be included must be a basal layer of sufficient wavelength to allow for cellular adhesion and further proliferation. In the context of this work, 1300°C and 1350°C produced the highest surface wavelengths (~2.65µm) and the best cell responses. It was decided to retain the sintering temperature of 1350°C for further optimization as this was the temperature originally proposed by Buckley *et al.* [4] and it appeared to be the most mechanically stable.

6.4 Nanophase Addition

Aim: Inducing Topographical Changes in HA Scaffolds

The correlation of surface wavelength with cell response observed in Chapter 3 resulted in a target design for a surface optimized for both cellular adhesion and proliferation. It would consist of an underlying basal layer made up of the original HA matrix that proved so conducive to cellular adhesion. Nanoscale topographical features embedded into this layer could then provide a stimulus for cellular proliferation. The general approach to achieving this design was phase

addition. Specifically, a nanopowder of a material with a higher sintering temperature than HA was added to the HA surface, forming distinct topographical features. Alumina was chosen due to its high sintering temperature and proven biocompatibility.

The addition of the nanophase alumina to the HA precursor proved extremely effective. Regular, distinct and nanoscale topographical features arising from the alumina nanoparticles were clearly apparent on the HA surface (Figures 4.2 and 4.3(A)). This morphology closely matched the target surface design. Furthermore, quantified topographical data from white-light interferometry measurements showed that the underlying basal layer of the surface, formed from the sintered HA, had surface wavelengths in the range of 2.4-2.65µm, i.e. optimal for cellular adhesion.

6.5 Phase Stability and Surface Chemistry

Aim: Monitor Phase Stability

The literature tends to agree that decomposition of HA to α-TCP starts to occur at sintering temperatures of ~1250°C. However, it has been shown here that the Sigma-Aldrich brand of HA used throughout this project is phase stable to 1350°C. This is not the case for all commercial HA products (see Appendix I). The XRD data presented in Chapter 3 showed almost no phase decomposition as the temperature was increased from 1100-1350°C (Figure 3.5). Only very faint evidence of α-TCP was observed at the higher temperatures. Thus, it was concluded that any difference in cell behaviour observed on the surfaces was attributable to their differing topographies.

The situation became a little more complex once alumina was added to the system (Chapter 4). Although the pure HA was phase stable to 1350°C, increasing quantities of alumina added to it caused a corresponding increase in decomposition to α-TCP (Figure 4.6). The rise was

steady from pure HA at 1wt% alumina to pure α-TCP at 10wt% alumina. It is believed that the alumina nanoparticles act as nucleation sites for phase change of the HA to α-TCP.

This idea of the alumina nanoparticles being nucleation points is given further credence by the EDX analysis in Chapter 4 (Figure 4.5). This analysis proved that the alumina particles were the source of the nanoscale topographical features by revealing high concentrations of aluminium in locations corresponding to the nanoparticles. It also showed that diffusion of calcium ions was occurring into the particles from the surrounding calcium phosphate. It is believed that these free calcium ions originated from the decomposition of the HA to α-TCP.

The diffusion of calcium from the decomposing HA into the alumina also suggests a reaction taking place between the two species. No evidence of alumina can be found in the XRD data. Additionally, no evidence of any other phase is apparent either; apart from the well-documented HA and α-TCP phases. Reactions in the calcium phosphate – alumina system have been described before and the products tend to be various calcium aluminates [51]. Finding empirical evidence of these is difficult. However, it was done by the Viswanath group [51] by dissolving the calcium phosphate/alumina composite in HCL, filtering the solution and running XRD analysis on the filtrate. The calcium aluminates, being insoluble in HCL, then become apparent in the resulting diffractogram. This shows that it is the calcium phosphate peaks that are hiding the relatively weak signals of the calcium aluminates in the composite diffractograms as was suggested in Chapter 4. Hence, the conclusion drawn here is that the same reaction has occurred between the calcium and alumina with various calcium aluminates being the products. It is worth bearing in mind that calcium aluminates are biocompatible and have widespread clinical use in dental cements.

6.6 Surface Performance – Cellular Response

Aim: Assess Surface Performance Using Cell Activity and Thus Determine the Effectiveness of Surface Topography as a Method of Enhancing Cell Proliferation on HA Scaffolds

The addition of the alumina nanoparticles allowed the novel topography that was the aim of this work to be realised. The cell response to this morphology was exceptional (Figure 4.8). Additions of between 2-10wt% alumina proved capable of increasing MSC proliferation on the surfaces by up to 261.5% over pure HA and 447% over the tissue culture plastic control. Longitudinally, these increases manifested themselves as an accelerated initial proliferation stage over the first two weeks of culture. This was followed by a sustained plateau of high metabolic activity right to the end of the culture period (day 32) completely unmatched by either pure HA or control. This result is the cornerstone of this project. It proves that tailored surface topography can positively and significantly affect cellular proliferation rates on tissue engineering scaffolds. Moreover, these improvements can be provided by inexpensive, biocompatible materials combined in a way that is simple and scalable to industry. Figures 6.1 and 6.2 are He-ion images giving visual confirmation of MSCs adhering and proliferating on HA+5wt% alumina surfaces.

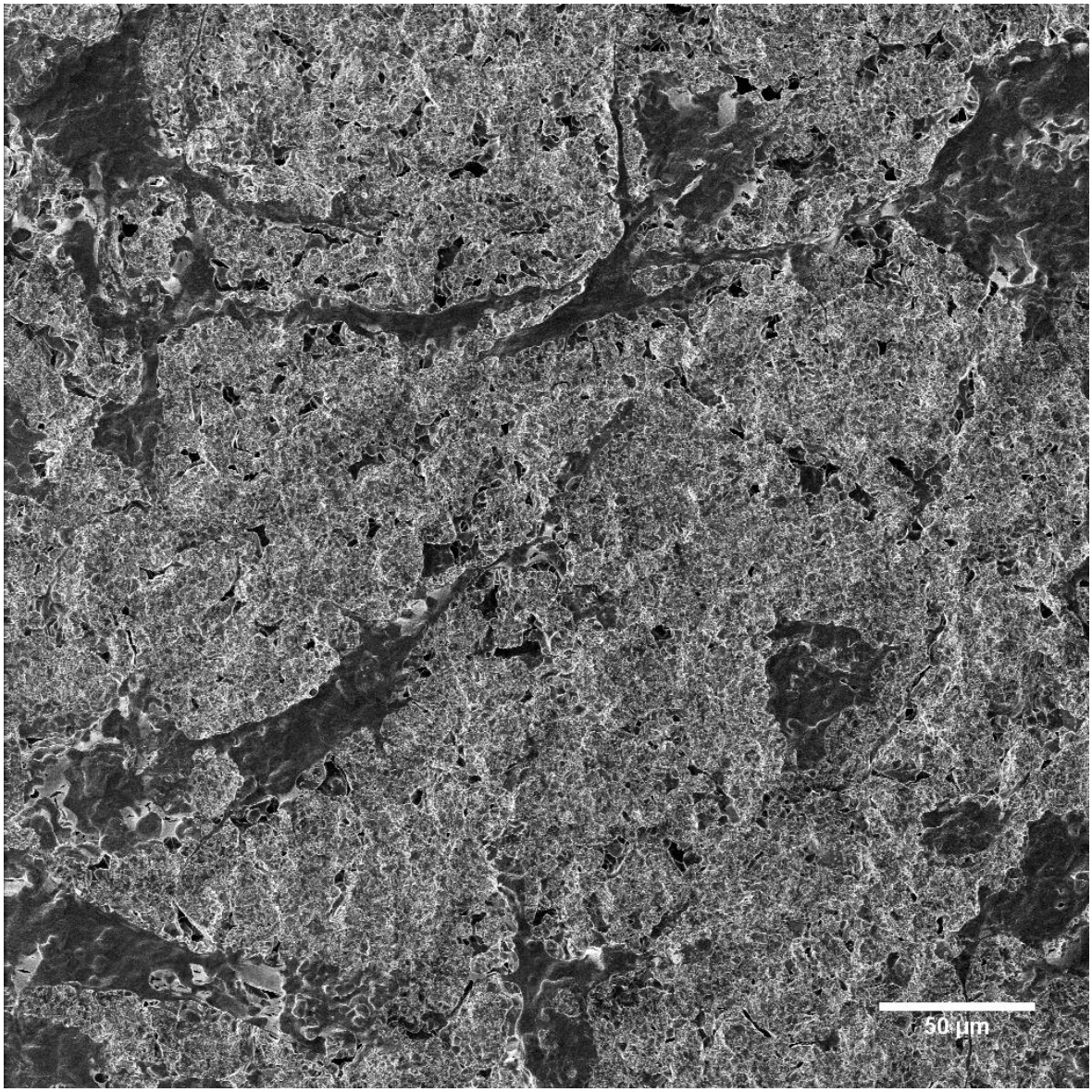

Figure 6.1. *He-ion image of MSCs proliferating on a HA+5wt% alumina substrate. Scale bar is 50µm.*

One of the more puzzling results observed in this project was the cell response to surfaces with higher alumina contents (>10wt%). A sudden drop in cell activity was observed as the alumina concentration crossed the 10-12wt% threshold. These surfaces induced the lowest metabolic response of all those tested including pure HA. This was unexpected as no difference in surface topography could be discerned across this threshold, yet the positive effects of the alumina nanoscale features were suddenly no longer apparent.

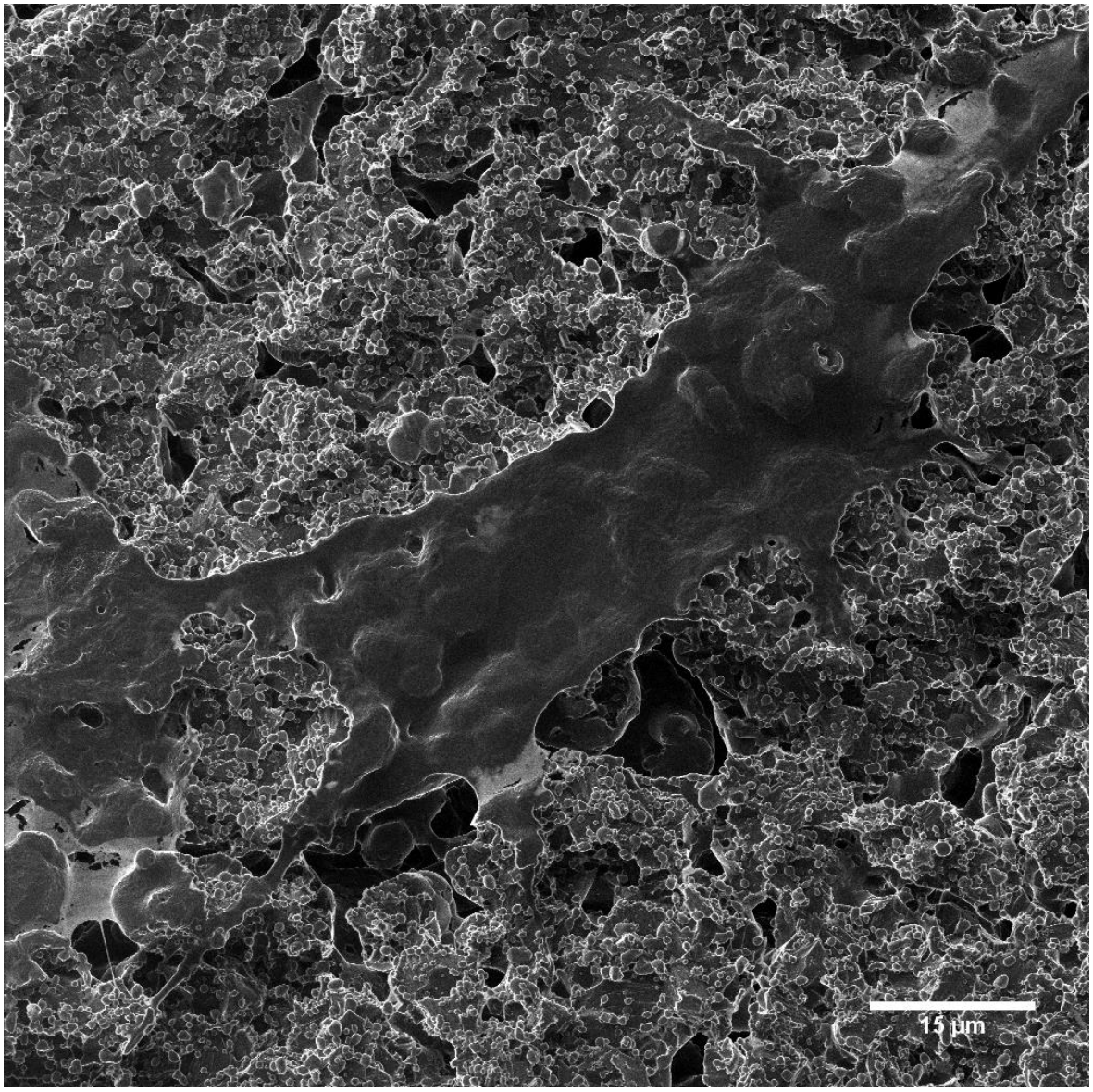

Figure 6.2. *Close-up He-ion image of an MSC adhering to a HA+5wt% surface. Scale bar is 15µm.*

It is important to note that the low cell response to the high alumina samples manifested differently to that observed on the low-temperature sintered surfaces. In the latter case, no cell life at all was apparent (Figure 3.6). This led to the conclusion about cellular adhesion and the necessity for a long surface wavelength (>2.4µm) to allow this. With the high alumina surfaces, cell viability was still observable but it was extremely depressed and exhibited a general downward trend across the 32 days of culture.

The XRD and EDX results showed no sign of a third phase i.e. an unintended cytotoxic compound that would account for the poor performance of the >10wt% alumina surfaces. The literature is also clear that all of the phases that are present in this HA+alumina system are biocompatible; namely hydroxyapatite, α-tri-calcium phosphate, calcium oxide, alumina and calcium aluminate.

It was next hypothesized that ionic dissolution from the high alumina substrates was causing the negative cell responses. There is an interest in the biochemical literature in the link between calcium and apoptosis or programmed cell death. Essentially, it has been shown that calcium concentrations above a certain threshold can cause apoptotic signals to be produced in otherwise healthy cells [91]. The EDX data presented in Chapter 4 showed that calcium was diffusing from the calcium phosphate regions into the alumina regions. Therefore, the question was if, in the high alumina samples, it was also diffusing into the media and becoming available to the MSCs. The calcium assay data (Figure 4.11) proved that this was not the case.

The next hypothesis to be tested was particulate dissolution. It was noted during manufacturing that the high alumina samples tended to be less mechanically stable than their low alumina counterparts. It was thought that this might lead to particulate dissociation from the bulk during culture. The effect of particulate debris on bone-type cells has been the focus of a lot of research due to the tendency of bone prostheses to produce wear particles over time. There is a lot of variation in the data due to the myriad of contributing factors including particle chemistry, size, shape and crystallinity. However, it is clear that in certain cases particulate debris can have a negative effect on proliferating cells [94]. Principally when being phagocytosed or engulfed by cells. Image analysis was employed here to deduce if high alumina samples produced more debris than others.

It was shown that the HA+14wt% alumina disks produced twice as many particles as either HA+6wt% alumina or pure HA (Figure 4.13(A)) and this was seen as a probable cause of the

negative cell response. Having ruled out any other chemical phase or ion dissolution as explanations for the poor cell response to the high alumina samples, a high number of debris particulates remains the most likely reason. It is suggested that cells are phagocytosing particles dissociating from the bulk material. The subsequent effects would then be two-fold; first the cells would naturally stop proliferating to perform the phagocytosis, and second many of the cells would die if unable to break down the particle internally. This would account for both the lack of proliferation apparent in the data and also for the downward trend in cell activity. Similar effects have been observed in human MSCs in response to titanium wear particles [107]. Here the authors suggest that the inhibition of cellular functions is caused by disruption of the cytoskeleton by the particulates.

The same image analysis also revealed another interesting trend. The particles produced by the HA+14wt% alumina samples tended to be nearly twice as large as those dissociating from the HA+6wt% alumina and pure HA disks (Figure 4.13(B)). This suggests a significant disintegration of the surfaces of the 14wt% disks. As a result, although initial adhesion is not affected, in the long-term cells may find it difficult to adhere to the surface. Once removed by the dissociative tendency of the substrate, these MSCs would die in suspension. This dissociative behaviour might also be exacerbated by the mechanical action of the cells on the surface. It may be that the low and decreasing cell response to the high alumina surfaces is a combination of the two phenomena; phagocytosis of particulate debris and surface instability leading to long-term adhesion challenges.

6.7 Comparisons with an Established Industry Competitor

Aim: Compare the Optimized Scaffold to an Industry Competitor Using the Metrics of Cell Activity and Inflammatory Response

The novel HA+alumina topography translated well to the full 3D scaffold constructs. This was aided primarily by the simplicity of the phase addition protocol. The addition of the nanopowder occurs before any of the major scaffold manufacturing procedures. It thus effects only the surface topography of the porous structure and requires no additional post-processing steps. This was highlighted as being a key requirement in Chapter 2.

The results seen on the 2D disks were also replicated on the 3D scaffolds. HA+5wt% alumina constructs induced up to 157% of the cell activity of pure HA scaffolds. However, in this project, the key performance indicators of the novel, optimised scaffold (HA+5wt% alumina) were comparisons made with an industry standard bone grafting product; Geistlich Bio-Oss®. Bio-Oss is a decellularized bovine bone scaffold and was suggested as the comparator for this project by dental surgeons in the Dublin Dental Hospital due to its widespread clinical use and positive results.

The results of the comparison were outstanding (Figures 5.5 and 5.6). In both block and granule form, HA+5% alumina scaffolds induced nearly ten times as much proliferative activity in the MSCs as on Bio-Oss samples. This was the first indicator that the novel topography improved the outcomes of cells over not just the original 100% HA TCBE scaffold but also a market leading, FDA approved commercial product.

As highlighted in Chapter 2, inflammation is a physiological process that can have significant ramifications for any implanted biomaterial but is often overlooked by researchers. Here, experiments were run to test the inflammatory response of both Bio-Oss and various HA+alumina scaffold formulations (Figures 5.8 and 5.9). It was found that the novel scaffold

formulations induced significantly less production of the inflammatory cytokine IL-1β in immune cells than Bio-Oss. This was true for pure HA and HA+1-10wt% alumina. An implanted scaffold that is capable of inducing minimal inflammation could prove to be of great benefit to the clinical community, offering quicker integration times and fewer post-operative complications. This is especially exciting when coupled with the accelerated MSC proliferation provided by the novel topography.

6.8 Further Research

6.8.1 *In Vivo* Study

It is imperative, both from an ethical and cost-benefit point of view, that before any animal trial of a novel scaffold can take place, all possible *in vitro* analysis is done. These *in vitro* studies were the focus of this project and what resulted is a scaffold that has a novel surface topography fully optimized to increase cellular proliferation. The next stage of evaluation in the design cycle of the scaffold must be a set of *in vivo* animal trials. Only then can the construct be finally deemed commercially viable. It is also an essential intermediate step before subsequent human trials can be approached. Human trials are necessary for FDA and EU approval, before a new therapy can be commercially realised.

The form that the *in vivo* trials take is open to debate but from an oro-maxillo-facial perspective, the best model for the human jaw appears to be canine. This model is expensive however, and a pilot trial in rabbits would probably need to precede it. Depending on the success of these trials, three outcomes are possible. One, the scaffold does not live up to its laboratory promise, this would require a failure analysis and possible redesign. Two, the trials are inconclusive, this could either result in further animal study or *in vitro* work. Three, the trials are a

success, proving the novel scaffold superior to the available commercial products. In this case, further funding may then be sought to pursue a human trial.

In any event, there are large ethical and financial issues surrounding animal work and rightly so. To avoid unnecessary pain to any animal and also wasted research funding, it is absolutely necessary that every possible avenue of enquiry is pursued in the laboratory first. This was achieved by this project.

6.8.2 Further Material Analysis

Every effort was made to fully characterise the materials used in this project with the tools and expertise available. However some questions still remain, primarily concerning the potential reaction between calcium and alumina in the HA+alumina system. The literature indicates that calcium aluminates are the only likely products of any such reaction. But empirical verification of this fact is still desirable.

A first pass might be attempted by following the protocol laid out by Viswanath *et al.* [51]. Dissolving the materials in hydrochloric acid and filtering the solutions, leaving behind the insoluble calcium aluminates which can then be defined. This approach was not attempted as part of this work due to time constraints and it also comes with the obvious weakness of not being able to analyse any unknown soluble components. Still, it is worth considering before going further afield in search of an answer.

The phases known to be present in the system also present some interesting avenues for exploration. As has been shown, increasing the alumina content in the HA+alumina system, in turn accelerates the decomposition of HA to α-TCP. It is accepted that α-TCP dissolves and resorbs faster than HA. This phenomenon is worth investigating *in vitro*, particularly if the alumina content is to be used as a control for the HA to α-TCP ratio and, thus, the resorption rate of the

implanted scaffold. Carefully maintained, longitudinal dissolution tests in simulated body fluid may fully characterise this effect.

6.8.3 Biochemical Study of Cell Death

Some of the most interesting results presented in this work were the poor cell responses to high alumina content surfaces. The relatively sudden change from positive responses to negative was unexpected as dose-dependent reactions are more common in cell biology.

The theory that particulate debris is having an adverse effect on cell viability is a good one, and well supported by the literature [94], [107]. However, to fully understand what is occurring on an intra-cellular level in response to the high alumina surfaces, a full biochemical analysis of the signals and cytokines being expressed by the cells is probably necessary. Such research goes beyond both the scope and expertise of this project but it would be interesting to learn the exact mechanism by which the cells are dying; be it apoptosis, programmed cell death; necrosis, self-digestion or some other, as yet undetermined route. To this end, collaboration with a biochemical laboratory would be a good approach.

6.8.4 Further Study of Inflammatory Response

Another potentially fruitful source of collaboration would be with an immunology group to further investigate the positive effect that the novel scaffolds have on inflammation. The discrepancy between the responses produced by the novel formulations and Bio-Oss further strengthen the case that this is something that should be looked at in more detail by researchers in implantable biomaterials.

The inflammation results presented in this work are really only a metric of comparison between the novel HA+alumina scaffold and the commercial product Bio-Oss. Many questions

remain such as why the difference exists between the novel scaffolds and Bio-Oss, what effect would such inflammation levels have on surrounding bone and what cellular pathways are being activated by these materials. This last question ties in with the cell death question mentioned above. *In vivo*, inflammation and cellular apoptosis are often intrinsically linked, and so it is important that these questions are not viewed in isolation.

6.8.5 Functionally Graded Constructs

The reduction/elimination of core necrosis was one of the key drivers behind the project aim of increasing cellular proliferation on the surfaces of tissue engineering scaffolds. The fact that topography can now be tailored to deliver the sorts of benefits shown in this work will go a long way towards alleviating the core necrosis problem. However, it is possible that this is not the end of the story. It was mentioned in Chapter 2 that pore occlusion by proliferating cells in the outer regions of a scaffold can reduce the fluid transport capabilities of the matrix and, thus, exacerbate the necrotic core. It is conceivable that this problem might be made worse by a surface topography that actively encouraged cellular proliferation at the scaffold edges.

An interesting avenue of exploration may therefore be a scaffold whose topography is functionally graded from the outer edges to the core. An example might be a scaffold with a HA+5wt% alumina core to stimulate proliferation and a pure HA outer region to facilitate cell adhesion and movement into the inner regions of the construct. The ALP assay results presented in Chapter 5 also show that an outer, pure HA layer would accelerate osteogenesis in those regions. This would accelerate the integration of the scaffold with the host tissue. It is likely that *in vivo* trials would be required to accurately compare this theoretical bilayer design with the formulations described by this project.

It is also possible that increased cellular proliferation at the outer edges of the scaffold would not be a negative characteristic. Necrotic cores are often associated with constructs that

have had cells seeded directly into their interiors, followed by culture in a bioreactor system. A more natural therapeutic progression might be implantation of a dry construct of the type described in this work. Recruitment of progenitor cells from the surrounding tissue would naturally follow and the tailored topography would increase their proliferation. It is envisioned that the outer edges of the scaffold would then integrate with the host bone quicker than was previously possible, before the cells move further into the interior. This would make any potential necrotic core irrelevant as cells would only reach the scaffold interior when they could be supported by the surrounding tissue.

6.9 Conclusion

The overall project aim of defining, producing and optimizing a ceramic scaffold for use in oro-maxillo-facial bone tissue engineering has been achieved. In so doing, an improved standard for quantification of tissue engineering surfaces is suggested; the surface wavelength, λ. This was found to correlate strongly with cellular adhesion and provided a threshold value, below which adhesion proved impossible. Using this parameter, a novel topography was designed with two distinct features. The first, a basal layer of hydroxyapatite with surface wavelength ~2.65µm which was deemed optimum for providing adhesion sites for cells. The second, nanoscale topographical features formed by adding alumina to the hydroxyapatite precursor powder. These provided the additional stimulus to increase mesenchymal stem cell proliferation by up to 261.5% over pure HA alone in two-dimensional disks.

This result translated to full three dimensional scaffolds which displayed ten times the mesenchymal stem cell proliferation of an industry leading scaffold Bio-Oss. Furthermore, the novel scaffold produced significantly less inflammatory response in both macrophages and

dendritic cells than Bio-Oss. This demonstrates a proven *in vitro* viability for the new construct and paves the way for full scale *in vivo* trials.

Bibliography

[1] A. A. Jahangir, R. M. Nunley, S. Mehta, and A. Sharan, “Bone-graft substitutes in orthopaedic surgery,” *AAOS Now*, vol. 7, no. 6, pp. 5–9, 2013.

[2] M. A. Velasco, C. A. Narváez-Tovar, and D. A. Garzón-Alvarado, “Design, Materials, and Mechanobiology of Biodegradable Scaffolds for Bone Tissue Engineering,” vol. 2015, 2015.

[3] C. T. Buckley, “On the Development of Scaffolds for Bone Tissue Engineering,” University of Dublin, Trinity College, 2007.

[4] C. T. Buckley and K. U. O’Kelly, “Fabrication and characterization of a porous multidomain hydroxyapatite scaffold for bone tissue engineering investigations.,” *J. Biomed. Mater.*, vol. 93, no. 2, pp. 459–67, May 2010.

[5] X. Wang, J. S. Nyman, X. Dong, H. Leng, and M. Reyes, *Fundamental Biomechanics in Bone Tissue Engineering*. Morgan & Claypool, 2010.

[6] J. D. Currey, *Bones: Structure and Mechanics*. 2002.

[7] S. Weiner and H. D. Wagner, “THE MATERIAL BONE: Structure-Mechanical Function Relations,” *Annu. Rev. Mater. Sci.*, vol. 28, no. 1, pp. 271–298, Aug. 1998.

[8] E. A. Zimmerman, M. E. Launey, and R. O. Ritchie, “Berkeley Lab, Ritchie Group,” 2012. [Online]. Available: http://www.lbl.gov/ritchie/Programs/BIO/MixedModeFracture.htm. [Accessed: 30-Jul-2013].

[9] P. Zhang, K. Hamamura, and H. Yokota, “A Brief Review of Bone Adaptation to Unloading,” *Genomics. Proteomics Bioinformatics*, vol. 6, no. 1, pp. 4–7, 2008.

[10] L. Hammarstrom and S. Lindskog, “General morphological aspects of resorption of teeth and alveolar bone.,” *Int. Endod. J.*, vol. 18, no. 2, pp. 93–108, Apr. 1985.

[11] S. Hansson and A. Halldin, “Alveolar ridge resorption after tooth extraction: A consequence of a fundamental principle of bone physiology,” *J. Dent. Biomech.*, vol. 3, pp. 1–8, 2012.

[12] T. Thalmair, S. Fickl, D. Schneider, M. Hinze, and H. Wachtel, “Dimensional alterations of extraction sites after different alveolar ridge preservation techniques - a volumetric study.,” *J. Clin. Periodontol.*, vol. 40, no. 7, pp. 721–7, Jul. 2013.

[13] F. G. Draenert, D. Huetzen, A. Neff, and W. E. G. Mueller, “Vertical bone augmentation procedures: Basics and techniques in dental implantology,” *J. Biomed. Mater. Res. Part A*, pp. 6–8, 2013.

[14] M. Clementini, a Morlupi, C. Agrestini, and L. Ottria, “Success rate of dental implants inserted in autologous bone graft regenerated areas: a systematic review.,” *Oral Implantol. (Rome).*, vol. 4, no. 3–4, pp. 3–10, Jul. 2011.

[15] E. Nyström, J. Ahlqvist, P. E. Legrell, and K. E. Kahnberg, “Bone graft remodelling and implant success rate in the treatment of the severely resorbed maxilla: a 5-year longitudinal study.,” *Int. J. Oral Maxillofac. Surg.*, vol. 31, no. 2, pp. 158–64, Apr. 2002.

[16] J. R. Porter, T. T. Ruckh, and K. C. Popat, “Bone tissue engineering: a review in bone biomimetics and drug delivery strategies.,” *Biotechnol. Prog.*, vol. 25, no. 6, pp. 1539–60, 2009.

[17] J. Folkman and M. Hochberg, “Self-regulation of growth in three dimensions,” *J. Exp. Med.*, vol. 138, pp. 745–753, 1973.

[18] K. Lee, S. Wang, M. J. Yaszemski, and L. Lu, “Enhanced Cell Ingrowth and Proliferation through Three-Dimensional Nanocomposite Scaffolds with Controlled Pore Structures,” *Biomacromolecules*, vol. 11, no. 3, pp. 682–689, 2010.

[19] C. M. Murphy and F. J. O’Brien, “Understanding the effect of mean pore size on cell activity in collagen-glycosaminoglycan scaffolds,” *Cell Adh. Migr.*, vol. 4, no. 3, pp. 377–381, Jul. 2010.

[20] S. Li, J.-L. Guan, and S. Chien, “Biochemistry and biomechanics of cell motility.,” *Annu. Rev. Biomed. Eng.*, vol. 7, pp. 105–150, Jan. 2005.

[21] Y. M. Kolambkar, M. Bajin, A. Wojtowicz, D. W. Hutmacher, A. J. García, and R. E. Guldberg, “Nanofiber Orientation and Surface Functionalization Modulate Human Mesenchymal Stem Cell Behavior In Vitro,” *Tissue Eng. Part A*, vol. 20, no. 1–2, pp. 398–409, 2014.

[22] E. Lamers, R. van Horssen, J. te Riet, F. C. M. J. M. van Delft, R. Luttge, X. F. Walboomers, and J. A. Jansen, “The influence of nanoscale topographical cues on initial osteoblast morphology and migration.,” *Eur. Cell. Mater.*, vol. 20, pp. 329–43, Jan. 2010.

[23] L. S. Gardel, C. Correia-Gomes, L. A. Serra, M. E. Gomes, and R. L. Reis, “A novel bidirectional continuous perfusion bioreactor for the culture of large-sized bone tissue-engineered constructs.,” *J. Biomed. Mater. Res. Part B Appl. Biomater.*, pp. 1–10, May 2013.

[24] D. A. Gaspar, V. Gomide, and F. J. Monteiro, “The role of perfusion bioreactors in bone tissue engineering.,” *Biomatter*, vol. 2, no. 4, pp. 167–75, 2012.

[25] L. Bjerre, C. Bünger, A. Baatrup, M. Kassem, and T. Mygind, “Flow perfusion culture of human mesenchymal stem cells on coralline hydroxyapatite scaffolds with various pore sizes.,” *J. Biomed. Mater.*, vol. 97, no. 3, pp. 251–63, Jun. 2011.

[26] D. A. Brown, *The Effects of Mass Transport Limitations on Cell Metabolism and Viability in a Diffusion-limited Model of Engineered Heart Tissue*. 2008.

[27] A. J. Vander, J. H. Shermann, and D. S. Luciano, *Human Physiology*. New York: McGraw-Hill, 1985.

[28] H. Huang, C. Ho, T. Lee, T. Lee, K. Liao, and F. Chen, “Effect of surface roughness of ground titanium on initial cell adhesion,” *Biomol. Eng.*, vol. 21, pp. 93–97, 2004.

[29] M. J. Dalby, N. Gadegaard, R. Tare, A. Andar, M. O. Riehle, P. Herzyk, C. D. W. Wilkinson, and R. O. C. Oreffo, “The control of human mesenchymal cell differentiation using nanoscale symmetry and disorder.,” *Nat. Mater.*, vol. 6, no. 12, pp. 997–1003, Dec. 2007.

[30] S. Watari, K. Hayashi, J. A. Wood, P. Russell, P. F. Nealey, C. J. Murphy, and D. C. Genetos, “Modulation of osteogenic differentiation in hMSCs cells by submicron topographically-patterned ridges and grooves.,” *Biomaterials*, pp. 1–9, Oct. 2011.

[31] J. M. Łopacińska, C. Grădinaru, R. Wierzbicki, C. Købler, M. S. Schmidt, M. T. Madsen, M. Skolimowski, M. Dufva, H. Flyvbjerg, and K. Mølhave, “Cell motility, morphology, viability and proliferation in response to nanotopography on silicon black.,” *Nanoscale*, vol. 4, no. 12, pp. 3739–45, Jun. 2012.

[32] A. Helth, P. F. Gostin, S. Oswald, H. Wendrock, U. Wolff, U. Hempel, S. Arnhold, M. Calin, J. Eckert, and A. Gebert, “Chemical nanoroughening of Ti40Nb surfaces and its effect on human mesenchymal stromal cell response.,” *J. Biomed. Mater. Res. Part B Appl. Biomater.*, pp. 1–11, Jul. 2013.

[33] K. Anselme, P. Linez, M. Bigerelle, D. Le Maguer, A. Le Maguer, P. Hardouin, H. F. Hildebrand, A. Iost, and J. M. Leroy, “The relative influence of the topography and chemistry of TiAl6V4 surfaces on osteoblastic cell behaviour,” *Biomaterials*, vol. 21, pp. 1567–1577, 2000.

[34] P. M. Tsimbouri, K. Murawski, G. Hamilton, P. Herzyk, R. O. C. Oreffo, N. Gadegaard, and M. J. Dalby, “A genomics approach in determining nanotopographical effects on MSC phenotype.,” *Biomaterials*, vol. 34, no. 9, pp. 2177–84, Mar. 2013.

[35] L. Xia, B. Feng, and P. Wang, “In vitro and in vivo studies of surface-structured implants for bone formation,” *Int. J. Nanomedicine*, no. 7, pp. 4873–4881, 2012.

[36] B. Altmann, R.-J. Kohal, T. Steinberg, P. Tomakidi, M. Bachle-Haas, A. Wennerberg, and W. Att, “Titanium- and Zirconia-Based Implant Materials Are Modulated by Surface Topography,” *Tissue Eng. Part C Methods*, vol. 19, no. 11, pp. 1–14, 2013.

[37] M. Vandrovcova, J. Hanus, M. Drabik, O. Kylian, H. Biederman, V. Lisa, and L. Bacakova, “Effect of different surface nanoroughness of titanium dioxide films on the growth of human osteoblast-like MG63 cells,” *J. Biomed. Mater. Res. Part A*, pp. 1016–1032, 2012.

[38] L. Guo, M. Huang, and X. Zhang, “Effects of sintering temperature on structure of hydroxyapatite studied with Rietveld method,” *J. Mater. Sci. Mater. Med.*, vol. 14, pp. 817–822, 2003.

[39] M. Rouahi, E. Champion, O. Gallet, a. Jada, and K. Anselme, “Physico-chemical characteristics and protein adsorption potential of hydroxyapatite particles: Influence on in vitro biocompatibility of ceramics after sintering,” *Colloids Surfaces B Biointerfaces*, vol. 47, pp. 10–19, 2006.

[40] A. J. Dulgar-Tulloch, R. Bizios, and R. W. Siegel, “Human mesenchymal stem cell adhesion and proliferation in response to ceramic chemistry and nanoscale topography.,” *J. Biomed. Mater. Res. Part A*, vol. 90, no. 2, pp. 586–94, Aug. 2009.

[41] T. J. Webster, R. W. Siegel, and R. Bizios, “Osteoblast adhesion on nanophase ceramics,” *Biomaterials*, vol. 20, pp. 1221–1227, 1999.

[42] F. Ben Ayed and J. Bouaziz, “Sintering of tricalcium phosphate–fluorapatite composites with zirconia,” *J. Eur. Ceram. Soc.*, vol. 28, no. 10, pp. 1995–2002, Jan. 2008.

[43] A. Bertoluzza, R. Simoni, A. Tinti, M. Morocutti, V. Ottani, and A. Ruggeri, “Calcium phosphate materials containing alumina: Raman spectroscopical, histological, and ultrastructural study.,” *J. Biomed. Mater. Res.*, vol. 25, no. 1, pp. 23–38, Jan. 1991.

[44] L. M. Epure, S. Dimitrievska, Y. Merhi, and L. H. Yahia, “The effect of varying Al2O3 percentage in hydroxyapatite/Al2O3 composite materials: Morphological , chemical and cytotoxic evaluation,” *J. Biomed. Mater. Res.*, vol. 83A, no. 4, pp. 1009–1023, 2007.

[45] H. Y. Juang and M. H. Hon, “Fabrication and mechanical properties of hydroxyapatite-alumina composites,” *Mater. Sci. Eng. C*, vol. 2, no. 1–2, pp. 77–81, Dec. 1994.

[46] Y.-K. Jun, W. H. Kim, O.-K. Kweon, and S.-H. Hong, “The fabrication and biochemical evaluation of alumina reinforced calcium phosphate porous implants,” *Biomaterials*, vol. 24, no. 21, pp. 3731–3739, Sep. 2003.

[47] R. Ramachandra Rao and T. . Kannan, “Synthesis and sintering of hydroxyapatite–zirconia composites,” *Mater. Sci. Eng. C*, vol. 20, no. 1–2, pp. 187–193, May 2002.

[48] V. V Silva, R. Z. Domingues, and F. S. Lameiras, “Microstructural and mechanical study of zirconia-hydroxyapatite (ZH) composite ceramics for biomedical applications,” *Compos. Sci. Technol.*, vol. 61, no. 2, pp. 301–310, Feb. 2001.

[49] Z. Evis, M. Sato, and T. J. Webster, “Increased osteoblast adhesion on nanograined hydroxyapatite and partially stabilized zirconia composites,” *J. Biomed. Mater. Res.*, vol. 78A, no. 3, pp. 500–507, 2006.

[50] E. Adolfsson, M. Nygren, and L. Hermansson, “Decomposition Mechanisms in Aluminum Oxide – Apatite Systems,” *J. Am. Ceram. Soc.*, vol. 82, no. 10, pp. 2909–2912, 1999.

[51] B. Viswanath and N. Ravishankar, “Interfacial reactions in hydroxyapatite/alumina nanocomposites,” *Scr. Mater.*, vol. 55, no. 10, pp. 863–866, Nov. 2006.

[52] R. B. Zipin, “The height sensitive surface roughness parameters,” *Appl. Surf. Sci.*, vol. 9, no. 1–4, pp. 266–287, 1981.

[53] G. Stachowiak and A. W. Batchelor, *Experimental Methods in Tribology*. Elsevier, 2004.

[54] W. Zhang, Z. Li, Y. Liu, D. Ye, J. Li, L. Xu, B. Wei, X. Zhang, X. Liu, and X. Jiang, “Biofunctionalization of a titanium surface with a nano-sawtooth structure regulates the behavior of rat bone marrow mesenchymal stem cells.,” *Int. J. Nanomedicine*, vol. 7, pp. 4459–72, Jan. 2012.

[55] A. Canabarro, C. G. Paiva, H. T. Ferreira, B. Tholt-de-Vasconcellos, G. De-Deus, R. Prioli, A. B. R. Linhares, G. G. Alves, and J. M. Granjeiro, “Short-Term Response of Human Osteoblast-Like Cells on Titanium Surfaces With Micro- and Nano-Sized Features.,” *Scanning*, vol. 00, no. February, pp. 1–9, Jul. 2012.

[56] V. Borsari, G. Giavaresi, M. Fini, P. Torricelli, A. Salito, R. Chiesa, L. Chiusoli, A. Volpert, L. Rimondini, and R. Giardino, “Physical Characterization of Different-Roughness Titanium Surfaces , With and Without Hydroxyapatite Coating , and Their Effect on Human Osteoblast-Like Cells,” *J. Biomed. Mater. Res. Part B Appl. Biomater.*, vol. 75, no. 2, pp. 359–68, 2005.

[57] H. Ito, H. Sasaki, K. Saito, S. Honma, Y. Yajima, and M. Yoshinari, “Response of osteoblast-like cells to zirconia with different surface topography,” *Dent. Mater. J.*, vol. 32, no. 1, pp. 122–129, 2013.

[58] A. C. Jones, C. H. Arns, D. W. Hutmacher, B. K. Milthorpe, A. P. Sheppard, and M. a Knackstedt, “The correlation of pore morphology, interconnectivity and physical properties of 3D ceramic scaffolds with bone ingrowth.,” *Biomaterials*, vol. 30, no. 7, pp. 1440–51, Mar. 2009.

[59] J. M. Cordell, M. L. Vogl, and A. J. Wagoner Johnson, “The influence of micropore size on the mechanical properties of bulk hydroxyapatite and hydroxyapatite scaffolds.,” *J. Biomed. Mater.*, vol. 2, no. 5, pp. 560–70, Oct. 2009.

[60] Q. Fu, M. N. Rahaman, F. Dogan, and B. S. Bal, “Freeze-cast hydroxyapatite scaffolds for bone tissue engineering applications.,” *J. Biomed. Mater.*, vol. 3, no. 2, p. 025005, Jun. 2008.

[61] A. C. Jones, C. H. Arns, A. P. Sheppard, D. W. Hutmacher, B. K. Milthorpe, and M. a Knackstedt, “Assessment of bone ingrowth into porous biomaterials using MICRO-CT.,” *Biomaterials*, vol. 28, no. 15, pp. 2491–504, May 2007.

[62] B. Otsuki, M. Takemoto, S. Fujibayashi, M. Neo, T. Kokubo, and T. Nakamura, “Pore throat size and connectivity determine bone and tissue ingrowth into porous implants: three-dimensional micro-CT based structural analyses of porous bioactive titanium implants.,” *Biomaterials*, vol. 27, no. 35, pp. 5892–5900, Dec. 2006.

[63] L. Sherwood, *Human Physiology: From Cells to Systems*. Cengage Learning, 2010.

[64] S. J. Liliensiek, J. A. Wood, J. Yong, R. Auerbach, P. F. Nealey, and C. J. Murphy, “Modulation of Human Vascular Endothelial Cell Behaviors by Nanotopographic Cues,” *Biomaterials*, vol. 31, no. 20, pp. 5418–5426, 2010.

[65] B. Dreier, J. Z. Gasiorowski, J. T. Morgan, P. F. Nealey, P. Russell, and C. J. Murphy, “Early responses of vascular endothelial cells to topographic cues.,” *Am. J. Physiol. Cell Physiol.*, May 2013.

[66] S. Trkov, G. Eng, R. di Liddo, P. P. Parnigotto, and G. Vunjak-Novakic, “Micropatterned 3-Dimensional Hydrogel System to Study Human Endothelial-Mesenchymal Stem Cell Interactions,” *J. Tissue Eng. Regen. Med.*, vol. 4, no. 3, pp. 205–215, 2010.

[67] M. Handel, T. R. Hammer, P. Nooeaid, A. R. Boccaccini, and D. Hoefer, “45S5 Bioglass®-based 3D-scaffolds seeded with human adipose tissue-derived stem cells (hASC) induce in vivo vascularisation in the CAM angiogenesis assay,” *Tissue Eng. Part A*, vol. 9 July, pp. 1–27, 2013.

[68] U. Helmrich, N. Di Maggio, S. Güven, E. Groppa, L. Melly, R. D. Largo, M. Heberer, I. Martin, A. Scherberich, and A. Banfi, “Osteogenic graft vascularization and bone resorption by VEGF-expressing human mesenchymal progenitors.,” *Biomaterials*, vol. 34, no. 21, pp. 5025–35, Jul. 2013.

[69] L. A. J. O’Neill, “Immunity’s Early Warning System,” *Sci. Am.*, no. January, pp. 38–45, 2005.

[70] S. J. Hollister and W. L. Murphy, “Scaffold Translation : Barriers Between Concept and Clinic,” *Design*, vol. 7, no. 6, pp. 459–474, 2011.

[71] S. J. Hollister, “Porous scaffold design for tissue engineering,” *Nat. Mater.*, vol. 4, no. 7, pp. 518–524, 2005.

[72] J. D. Kretlow and A. G. Mikos, “Bones to biomaterials and back again--20 years of taking cues from nature to engineer synthetic polymer scaffolds,” *J. Biomed. Mater.*, vol. 98, no. 3, pp. 323–331, Jun. 2011.

[73] P. Lichte, H. C. Pape, T. Pufe, P. Kobbe, and H. Fischer, “Scaffolds for bone healing: Concepts, materials and evidence.,” *Injury*, vol. 42, no. 6, pp. 569–73, Jun. 2011.

[74] H. H. Lu, S. D. Subramony, M. K. Boushell, and X. Zhang, “Tissue engineering strategies for the regeneration of orthopedic interfaces.,” *Ann. Biomed. Eng.*, vol. 38, no. 6, pp. 2142–54, Jun. 2010.

[75] F. Velard, J. Braux, J. Amedee, and P. Laquerriere, “Inflammatory cell response to calcium phosphate biomaterial particles: an overview.,” *Acta Biomater.*, vol. 9, no. 2, pp. 4956–63, Mar. 2013.

[76] S. Tai, J.-Y. Cheng, H. Ishii, S. Akimoto, T. Satoh, K. Yamamoto, T. Nakajima, S. Karaki, E. Suzuki, K. Yamaguchi, and K. Maruyama, “Characterization of beta-tricalcium phosphate as a novel immunomodulator.,” *Int. Immunopharmacol.*, vol. 19, no. 1, pp. 45–51, Mar. 2014.

[77] M. C. Matesanz, M. J. Feito, M. Oñaderra, C. Ramírez-Santillán, C. da Casa, D. Arcos, M. Vallet-Regí, J. M. Rojo, and M. T. Portolés, “Early in vitro response of macrophages and T lymphocytes to nanocrystalline hydroxyapatites.,” *J. Colloid Interface Sci.*, vol. 416, pp. 59–66, Mar. 2014.

[78] P. Laquerriere, A. Grandjean-Laquerriere, S. Addadi-Rebbah, E. Jallot, D. Laurent-Maquin, P. Frayssinet, and M. Guenounou, “MMP-2, MMP-9 and their inhibitors TIMP-2 and TIMP-1 production by human monocytes in vitro in the presence of different forms of hydroxyapatite particles,” *Biomaterials*, vol. 25, no. 13, pp. 2515–2524, Jun. 2004.

[79] P. Laquerriere, A. Grandjean-Laquerriere, M. Guenounou, D. Laurent-Maquin, P. Frayssinet, and M. Nardin, “Correlation between sintering temperature of hydroxyapatite particles and the production of inflammatory cytokines by human monocytes,” *Colloids Surfaces B Biointerfaces*, vol. 30, no. 3, pp. 207–213, Jul. 2003.

[80] A. Grandjean-Laquerriere, O. Tabary, J. Jacquot, D. Richard, P. Frayssinet, M. Guenounou, D. Laurent-Maquin, P. Laquerriere, and S. Gangloff, “Involvement of toll-like receptor 4 in the inflammatory reaction induced by hydroxyapatite particles.,” *Biomaterials*, vol. 28, no. 3, pp. 400–4, Jan. 2007.

[81] A. Polini, D. Pisignano, M. Parodi, R. Quarto, and S. Scaglione, “Osteoinduction of Human Mesenchymal Stem Cells by Bioactive Composite Scaffolds without Supplemental Osteogenic Growth Factors.,” *PLoS One*, vol. 6, no. 10, p. e26211, Jan. 2011.

[82] F. R. Rose, L. a Cyster, D. M. Grant, C. a Scotchford, S. M. Howdle, and K. M. Shakesheff, “In vitro assessment of cell penetration into porous hydroxyapatite scaffolds with a central aligned channel.,” *Biomaterials*, vol. 25, no. 24, pp. 5507–14, Nov. 2004.

[83] A. E. Markaki, “alamarBlue ® Assay for Assessment of Cell Proliferation using the FLUOstar OPTIMA.” 2009.

[84] J. Palomino, A. Martin, M. Camacho, H. Guerra, J. Swings, and F. Portaels, “Resazurin Microtiter Assay Plate : Simple and Inexpensive Method for Detection of Drug Resistance in Mycobacterium tuberculosis,” *Antimicrob. Agents Chemother.*, vol. 46, no. 8, pp. 2720–2722, 2002.

[85] F. Nateche, A. Martin, S. Baraka, J. C. Palomino, S. Khaled, and F. Portaels, “Application of the resazurin microtitre assay for detection of multidrug resistance in Mycobacterium tuberculosis in Algiers.,” *J. Med. Microbiol.*, vol. 55, no. Pt 7, pp. 857–60, Jul. 2006.

[86] E. Magnani and E. Bettini, “Resazurin detection of energy metabolism changes in serum-starved PC12 cells and of neuroprotective agent effect,” *Brain Res. Protoc.*, vol. 5, pp. 266–272, 2000.

[87] G. Pattappa, H. K. Heywood, J. D. de Bruijn, and D. a. Lee, “The metabolism of human mesenchymal stem cells during proliferation and differentiation,” *J. Cell. Physiol.*, vol. 226, no. December, pp. 2562–2570, 2011.

[88] L. Lin, K. L. Chow, and Y. Leng, “Study of hydroxyapatite osteoinductivity with an osteogenic differentiation of mesenchymal stem cells,” *J. Biomed. Mater. Res. - Part A*, vol. 89, pp. 326–335, 2009.

[89] D. Nečas and P. Klapetek, “Gwyddion: an open-source software for SPM data analysis,” *Cent. Eur. J. Phys.*, vol. 10, no. 1, pp. 181–188, Nov. 2011.

[90] H. Y. Yang, I. Thompson, S. F. Yang, X. P. Chi, J. R. G. Evans, and R. J. Cook, “Dissolution characteristics of extrusion freeformed hydroxyapatite- tricalcium phosphate scaffolds,” *J. Mater. Sci. Mater. Med.*, vol. 19, no. 11, pp. 3345–3353, 2008.

[91] S. Orrenius, B. Zhivotovsky, and P. Nicotera, “Regulation of cell death: the calcium-apoptosis link.,” *Nat. Rev. Mol. Cell Biol.*, vol. 4, no. 7, pp. 552–65, Jul. 2003.

[92] S. J. Kalita, S. Bose, a. Bandyopadhyay, and H. L. Hosick, “Porous calcium aluminate ceramics for bone-graft applications,” *J. Mater. Res.*, vol. 17, no. 12, pp. 3042–3049, Jan. 2011.

[93] I. Sopyan, A. Fadli, and M. Mel, “Porous alumina-hydroxyapatite composites through protein foaming-consolidation method.,” *J. Mech. Behav. Biomed. Mater.*, vol. 8, pp. 86–98, Apr. 2012.

[94] S. B. Goodman, T. Ma, R. Chiu, R. Ramachandran, and R. Lane Smith, “Effects of orthopaedic wear particles on osteoprogenitor cells,” *Biomaterials*, vol. 27, no. 36, pp. 6096–6101, 2006.

[95] C. a Schneider, W. S. Rasband, and K. W. Eliceiri, “NIH Image to ImageJ: 25 years of image analysis,” *Nat. Methods*, vol. 9, no. 7, pp. 671–675, Jun. 2012.

[96] A. Priya, S. Nath, K. Biswas, and B. Basu, “In vitro dissolution of calcium phosphate-mullite composite in simulated body fluid.,” *J. Mater. Sci. Mater. Med.*, vol. 21, no. 6, pp. 1817–28, Jun. 2010.

[97] C. P. Klein, J. M. de Blieck-Hogervorst, J. G. Wolke, and K. de Groot, “Studies of the solubility of different calcium phosphate ceramic particles in vitro.,” *Biomaterials*, vol. 11, no. 7, pp. 509–512, 1990.

[98] P. Ducheyne, S. R. Radin, and L. King, “The effect of calcium phosphate ceramic composition and structure on in vitro behavior. I. Dissolution,” *J. Biomed. Mater. Res.*, vol. 27, no. 1, pp. 25–34, 1993.

[99] L. Morejón-Alonso, “Development and characterization of α-tricalcium phosphate/monocalcium aluminate composite bone cement,” *J. Biomed. Sci. Eng.*, vol. 05, no. 08, pp. 448–456, 2012.

[100] M. L. Wang, R. Tuli, P. a Manner, P. F. Sharkey, D. J. Hall, and R. S. Tuan, “Direct and indirect induction of apoptosis in human mesenchymal stem cells in response to titanium particles.,” *J. Orthop. Res.*, vol. 21, no. 4, pp. 697–707, 2003.

[101] C. C. Okafor, H. Haleem-Smith, P. Laqueriere, P. A. Manner, and R. S. Tuan, “Particulate endocytosis mediates biological responses of human mesenchymal stem cells to titanium wear debris,” *J. Orthop. Res.*, vol. 24, no. 3, pp. 461–473, 2006.

[102] M. Hashimoto, J. Sasaki, and S. Imazato, “Investigation of the cytotoxicity of aluminum oxide nanoparticles and nanowires and their localization in L929 fibroblasts and RAW264 macrophages,” *Journal of Biomedical Materials Research Part B: Applied Biomaterials*. 2015.

[103] S. C. Schmitt, M. Wiedmann-Al-Ahmad, J. Kuschnierz, A. Al-Ahmad, U. Huebner, R. Schmelzeisen, and R. Gutwald, “Comparative in vitro study of the proliferation and growth of ovine osteoblast-like cells on various alloplastic biomaterials manufactured for augmentation and reconstruction of tissue or bone defects,” *Journal of Materials Science: Materials in Medicine*, vol. 19, no. 3. pp. 1441–1450, 2008.

[104] A. Bernhardt, A. Lode, F. Peters, and M. Gelinsky, “Novel ceramic bone replacement material Osbone in a comparative in vitro study with osteoblasts,” *Clin. Oral Implants Res.*, vol. 22, no. 6, pp. 651–657, 2011.

[105] A. J. Saklatvala, W. Davis, F. Guesdon, M. Karin, C. J. Marshall, and J. Saklatvala, "Interleukin 1 (IL 1) and tumour necrosis factor (TNF) signal transduction," *Philos. Trans. Biol. Sci.*, vol. 351, no. 1336, pp. 151–157, 1996.

[106] Y. K. Liu, Q. Z. Lu, R. Pei, H. J. Ji, G. S. Zhou, X. L. Zhao, R. K. Tang, and M. Zhang, "The effect of extracellular calcium and inorganic phosphate on the growth and osteogenic differentiation of mesenchymal stem cells in vitro: implication for bone tissue engineering.," *Biomed. Mater.*, vol. 4, no. 2, pp. 1–8, Apr. 2009.

[107] H. Haleem-Smith, E. Argintar, C. Bush, D. Hampton, F. William, F. H. Chen, T. Rimington, J. Lamb, and R. S. Tuan, "Biological Responses of Human Mesenchymal Stem Cells to Titanium Wear Debris Particles," *J. Orthop. Res.*, vol. 30, no. 6, pp. 853–863, 2012.

[108] L. Huyck, C. Ampe, and M. Van Troys, "The XTT Cell Proliferation Assay Applied to Cell Layers Embedded in Three-Dimensional Matrix," *Assay Drug Dev. Technol.*, vol. 10, no. 4, pp. 382–392, 2012.

[109] D. Liu, T. Troczynski, and W. J. Tseng, "Water-based sol-gel synthesis of hydroxyapatite: process development," *Biomaterials*, no. 22, pp. 1721–1730, 2001.

[110] C. S. Chai, K. A. Gross, and B. Ben-nissan, "Critical ageing of hydroxyapatite sol - gel solutions," *Biomaterials*, vol. 19, no. 24, pp. 2291–2296, 1998.

[111] A. R. Kumar and S. Kalainathan, "Sol – gel synthesis of nanostructured hydroxyapatite powder in presence of polyethylene glycol," *Phys. B Phys. Condens. Matter*, vol. 405, no. 13, pp. 2799–2802, 2010.

[112] N. Y. Mostafa, "Characterization, thermal stability and sintering of hydroxyapatite powders prepared by different routes," *Mater. Chem. Phys.*, vol. 94, no. 2–3, pp. 333–341, 2005.

[113] A. J. Ruys, M. Wei, C. C. Sorrell, M. R. Dickson, A. Brandwood, and B. K. Milthorpe, "Sintering effects on the strength of hydroxyapatite," *Biomaterials*, vol. 16, pp. 409–415, 1995.

[114] G. Muralithran and S. Ramesh, "The effects of sintering temperature on the properties of hydroxyapatite," *Ceram. Int.*, vol. 26, pp. 221–230, 2000.

[115] J. Barralet, J. C. Knowles, S. Best, and W. Bonfield, "Thermal decomposition of synthesised carbonate hydroxyapatite," *J. Mater. Sci. Mater. Med.*, vol. 13, no. 6, pp. 529–533, 2002.

[116] F. Boschetti, M. T. Raimondi, F. Migliavacca, and G. Dubini, "Prediction of the micro-fluid dynamic environment imposed to three-dimensional engineered cell systems in bioreactors.," *J. Biomech.*, vol. 39, no. 3, pp. 418–25, Jan. 2006.

[117] A. L. Olivares, E. Marsal, J. a Planell, and D. Lacroix, "Finite element study of scaffold architecture design and culture conditions for tissue engineering.," *Biomaterials*, vol. 30, no. 30, pp. 6142–9, Oct. 2009.

[118] J. Sanz-Herrera, M. Doblaré, and J. García-Aznar, "Scaffold microarchitecture determines internal bone directional growth structure: A numerical study," *J. Biomech.*, vol. 43, no. 13, pp. 2480–2486, 2010.

[119] M. Cioffi, J. Küffer, S. Ströbel, G. Dubini, I. Martin, and D. Wendt, “Computational evaluation of oxygen and shear stress distributions in 3D perfusion culture systems: macro-scale and micro-structured models.,” *J. Biomech.*, vol. 41, no. 14, pp. 2918–25, Oct. 2008.

[120] C. Sandino, J. a Planell, and D. Lacroix, “A finite element study of mechanical stimuli in scaffolds for bone tissue engineering.,” *J. Biomech.*, vol. 41, no. 5, pp. 1005–14, Jan. 2008.

[121] F. Maes, T. Claessens, M. Moesen, H. Van Oosterwyck, P. Van Ransbeeck, and P. Verdonck, “Computational models for wall shear stress estimation in scaffolds: a comparative study of two complete geometries.,” *J. Biomech.*, vol. 45, no. 9, pp. 1586–92, Jun. 2012.

[122] P. J. Prendergast, R. Huiskes, and K. Søballe, “Biophysical stimuli on cells during tissue differentiation at implant interfaces,” *J. Biomech.*, vol. 30, no. 6, pp. 539–548, 1997.

[123] M. R. Dias, P. R. Fernandes, J. M. Guedes, and S. J. Hollister, “Permeability analysis of scaffolds for bone tissue engineering.,” *J. Biomech.*, vol. 45, no. 6, pp. 938–944, Apr. 2012.

[124] A. Lesman, Y. Blinder, and S. Levenberg, “Modeling of flow-induced shear stress applied on 3D cellular scaffolds: Implications for vascular tissue engineering.,” *Biotechnol. Bioeng.*, vol. 105, no. 3, pp. 645–54, Feb. 2010.

[125] P. V. Frédéric Maes, Peter Van Ransbeeck, Hans Van Oosterwyck, “Modeling Fluid Flow Through Irregular Scaffolds for Perfusion Bioreactors,” *Biotechnol. Bioeng.*, vol. 103, no. 3, pp. 621–630, 2009.

[126] M. Spiller, “Doctor Spiller,” 2000. [Online]. Available: http://doctorspiller.com/Bone_Grafting/bone_grafting.htm.

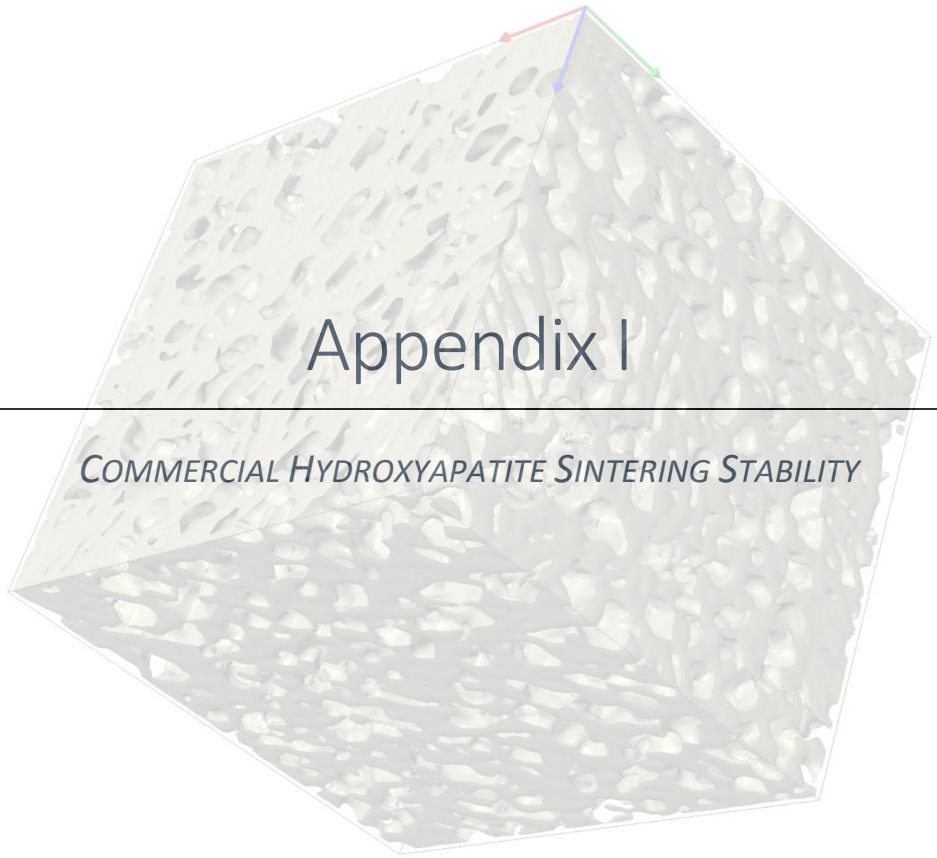

Appendix I

Commercial Hydroxyapatite Sintering Stability

I.1 Introduction

Hydroxyapatite can be produced in the lab through a relatively simple sol-gel method. The literature abounds with variations on this method producing differing phase purities of hydroxyapatite [109]–[111]. A sol-gel method was trialled during the course of this project however the decision was ultimately made to source commercially manufactured hydroxyapatite. This was done primarily to improve repeatability but also for financial and temporal practicalities.

It will be noted from the XRD data presented in Chapter 3 that the Sigma-Aldrich HA used throughout the project was found to be phase stable up to the maximum sintering temperature of 1350°C. The literature is ambiguous on how stable HA is at high temperatures; a common maximum quoted sintering temperature is 1200-1250°C [112], however it has also been demonstrated to be as high or higher than 1350°C [113], [114]. Furthermore it can be highly dependent on atmospheric composition during the sintering process [115].

Despite the reasonably unequivocal XRD data presented in Chapter 3 showing phase stability in the Sigma HA at 1350°C, it was felt prudent to compare that data to some other manufacturers' HAs. The comparison would encompass both phase stability and cell response and hence shed some light on the relative performance of commercial HA.

I.2 Materials and Methods

The three HA variants compared were the Sigma-Aldrich brand used throughout this project (abbreviated SA), CAPTAl-R sintering grade hydroxyapatite by Plasma-Biotal Ltd. (Buxton, UK) (abbreviated PB), and a purum p.a. grade hydroxyapatite from Fluka (sourced from Sigma-Aldrich) (abbreviated F). The methods of analysis are similar to those employed in Chapters 3 and 4 but are repeated here briefly.

I.2.1 2D Disks

Cells were cultured on 2D substrates to simplify the process. They were made by lightly pressing 200mg of the precursor powder for two minutes in a ø13mm die (International Crystal Laboratories, Garfield, NJ, USA) followed by sintering in a chamber furnace (Lenton, Hope, UK) under the following regime.

1. Ramp at 3°C/min up to 250°C.
2. Hold for one hour to facilitate burnout of organic components.
3. Ramp at 3°C/min up to maximum sintering temperature (1350°C).
4. Hold for three hours.
5. Ramp at 3°C/min to room temperature.

I.2.2 Cell Culture

Prior to culture all samples were sterilized by heating to 121°C for one hour in a vacuum oven (Binder, Tuttingen, Germany). Samples were seeded with porcine bone-marrow-derived MSCs at a density of 40,000 per well. Samples were incubated at 37°C for four hours before adding 500µl of media consisting of Dulbecco's Modified Eagle Medium (DMEM) Glutamax (Gibco, Dublin, Ireland), 10vol% foetal bovine serum, 2vol% penicillin/streptomycin and 0.1µl/ml amp-B

(all Sigma-Aldrich) to each. Cells were cultured for 11 days at 37°C and assayed at regular intervals. Cells cultured directly on tissue-culture plastic were used as a positive control.

I.2.3 Resazurin Media Assay

Cell proliferation and activity was assessed using the same resazurin assay described in Chapter 3.

I.2.4 X-Ray Diffraction (XRD) Analysis

XRD, as per Chapter 3, was carried out on powder samples of the HA variants that had been sintered to the same specifications as the disks.

I.2.5 Statistical Analysis

All experiments were duplicated. Groups were evaluated using one-way analysis of variance (ANOVA) and Tukey's comparison test. All analysis was performed in Minitab (Minitab Ltd., Coventry, UK).

I.3 Results

I.3.1 Cell Culture

Overall there is no significant difference in the cell response to the different substrates, Figure I.1. They generally all underperform the control and by day seven, this difference is significant, Figure I.2. However by day 11 the control has dropped down again and the four groups are statistically indistinguishable, Figure I.3.

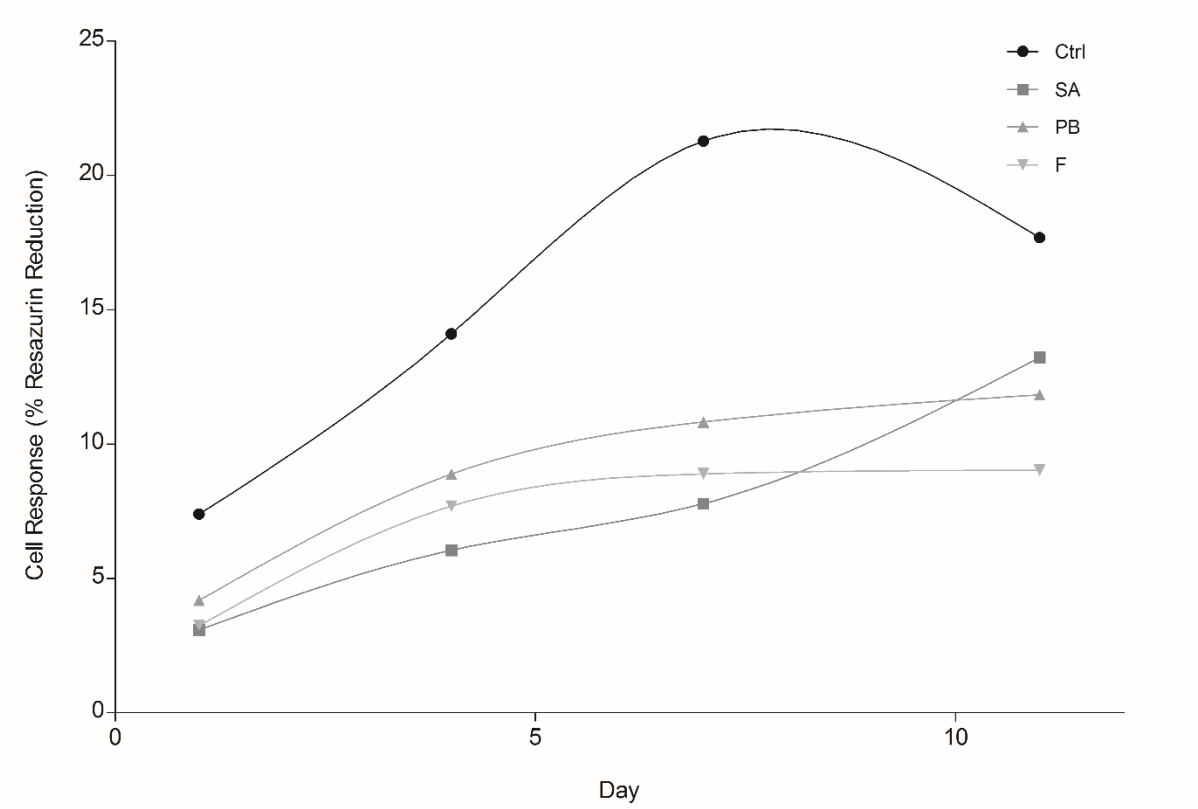

Figure I.1. *MSC response to tissue culture plastic control and Sigma-Aldrich, Plasma-Biotal and Fluka HA substrates across 11 days of culture.*

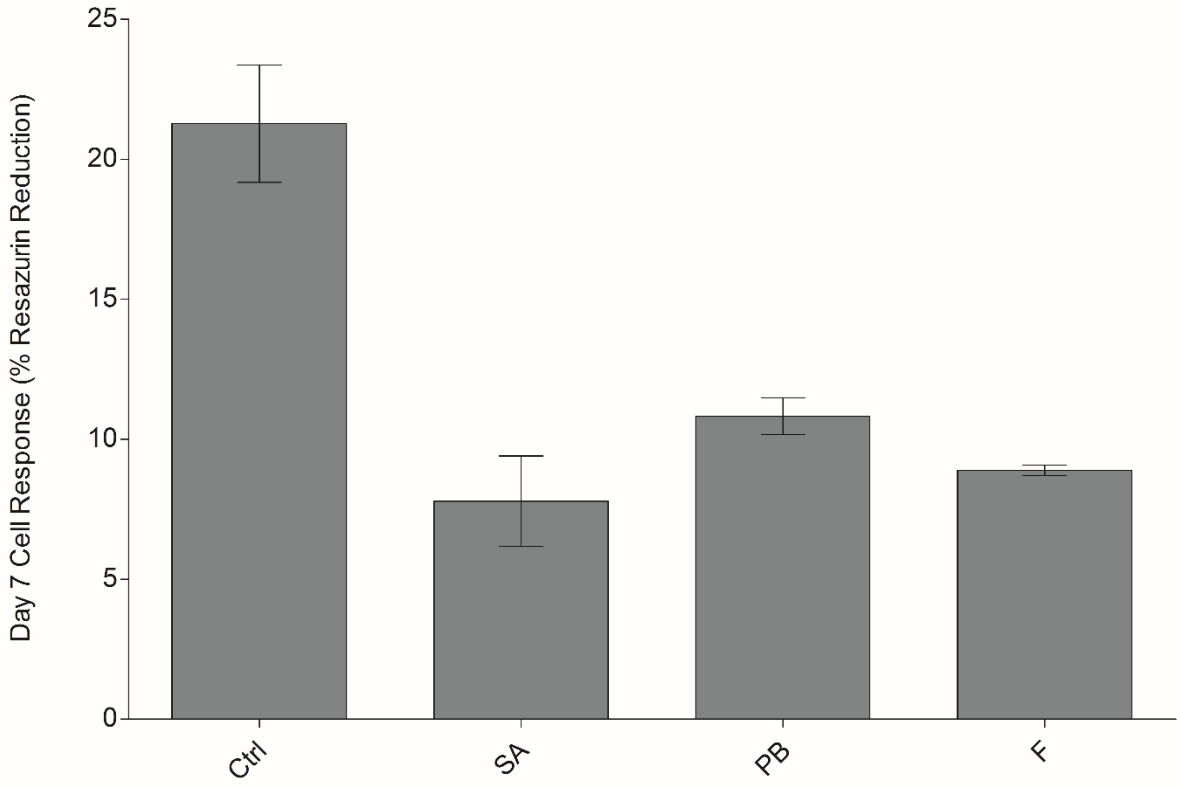

Figure I.2. *Day seven cell response to the three manufacturers' HAs and the tissue culture plastic control.*

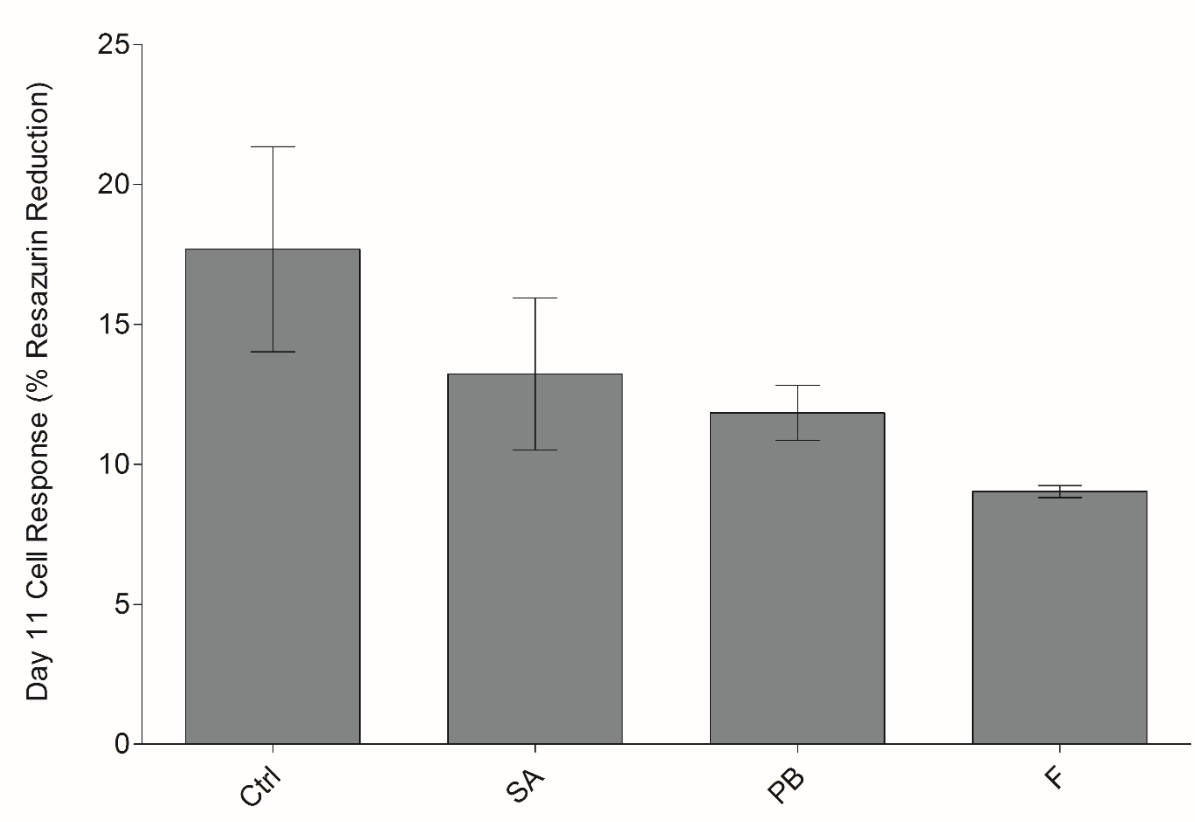

Figure I.3. *Day 11 cell response to the three manufacturers' HAs and the tissue culture plastic control.*

I.3.2 XRD Analysis

In contrast to the cell responses to the surfaces, there is marked variation in the respective XRD patterns of their sintered powders, Figure I.4. PB and SA are indistinguishable and show all the classic peaks of pure hydroxyapatite. There is some indication in each of trace amounts of β-tricalcium phosphate but those peaks are very faint. The Fluka sample meanwhile has completely decomposed to α-TCP.

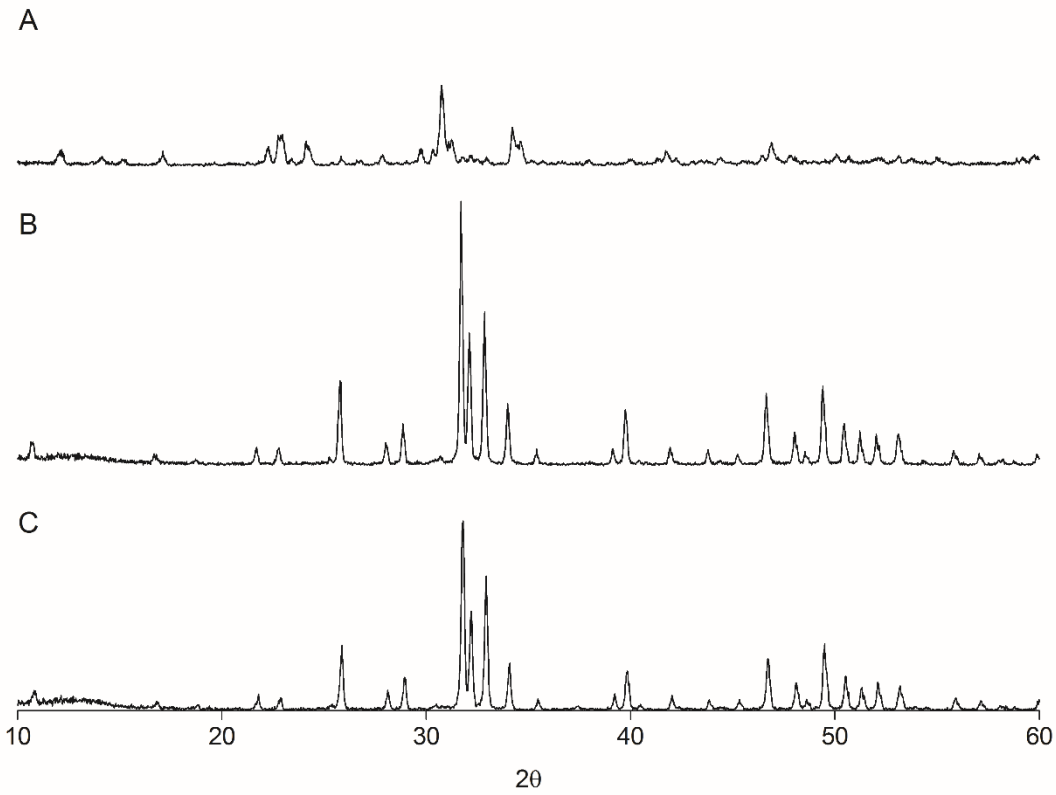

Figure I.4. *XRD data for (A) Fluka, (B) Plasma-Biotal and (C) Sigma-Aldrich HAs after sintering at 1350°C.*

I.4 Discussion

The purpose of this study was essentially to see whether the brand of hydroxyapatite used in the project could affect the results. Because sintering was taking place at high temperatures (>1250°C), the phase stability of the HA was in doubt. The data presented here clearly prove that from a phase stability perspective, the brand of HA does matter. The XRD data shows that Fluka HA completely decomposes to α-TCP upon sintering at 1350°C whereas both Plasma-Biotal and Sigma-Aldrich remain stable in the hydroxyapatite phase.

Interestingly, the phase differences in the materials did not appear to affect the cell response. No significant differences in cell activity on the various substrates were apparent across the culture period. This implies that α-TCP is as biocompatible as HA, at least *in vitro*.

Because of the similarity in cells behaviour, it could be argued that the choice of HA manufacturer makes no difference. However, it is not clear how, say, the Fluka HA would act when combined with alumina. It has already been shown in Chapter Four that the addition of the alumina catalyses the decomposition of Sigma-Aldrich HA to α-TCP. The sintering of alumina with a material that had already decomposed to α-TCP might well produce unexpected chemical outcomes. More work would be required to assess this.

In addition, it was noted in passing that the Fluka and Plasma-Biotal samples were more difficult to handle both pre- and post-sintering. This implies a variation in mechanical properties; with Sigma-Aldrich being the strongest. No data is available to confirm this however. In future, mechanical testing would have to be included in the analysis of HA brands if a change was being considered.

In any event, it would appear that the Sigma-Aldrich HA is a good choice for the kind of work described in this project. It is cheap, phase stable to 1350°C and produces cell responses no different to those of the other manufacturers tested.

I.5 Conclusion

This study highlights the variability in sintering behaviour between various brands of HA. Fluka was found to decompose to α-TCP upon sintering to 1350°C whereas both Plasma-Biotal and Sigma-Aldrich remained stable. Despite the differences in phase, no significant variance could be observed in the cell response to the respective substrates. This implies that, everything else being equivalent, both HA and α-TCP are equally good surface materials for the proliferation of mesenchymal stem cells. However, if a stable HA is required, Sigma-Aldrich is the best choice.

Appendix II

RESAZURIN SODIUM SALT ASSAY

II.1 Introduction

As explained in Chapter 2, the resazurin assay has been used in the literature as a cheap alternative to AlamarBlue® to assess the proliferation of various cell types [84]–[86]. However, it was decided to confirm that increased resazurin reduction coincided with increased mesenchymal stem cell number in order to verify the application of the assay in this work.

II.2 Materials and Methods

MSCs were cultured as detailed in Chapter 3. Cells were seeded in triplicate at densities of 20,000, 40,000, 60,000, 80,000, 100,000 and 200,000 per well in a standard 24 well plate. Blank wells were used as a control.

The cells were allowed four hours to adhere and then analysed using the resazurin assay as described in Chapter 3.

II.3 Results and Discussion

A regression plot of cell number against resazurin reduction gives an R^2 value of 0.9954 (Figure II.1). Clearly, as expected, there is a strong correlation between cell number and resazurin reduction. It is therefore reasonable to use the assay to assess proliferation where any increase in cell number will be represented by an increase in the resorufin fluorescence.

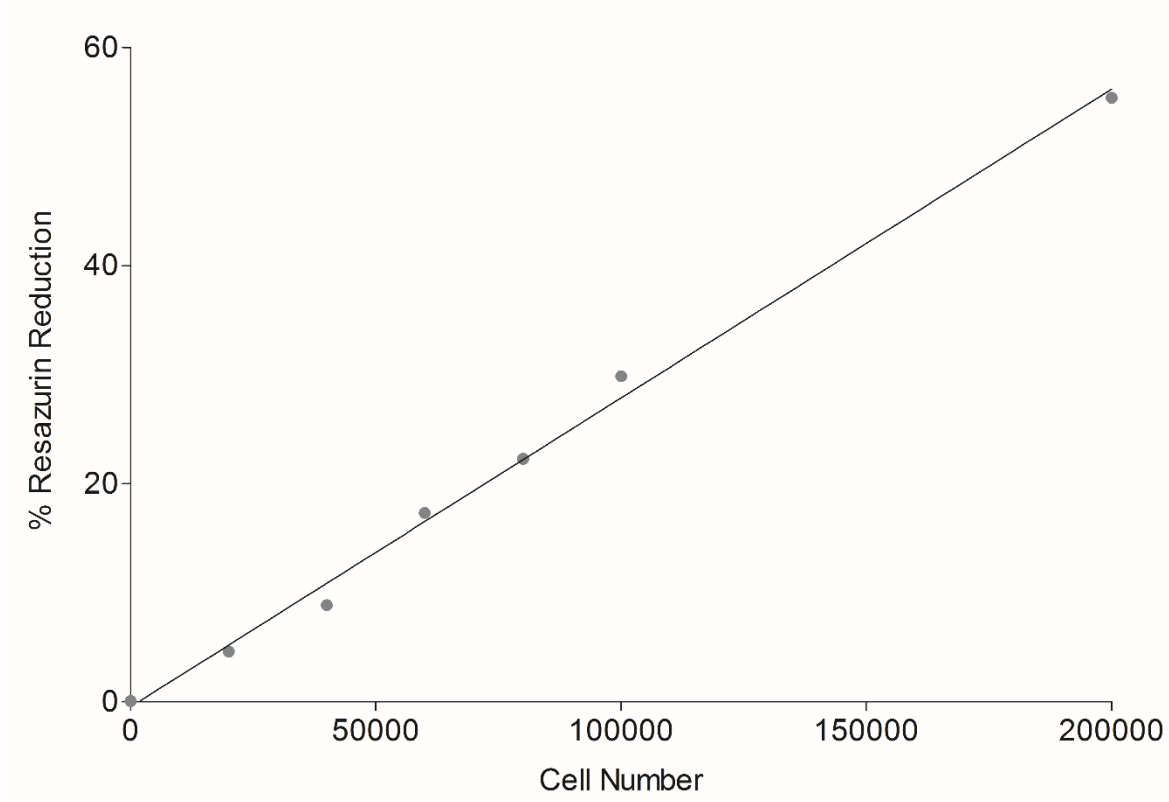

Figure II.1. *Linear regression of cell number against resazurin reduction. $R^2 = 0.9954$.*

II.4 Conclusion

The resazurin assay has been shown to accurately reflect increases in the numbers of viable MSCs. As such it is an appropriate metric to employ to differentiate scaffold surfaces based on cell activity.

Appendix III

COMPUTATIONAL MODEL

III.1 Introduction

A computational model is an excellent way of extending empirical studies. Once verified, it provides a cheap and efficient alternative to lab work. Initially, an *in silico* model of the diffusion scaffold environment was attempted as part of this project to assist in scaffold design. However, due to several factors including time and resource constraints, it was sidelined in favour of a purely *in vitro* mode of enquiry. Having said that, some important steps were made in the computational modelling process which may be of benefit in the future. As such, it is included here for reference.

III.1.1 Geometry Acquirement

The first step in any computational study is the selection of the geometry which will represent the problem *in silico*. Depending on the requirements of the simulation, the raw data for the geometry can come from one of two places.

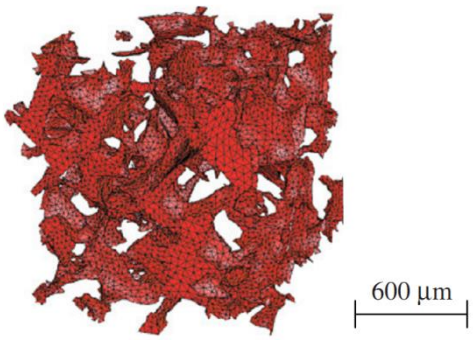

Figure III.1.*Model of microCT scanned scaffold from Cioffi et al.* [119].

The first is a bespoke design created using a modelling package such as **Gambit** or **Rhino 3D** [116], [117]. This method has the advantage of being adaptable and as simple as desired. It is generally used to represent an idealized version of the problem and, thus, is subject to a high degree of assumption. The alternative is to obtain the 3D geometry of an actual scaffold using a microCT scanner or similar [118], [119]. Here, 2D images of the structure are combined to form a 3D representation. The outcome of this second approach is a biomedically relevant structure whose accuracy is only limited by the resolution of the microCT scanner. However, it can present problems in the meshing phase as irregular geometries often

give rise to highly skewed elements in the mesh which can affect the accuracy of the resulting simulation. Such geometry will also be invariably complex and, as a result, will have an additional associated cost.

If the geometry is to come from raw data such as a microCT scan, it represents a serious rate-limiting step in the modelling process. This is due to the fact that it is not a trivial problem to convert that raw data into a mesh that can be readily understood by a program such as ANSYS Fluent. Although commercial software packages to do just this exist, they are invariably highly expensive.

III.1.2 Meshing Strategies

Once the geometry has been selected, the next stage is to use it to develop a robust and accurate mesh on which to perform analysis. The quality of the mesh refers to the shape and regularity of the individual elements and high quality is essential if one is to achieve an accurate result.

By far the most popular method for obtaining a workable mesh from any geometry, be it idealized or derived from microCT, is to use a commercial software package such as **Mimics** [117], [118], [120]. The advantage here is that very little work is required; a geometry is input and a mesh of specified format is output. However, as with any "black box" approach, a certain amount of control is relinquished to the program and the result must generally be taken at face value. The really prohibitive factor when using these types of program is their financial cost which can often put them out of reach of all but the best funded laboratories. As such, the development of a method to bypass that step in the process is highly desirable.

Some research groups have approached this problem by developing in-house software algorithms, for example Maes *et al.* [121] meshed their scaffold models using their own

Democells which they based on the **CGAL C++** library[7]. However, this approach still requires additional resources which may not be readily available.

III.1.3 Computational Modelling of Tissue Scaffolds

Once a mesh has been created it can be analysed in a variety of software packages e.g. **ANSYS Fluent**, **ABAQUS**, **OpenFOAM** etc. As with any experimental set-up there are as many ways of approaching a problem as there problems themselves. Some of the more relevant are detailed here.

Cioffi *et al.* [119] described macro/micro-scale models to analyse the oxygen concentration and shear stress distributions on chondrocytes seeded in a perfusion cultured porous scaffold. The macro-scale model represented the entire geometry of the bioreactor and was used to determine the initial and boundary conditions for a micro-scale region of interest constructed from µCT images of a poly(ethylene glycol terephthalate)/poly(butylene terephthalate) (PEGT/PBT) scaffold. Their results for oxygen concentration were corroborated by empirical observations at the inlet and outlet of the culture system using micro-oxygen sensors. The models were meshed using **Gambit** and solved in **ANSYS Fluent**. They found that, while the micro-scale model displayed small variations in oxygen concentration within the matrix, overall the two models agreed on that parameter at various depths. Additionally they established that a flow-rate of 0.3ml min^{-1} was sufficient to supply 99.5% of the scaffold with an oxygen concentration of between 2-8% (above anoxic levels of 1%) and subject 95% of the cells to a shear stress of less than 6.3mPa. They further postulated that a flow-rate of less than 0.03 ml min^{-1} would have likely result in severe depletion of cell viability in significant portions of the scaffold. Again, this highlights the issues surrounding implantation into the *in vivo* diffusion environment.

[7] Computational Geometry Algorithms Library. http://www.cgal.org

Olivares *et al.* [117] analysed the effect of mechanical loading and fluid shear stress on cell differentiation in two types of regular scaffold architecture. The architectures were selected for ease of CAD design and repeatability in rapid prototyping manufacture. They consisted of hexagonal and gyroid-based platforms with porosities of 55 and 70%. The designs were created using **Rhino3D** and **K3DSurf** and meshed with **Mimics Remesh**. Using **ABAQUS** software the simulated matrices were subjected to mechanical deformation and using **ANSYS Fluent** they were exposed to stresses caused by a perfused fluid. The group adapted a mechanoregulation theory from Prendergast *et al.* [122] which combines the above mechanical stimuli to yield an indicator for the cell phenotype that will be expressed. The analysis found that cell differentiation was much more sensitive to inlet fluid flow than deformation of the scaffold matrix. However, as no empirical observations were made to validate these results, their accuracy could be debated.

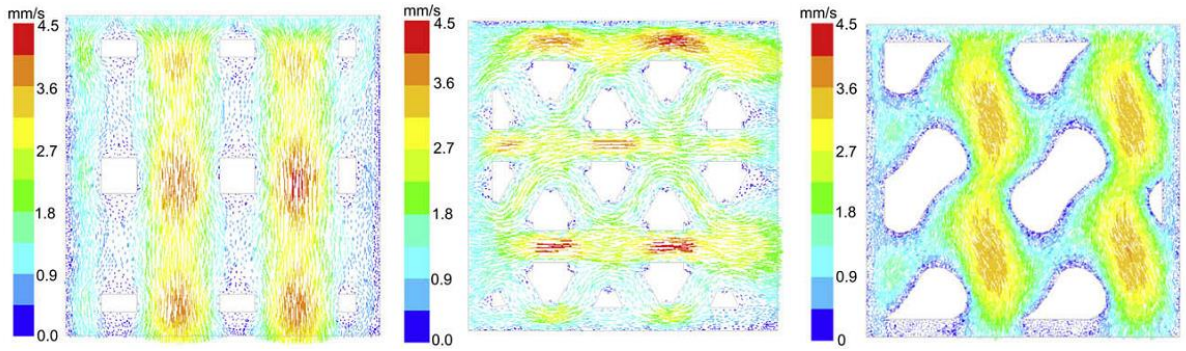

Figure III.2.*Fluid flow modelled through various geometries as investigated by Olivares et al.* [117].

The numerical cost issue has been looked at by Maes *et al.* [121]. Due to the limited computer resources of most labs, a smaller region or submodel is usually selected on which to perform analysis. It is then assumed that these results can be applied to the overall model as a whole. Maes *et al.* tested this hypothesis by comparing the results of wall shear stress through an entire scaffold model with those from a smaller subregion. They concluded that for heterogeneous geometries the region of interest should be selected to be between eight and ten times greater than the average pore size to yield effective results. This provides a useful guideline for any further simulations in this are when limited computing power is available.

III.1.4 Model Validation

The validation of computational models with physical experimentation is of the utmost importance. It is all too easy to be swept away by the ease of use and colourful imagery provided by software analysis.

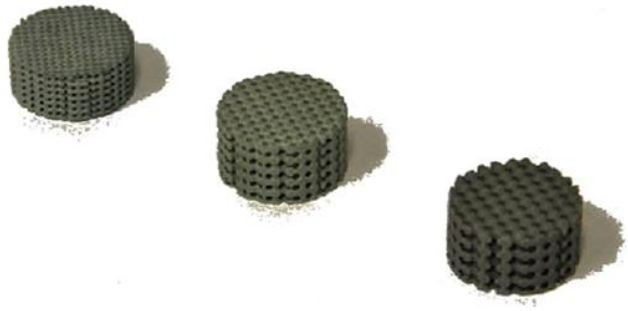

Figure III.3. *Scaffolds built in wax, using SFF techniques, 1mm, 1.4mm and 1.7mm unit cell size (from the left to the right), all with 50% porosity* [123].

Dias *et al.* [123] implemented a study to directly compare the permeability of scaffolds both computationally and empirically. The design consisted of repeating cell blocks to make up the porous structure. As mentioned, this approach greatly simplifies the numerical problem, which was solved in **MATLAB**. It also allows the scaffold to be manufactured using Solid Freeform Fabrication (SFF) as was the case here (Figure III.3). They printed the scaffolds in wax as they claim that the material itself was unimportant to the outcome of the experiment although this is debatable. Results showed good comparability between the computational and experimental values for permeability with both sets exhibiting the same trend (Figure III.4). However the experimental results are lower than their computational counterparts. The authors attribute this to the laminar flow assumptions they made particularly the fact that they made no allowance for

roughness or wettability.

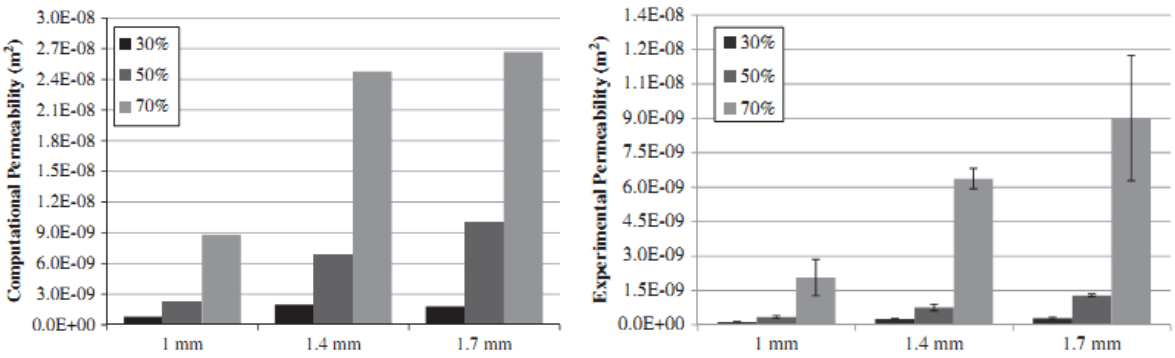

Figure III.4.*Computational (left) and experimental (right) permeability data. Grayscale represents porosity* [123].

The issue of validation becomes even more difficult when layers of complexity are added to the model without sufficient substantiation in the early stages. For example, Lesman *et al.* [124] attempted to model flow-induced shear stresses in 3D cellular scaffolds. The added complexity lay in their attempt to simulate cell growth on the pore surfaces by a stepwise decrease in the pore radius. They used permeability as an indication of the reliability of their model in each case as it is easily obtained both experimentally and *in silico*. Their predicted to experimental ratios varied from 31% to 2,602%. While there could be any number of reasons for these discrepancies, some of which such as initial assumptions and experimental difficulty are alluded to in the paper itself, it is clear that some refinement is required.

III.2 Materials and Methods

III.2.1 Introduction

The CFD model of fluid flow through the scaffold represents an attempt to develop a tool to verify and inform the design of future constructs. The ultimate objective is a model of oxygen diffusion through the scaffold pores. By necessity this will be the result of iterative models based on progressively more complex physics. The basic stages are as follows;

1. Conversion of a microCT image stack of the scaffold to an STL model which can be read by a meshing program.
2. Creation of a mesh from this geometry that can be recognised by ANSYS Fluent.
3. Model of basic fluid flow through the pores using Fluent.
4. Model of fluid flow with dissolved oxygen through the pores.
5. Model of oxygen diffusion through the pores.
6. Possible model of oxygen diffusion with added cell consumption.

This work comes with an important caveat which relates to steps one and two. Normally both of these can be taken care of by a commercial software package such as Mimics. However, such software is expensive so an effort has been made here to develop an alternative methodology using ImageJ [95] which is freely available as already stated. This approach has an obvious cost benefit however it is far less powerful. Coupled with limited computing resources this represents a bottleneck in the procedure which manifests itself as a maximum allowable size of the geometry that can be modelled in this work; approximately 1.2x1.2x1.2mm.

III.2.2 MicroCT Geometry Acquisition and Analysis

Scaffolds sintered at 1100-1350°C were scanned using a SCANCO µCT40 MicroCT Scanner (SCANCO, Medical AG, Brüttisellen, Switzerland). The scans were performed at the highest available resolution of 6µm.

III.2.3 Image Stack to STL File

The microCT images were imported into ImageJ as a stack of .tiff files. They were first cropped to an appropriate size (as discussed above) and cleaned (noise reduced) via the standard Despeckler and Gaussian filter. They were then converted to binary[8] via a visual thresholding technique. As each stack of images is different, this is the most expedient way of determining which parts of the image are the scaffold and which are just background. The technique simply involves sliding the threshold bar until an appropriate amount of the scaffold is highlighted. The software then converts these highlighted pixels to a value of 255 (white) and the rest are set to zero (black).

Inlet and outlet regions were required to facilitate the application of boundary conditions and to allow the flow to develop before entering the scaffold matrix. These regions, simple square-sectioned channels, were implemented via the addition of two more stacks; one above and one below the scaffold proper. These consisted of the same number of images as in the scaffold stack and their pixels were set to 255 so that ImageJ included them in the final mesh.

ImageJ was then commanded to produce an STL from the amalgamated stack of inlet, scaffold and outlet. The software essentially finds the boundary between the black and white pixels for each image in the stack and adds this boundary to the overall surface mesh. Once generated, the mesh was smoothed to remove any granulation that may have been left over from

[8] The STL file is essentially a surface mesh and, as such, requires a binary image as input.

the pixels of the image stack. Care must be taken here not to smooth so much that the overall pore shapes are lost.

III.2.4 STL File to Fluent Mesh

The STL mesh (at this stage referred to as the boundary mesh) was imported into ANSYS TGrid 3D 14.0.0 (ANSYS Inc., Canonsberg, PA, USA) and displayed to provide a quick visual check. Two plane surfaces were created at either end of the mesh and designated a velocity-inlet and pressure-outlet. These were then projected onto the mesh surface at both ends. A faceted stitch was performed on the apposed inlet-wall and outlet-wall surfaces followed by a remesh of the overall boundary using the text command Boundary/Remesh/Remesh-Overlapping-Zones. The boundary mesh was improved and refined using the default settings before the Auto-Mesh command was implemented to convert it to a volume mesh of tetrahedral elements. This mesh was then also improved in TGRID with default settings before export as a .msh file.

III.2.5 Model Implementation in Fluent

The finished mesh was imported into ANSYS Fluent (ANSYS Inc., Canonsberg, PA, USA), checked and scaled to the appropriate size. A laminar flow regime was deemed appropriate via a Reynold's Number calculation.

$$Re = \frac{\rho UL}{\mu}$$

Where ρ = density, U = velocity, L = characteristic length and μ = kinematic viscosity. A rough rule of thumb is that if the Reynold's Number is less than 2000, the flow can be said to be laminar. Due to the small length and velocity scales being dealt with here, Reynold's numbers would be typically very small and certainly far less than 2000.

Water was assigned as the interior fluid and the outlet pressure was set to zero pascals. The inlet velocity was initially set to 34µm s^{-1}, this value was taken from the literature to provide a rough estimation of whether or not the model was stable and realistic [125]. Later, this inlet condition was varied in an attempt to model the scaffold in a diffusion environment.

The model was initialised and set to solve for 200 iterations. Convergence was normally achieved before that point however. Results were analysed using the ANSYS CFX Post viewer which can be used to visualize streamlines, wall shear stresses, planes of interest, etc.

III.3 Results

III.3.1 Introduction

Although no in-depth analysis has yet been performed using the CFD model, several milestones have been achieved along the way to its implementation. These are detailed below.

III.3.2 Image Stack to STL File

Figure III.5 shows a sample image from a microCT produced stack after cropping, filtering, smoothing and thresholding. Specifically the filters used were ImageJ's built in Despeckling and Gaussian Smoothing plugins. The stack was then combined with an inlet and outlet region and exported as an STL surface mesh (Figure III.6).

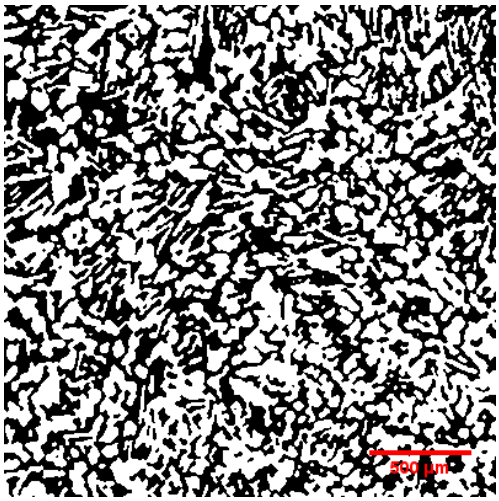

Figure III.5. *Prepared image from stack originating from scan of a scaffold sintered 1350°C, scale bar is 500µm.*

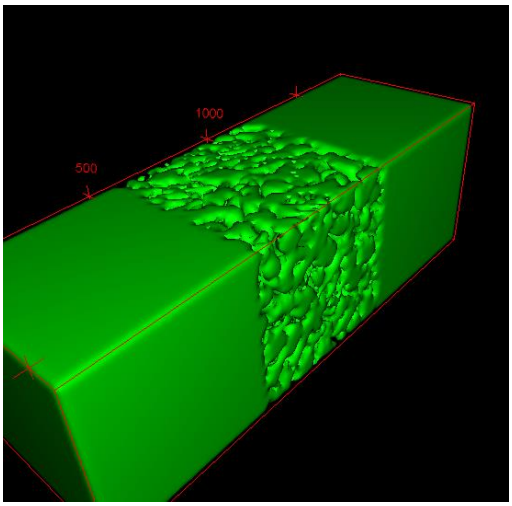

Figure III.6. *STL surface mesh of scaffold sample including inlet and outlet regions taken from ImageJ. Scale is in µm.*

III.3.3 STL File to Fluent Mesh

After the STL file had been imported into ANSYS TGrid, inlet and outlet boundary conditions were added and stitched. The volume mesh could then be generated and refined (Figure III.7). This mesh can then be read by Fluent as a .msh file.

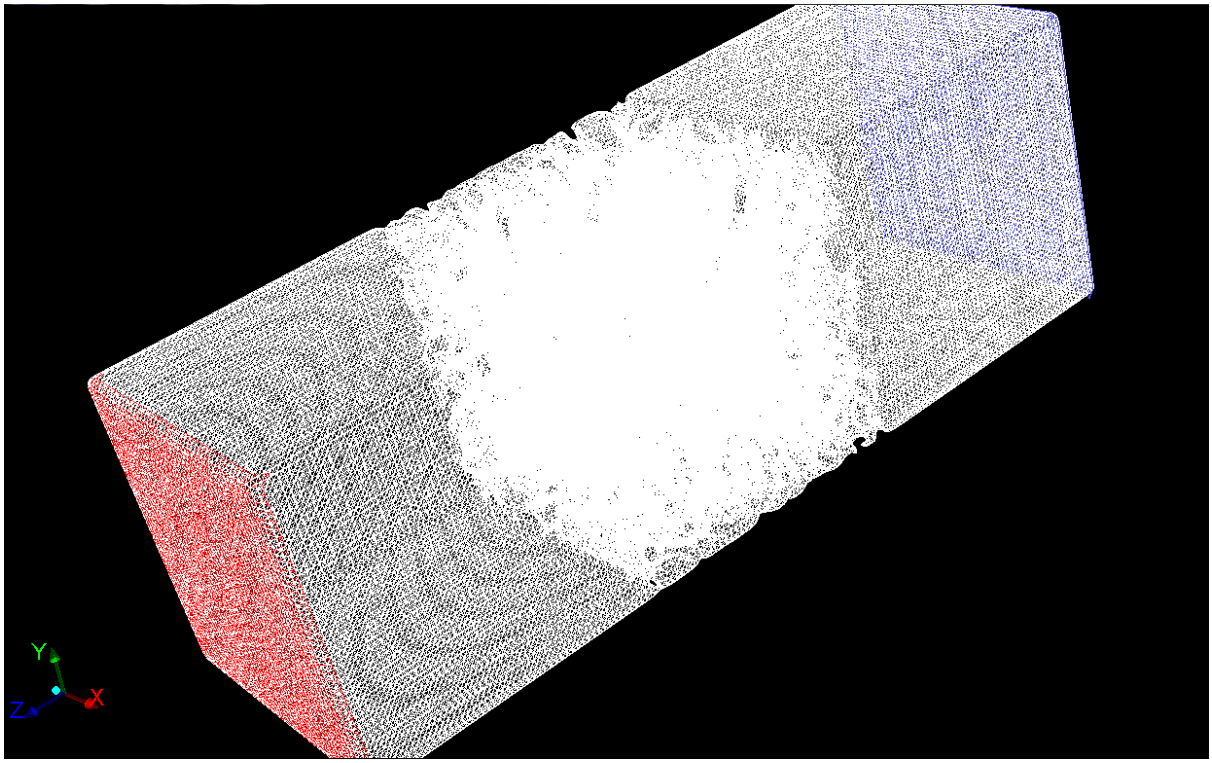

Figure III.7. *ANSYS TGrid display of the volume mesh showing inlet and outlet boundary conditions in red and blue respectively.*

III.3.4 Model Implementation in Fluent

Figure III.8 gives an indication of the possibilities presented by the model. It shows streamlines travelling through the pore network in response to a set velocity of 34µm/s at the inlet. The assumption of laminar flow was taken after computation of the Reynold's number of the flow as detailed in Section III.2.5. The value computed was ~0.046 which, being far less than 2000, indicated laminar flow.

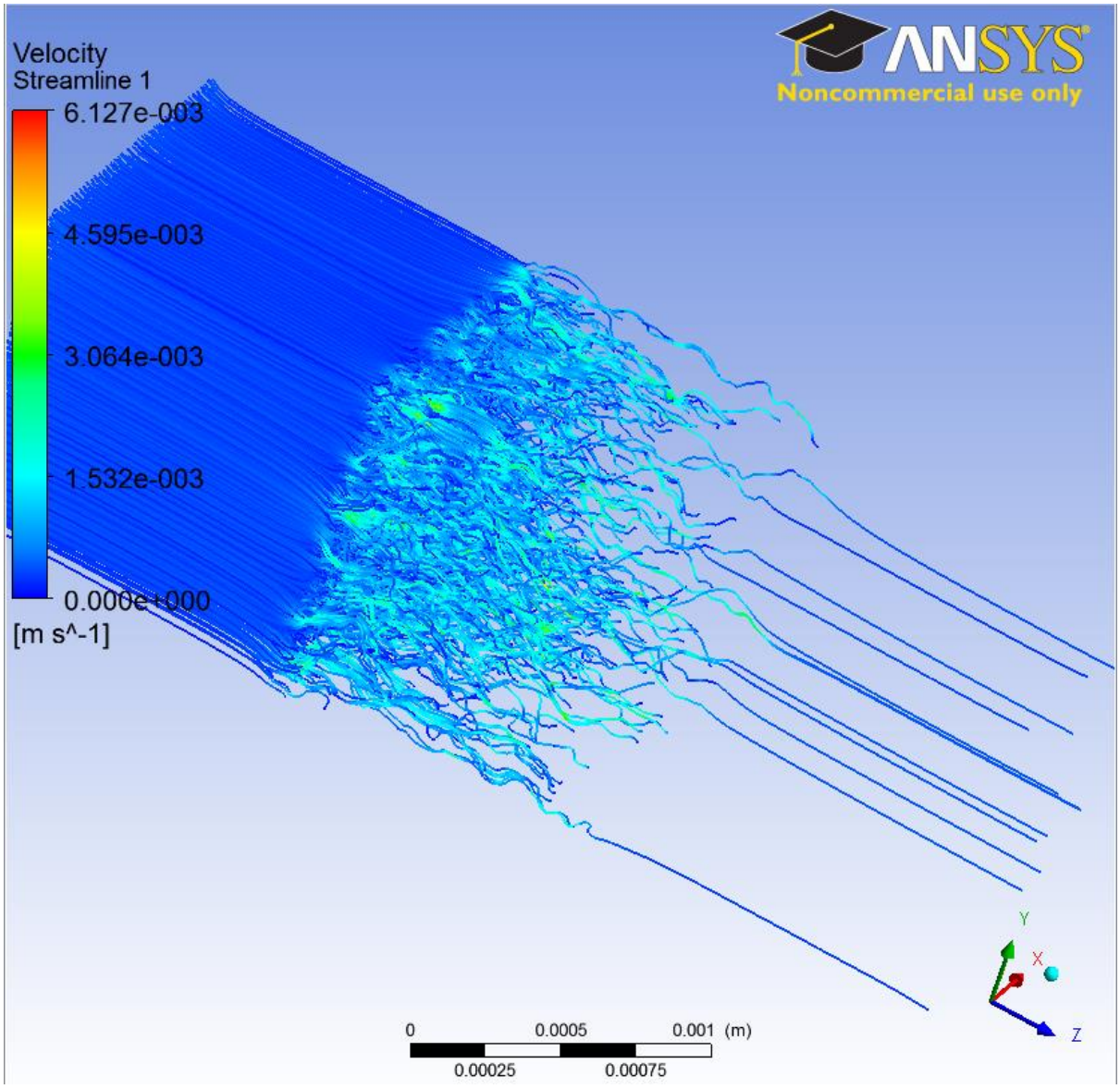

Figure III.8. *Streamlines showing fluid flow through the pore network in response to an inlet velocity of 34µm/s.*

III.3.5 Model Verification

A brief analysis was carried out using the model and a permeability value calculated based on the mass flow at the outlet and computed using Darcy's Law. The value of $2.56\times10^{-16}m^2$ that was obtained is four orders of magnitude smaller than that obtained by empirical observation; $1.41\times10^{-12}m$.

III.4 Discussion

Despite being some way from fully functional, several milestones have been achieved with the computational model's methodology. Chief amongst these is the use of ImageJ to produce an STL surface mesh from microCT scans of the scaffolds. This represents the removal of the most immediate rate-limiting step on the way to a usefully operating model. The fact that this was achieved without the use of an expensive software package such as Mimics will hopefully go some way towards curbing the cost of such models in future research. This is already high due to the need for modelling engines such as Fluent.

However, the process is not without its limitations. There is a certain lack of power associated with ImageJ and, coupled with the fact that all the analysis was being run on a standard desktop PC, this resulted in an apparent upper limit for the volume of sample that could be processed. So far this has appeared to be a cube measuring 1.2mm on a side. This is probably too small a size to draw many conclusions from, although there may be ways around it such as increasing N numbers or altering the shape of the sample. If this limit is deemed to be insurmountable and no alternative is found then the method may have to be abandoned.

A small amount of analysis was also done on the mesh in Fluent. Basic laminar flows were been set up and run through the pore network at an inlet speed of 34μm/s. This is relatively slow but is still some way from the diffusion regime that the scaffold will experience *in vivo*. Even so, this environment sufficed for basic analysis and model verification. The permeability value obtained using Darcy's equation and the mass flow rate at the outlet was $2.56\times10^{-16}m^2$. This was very much smaller than that obtained for the same scaffold type via empirical observation; $1.41\times10^{-12}m^2$. Even given the caveat that the analyses were rough proofs of concept and were not repeated this was still a large discrepancy.

There are numerous potential causes of inaccuracy in the model. As mentioned, the small volume tested may not contain enough information for a good result. If this is the case then a way

must be found to increase the mesh size. More mesh refinement may also be needed as the number of highly skewed elements caused by the geometry will have a profound effect on the model's capabilities.

III.5 Conclusion

The main achievements associated with the computational model were the protocol steps developed to get a stack of microCT images into a recognisable 3D format, accurately mesh them and subsequently import them into ANSYS Fluent for analysis. The advantage of the method presented here over a proprietary program such as Mimics is primarily cost. It eliminates the need for an additional, expensive software package. As such, it may prove useful for labs with limited budgets who nonetheless wish to pursue an *in silico* modelling project.